



# CVD diamond applications for particle detection and identification in high-radiation environments

Matevž Červ  
Vienna University of Technology

A thesis submitted for the degree of  
*Doctor of technical sciences*

Geneva 2016



# Contents

<b>1</b>	<b>Introduction</b>	<b>1</b>
1.1	Fundamental research . . . . .	2
1.2	Research institutes . . . . .	3
1.3	The Large Hadron Collider . . . . .	5
1.4	The ATLAS experiment . . . . .	6
1.5	Particle detectors . . . . .	7
<b>2</b>	<b>Diamond detectors for radiation detection</b>	<b>9</b>
2.1	Semiconductor detectors . . . . .	10
2.2	Principles of signal formation in semiconductors . . . . .	11
2.3	Carrier transport in a diamond sensor . . . . .	15
2.4	Radiation-induced current signals . . . . .	16
2.5	Radiation damage . . . . .	21
2.6	Temperature effects . . . . .	22
2.7	Electronics for signal processing . . . . .	23
<b>3</b>	<b>Diamond irradiation study</b>	<b>31</b>
3.1	Measurement setup . . . . .	31
3.2	Charged particle pulses and spectra . . . . .	36
3.3	Radiation limitations . . . . .	39
3.4	Temperature limitations . . . . .	48
3.5	Conclusion . . . . .	56
<b>4</b>	<b>Charge monitoring</b>	
	<i>The ATLAS Diamond Beam Monitor</i>	<b>57</b>
4.1	Introduction . . . . .	57
4.2	Luminosity measurements . . . . .	58
4.3	Diamond pixel module . . . . .	59
4.4	Module assembly . . . . .	62
4.5	Performance results . . . . .	63
4.6	Installation and commissioning . . . . .	68
4.7	First collision data . . . . .	70
4.8	Conclusion . . . . .	72
<b>5</b>	<b>Current monitoring</b>	
	<i>Real-time particle identification</i>	<b>73</b>
5.1	Motivation . . . . .	73

*CONTENTS*

---

5.2 Requirements . . . . .	74
5.3 Device specifications . . . . .	74
5.4 Pulse parameters . . . . .	75
5.5 Description of the firmware . . . . .	76
5.6 Control and data interface . . . . .	82
5.7 Performance results . . . . .	83
5.8 Source calibration . . . . .	85
5.9 Applications in neutron instrumentation . . . . .	102
5.10 Conclusion . . . . .	116
<b>Bibliography</b>	<b>117</b>

# Chapter 1

## Introduction

Curiosity is the driving force behind the development of human civilisation. Over centuries, scientists have discovered new methods for understanding Nature and the fundamental mechanisms governing the Universe, using continually improving research methods and technology to peer ever deeper into the heart of matter.

After the initial discovery of atoms, their underlying structure was soon revealed to be that of a positively charged core surrounded by a cloud of orbiting electrons. The atomic nucleus was subsequently decomposed into protons and neutrons, which themselves were found to consist of three tiny quarks. Studying these minuscule building blocks of visible matter has made it possible to understand more about the intricate complexities of the Universe, and the mechanisms that guide its behaviour and evolution.

Discoveries of this magnitude would not have been possible without the technologies developed to carry out such experiments. On one hand, the energy of the experimental devices has been increasing continually, allowing smaller and smaller distance scales to be probed. On the other hand, the devices used to observe and measure the phenomena created in these experiments have had to be designed with improved precision, speed and durability.

Keeping these factors in mind, the goal of this work was to find “the perfect material”. Diamond proved to be a worthy contender, offering both outstanding electrical and mechanical properties which make it the material of choice for a number of applications in experimental physics. However, much remains to be learned about its behaviour, and this thesis adds a small piece to the shimmering mosaic of diamond research efforts.

The first chapter introduces some of the leading particle physics research institutes, and describes how their research is carried out. The second chapter discusses the properties of diamond detectors used in high energy particle physics experiments. A diamond sensor irradiation study is presented in chapter 3. The conclusions of this study define the constraints for the two diamond detector applications presented in the final two chapters.

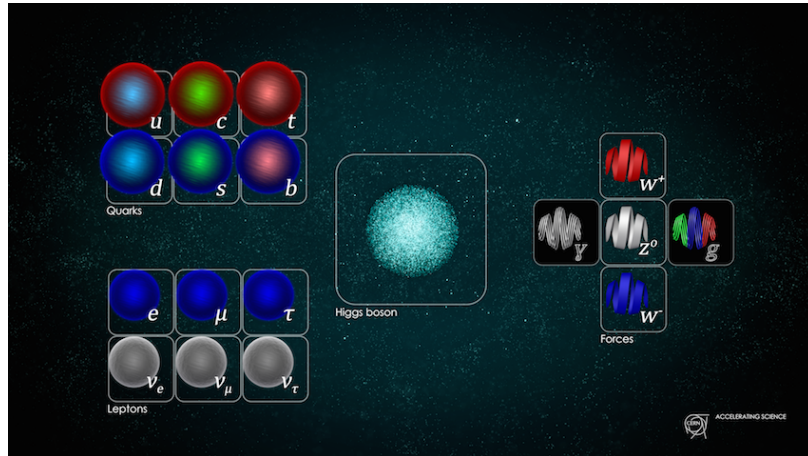


Figure 1.1: The Standard model [2].

## 1.1 Fundamental research

The aim of fundamental research is to define scientific theories and verify them to improve our understanding of the universe. It does not in itself focus on applying this research by developing products and is not meant to create a direct return on investment. Instead, it expands the overall knowledge of the human kind - by making the results freely available to the general public.

Particle physics research peers into the smallest constituents of the universe, dissecting the atoms into quarks and electrons, detecting cosmic rays and figuring out what dark matter is made of. Particle physicists want to explain the phenomena surrounding us by studying the fundamental particles and the mechanisms governing their interactions. Understanding them would enable us to answer difficult questions: How did the universe begin? What is the invisible force (dark matter, dark energy) pushing the galaxies apart from each other? Where does mass come from? Why is there almost no antimatter in the universe? In this effort, scientists have formed several theories. One of them, the Standard Model of particles, is currently the most successful theory to describe the constituents of matter and their interactions.

**The Standard Model** (SM) is a physics theory developed in the 1970's [1]. It was designed to explain the experimental results obtained at that time. As such, it was also able to predict new discoveries and was a driving force for the scientists to invest time and money in developing new experiments. To date, it is by far the most established and verified physics theory, despite its inability to explain gravity and dark matter. It explains how the basic building blocks of matter – *fermions* – interact with each other via mediators of interactions called *bosons*. There are two main families of fermions - *quarks* and *leptons*, as shown in figure 1.1. Each group consists of six members divided into three *generations*, the first being the lightest and most stable and the last the heaviest, which are the most unstable. The nature around us is made up of particles from the first generation. Those from the second or third generations can only be found in cosmic rays or be produced artificially using particle accelerators.

Quarks have a spin of 1/2 and a charge of either +2/3 (up, charm, top) or -1/3 (down, strange, bottom) while leptons have a spin of 1/2 and a charge of either 1 (electron, muon, tau) or 0 (electron neutrino, muon neutrino, tau neutrino). Leptons only exist individually – they do not cluster. Quarks, however, immediately form a cluster of either two, three or more. Clusters of three are the most stable – two up quarks and one down quark make up a proton whereas two down and

one up quark make up a neutron.

In addition to fermions, each particle has its corresponding antiparticle – a particle with the same mass but the opposite charge. If an antiparticle hits a particle, they annihilate each other, producing energy in form of photons and gluons.

Bosons are the carriers of force that mediate weak ( $W^+$ ,  $W^-$  and  $Z$  bosons), strong (gluons) and electromagnetic (photons) interactions. The weak interaction is responsible for the radioactive decay of subatomic particles, thus playing an essential role in nuclear fusion – a process taking place in the stars. The electromagnetic interaction works at a macroscopic level – it allows particles to interact via electric and magnetic fields. The strong interaction is effective at femtometer distances and it governs how quarks interact and bind with each other. An additional boson is the Higgs boson discovered at CERN in 2012 [3]. It is a representation of the Higgs mechanism, which gives rise to the mass (or lack thereof) of all the particles in the Standard Model.

## 1.2 Research institutes

This section gives a short overview of some of the institutes and collaborations carrying out fundamental physics research. These facilities were used for the research carried out in the scope of this work.

**CERN** (European Centre for Nuclear Research) [4] is the largest particle physics laboratory in the world, straddling the Swiss-French border just outside Geneva. It was established in 1954 to bring the war-torn Europe together by means of fundamental scientific research. Today, its 22 member state countries and several observer states contribute approximately 1 billion CHF annually to fund the research and development. More than 10000 scientists, engineers, technicians, students and others from all around the globe work at CERN on many projects in research fields ranging from particle to nuclear physics. The scope is to probe the fundamental structure of the universe and to understand the mechanisms governing it. Therefore CERN’s main function is to provide the infrastructure for high-energy physics experiments. These are carried out using large machines called particle accelerators. These instruments boost beams of particles to high energies before making them collide with each other or with stationary targets. The resulting collisions are recorded by particle detectors and later analysed by physicists. To conduct research on the smallest constituents of matter, their dynamics and structure, very high energies are needed. This is why the most powerful accelerators are used for fundamental research. The largest accelerators at CERN are the Proton Synchrotron [5], the Super Proton Synchrotron [6] and the Large Hadron Collider, described in 1.3.

**Atominstitut, Vienna** (ATI) [7], Austrian institute for atomic and subatomic physics, was established in 1958 in Vienna as an inter-university institute. It houses around 200 people involved in a broad range of research fields: quantum, particle, neutron, nuclear, radiation and reactor physics, quantum optics etc. As of 2002 the ATI is part of the University of Technology in Vienna. Its central facility is *TRIGA MARK II* [9], a neutron reactor used for training, research and isotope production. It is one of 40 such reactors worldwide, produced by the Californian company General Atomic in the early 60’s. It is capable of continuous operation at a maximum output power of 250 kW. The reactor core consists of 3 kg of 20 % enriched uranium ( $^{235}\text{U}$ ). The fuel moderator rods are mostly made up of zirconium with a low percentage of hydrogen and uranium. Both the core and the rods are immersed in a pool of water as shown in figure 1.2 for the purpose of cooling and radiation protection. The surrounding concrete walls are 2 m wide with an added graphite layer for

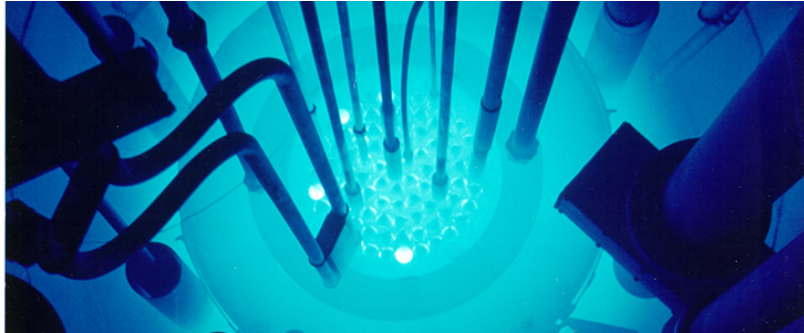


Figure 1.2: The TRIGA MARK II neutron reactor [8].

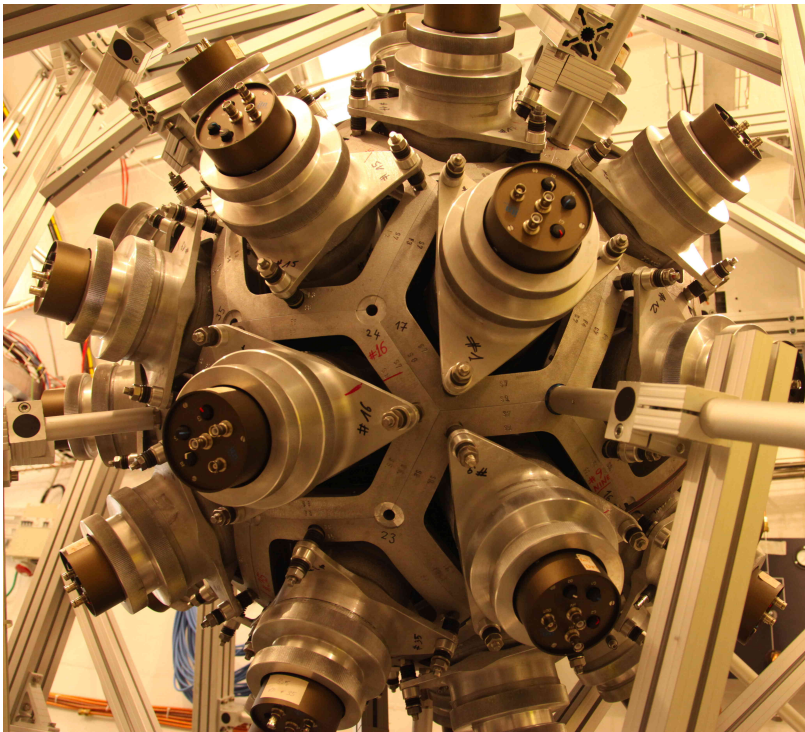


Figure 1.3: The calorimeter in the n-ToF area [11].

improved shielding. Four main experimental apertures for neutron beam are placed radially through the walls. All exits are heavily shielded to prevent people from being exposed to radiation, but still leaving enough space to set up experiments. Apart from the beam apertures, there are several other exits and components, e.g. a thermal column for generation of thermal (low energetic) neutrons.

**n-ToF** (neutron Time-of-Flight) [10] is a scientific collaboration with the aim of studying neutron-nucleus interactions. Over 30 institutes are active members of this collaboration, among them Atominstytut in Vienna. The n-ToF experiment is located at CERN where the experiments are carried out in a 200 m long experimental area. The knowledge stemming from the experimental results can then be applied in various fields ranging from nuclear technology and cancer therapy to astrophysics.

A pulsed beam of highly energetic protons (20 GeV/c) is produced by the Proton Synchrotron and aimed at a fixed lead spallation target. Each proton hitting the target produces around 300

neutrons of various energies. The initially highly energetic neutrons are slowed down by the target and by a slab of water behind it. This broadens their energy spectrum, which then ranges from meV (thermal neutrons) to GeV (fast neutrons). The neutrons are then sent through a 185 m long evacuated pipe to the experimental area, where they collide with another target or a sample. The radiation created by the collisions is detected by a set of dedicated detectors around the interaction point shown in figure 1.3. Having different energies, neutrons travel with different speeds, highly energetic ones reaching the target faster than those with low energies. The analysis of collisions with a precise timing allows for a determination of the interaction probability with the sample material as a function of energy of the incident neutrons.

### 1.3 The Large Hadron Collider

A particle accelerator is a machine that accelerates beams of charged particles such as protons, electrons, ions etc. It generates electric fields that add kinetic energy to the particles, speeding them up. It then uses magnets to retain them within a defined trajectory and inside the evacuated beam pipe. The trajectory can be either linear (linear accelerators or LINACs) or circular (circular or cyclic accelerators). The former accelerate particles in a straight line, therefore the acceleration process only occurs once. The latter can accelerate particles many times while keeping them in orbit, but need a LINAC to pre-accelerate the particles before being injected in the loop.

Particle accelerators are used in numerous fields ranging from fundamental and material research, cancer treatment to industrial applications, such as biomedicine and material processing. Several types of accelerators exist: electrostatic accelerators, LINACs, cyclotrons, synchrocyclotrons, synchrotrons and fixed-field alternating gradient accelerators (FFAGs).

The Large Hadron Collider (the LHC, figure 1.4) [12] at CERN is the largest particle collider in the world. It was build between 1998 and 2008 and was first successfully started in 2009 and operated until 2013 when it underwent a two-year long upgrade. Its second operational cycle started at the beginning of 2015.

The LHC is a 27 km long circular machine set up in a tunnel deep under the surface, ranging from 50 to 175 m below ground. It accelerates two proton beams to the energy of 6.5 TeV per beam before it makes them collide with each other with a centre-of-mass energy of 13 TeV at four different interaction points around its circumference. Hair-thin particle beams are guided inside two evacuated pipes with a  $\sim$ 5 cm diameter by means of a magnetic field. Coils made up of a superconductive material are wound around the pipes in special patterns. When cooled down to -271 °C using liquid helium, they become superconductive. Their resistivity of the material drops to the order of tens of  $n\Omega/m$  [14], minimising the heat dissipation despite high electric currents. These produce strong magnetic fields which bend the particles and keep them in a circular trajectory.

The protons travel in groups – bunches. There are  $10^{11}$  protons in every bunch and a maximum of 2808 bunches per direction in the accelerator. The bunches are accelerated when traversing the radio-frequency (RF) cavities with the frequency of the electromagnetic field equal to 400 MHz. This oscillating field creates 2.5 ns long buckets – compartments for the bunches. Only one out of ten buckets is filled, so the bunches are spaced at 25 ns. This defines the machine’s clock (40 MHz). The maximum rate of bunch crossings (the oppositely traveling bunches intersecting at a collision point) is 31.6 MHz and is defined as a product of the maximum number of bunches and the revolution frequency of 11.245 kHz, which is itself a quotient between the velocity of particles (close to the speed of light) and the circumference of the accelerator. 40 collisions on average occurred at every bunch crossing at the end of Run 1, yielding the maximum collision rate of the order of  $1.3 \times 10^9 s^{-1}$ . The

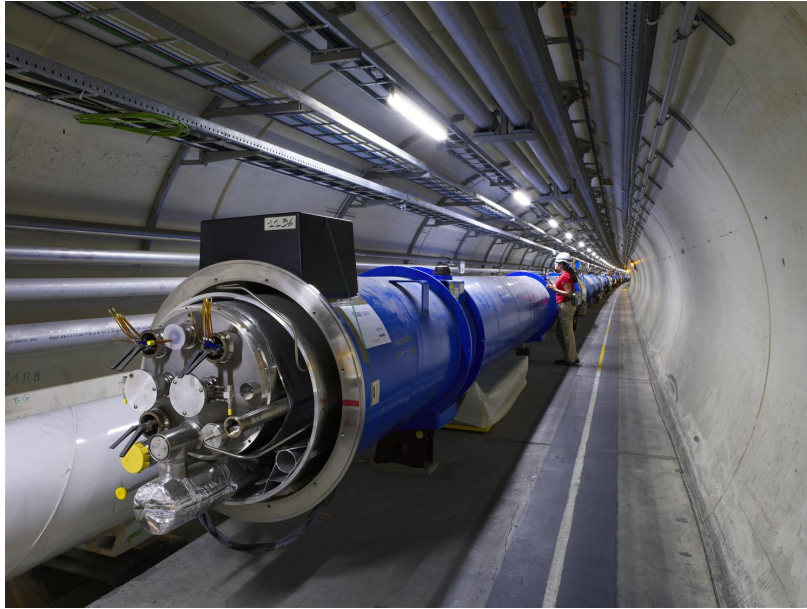


Figure 1.4: The Large Hadron Collider [13].

number of collisions will further increase in the following years. A higher collision probability will be achieved by increasing the number of particles per bunch and decreasing the transverse spread of the bunches, thus increasing the bunch density. The original design number of collisions accumulated over the years of operation is presented in the form of integrated luminosity [15] and is of the order of  $300 \text{ fb}^{-1}$  (inverse femtobarn) for Run 1 and Run 2 combined (2009–2024). After the planned upgrades in 2020, the High-Luminosity LHC [16] will achieve up to  $3000 \text{ fb}^{-1}$ .

## 1.4 The ATLAS experiment

ATLAS (short for A Toroidal Lhc ApparatuS, figure 1.5) [17] is a particle physics experiment at CERN. Its purpose is to verify current theories and to search for new discoveries by observing and analysing high energy proton-proton collisions produced by the LHC. It is the biggest experiment at CERN by dimensions (45 m in length and 26 m in height) and the number of people involved (more than 3000 physicists and engineers). The ATLAS experiment consists of a number of detectors, each designed to measure a specific property of the particles and photons produced during the collision. The closest to the collision point is the Inner Detector (ID). It consists of a Transition Radiation Tracker [19] and of several layers of highly spatially segmented semiconductor sensors, which record single points of the incident particles. These points are later reconstructed into particle tracks. In addition, a strong magnetic field of 2 T curves the paths of the charged particles, which in turn allows the ID to identify an individual particle's charge and momentum. The next two components of ATLAS are the electromagnetic calorimeter and the hadronic calorimeter. These detectors weigh several thousand tonnes and measure the energy that the particles deposit in the material. The only particles that make it through the calorimeters are neutrinos and muons. The former cannot be detected with the detectors in ATLAS. The latter however are detected by the Muon Spectrometer, a set of large detector plates placed all around the calorimeters. The last component is the superconductive magnet, which provides the magnetic field to allow the Muon Spectrometer to measure muon momenta. The ID has its own set of magnets that are used for the

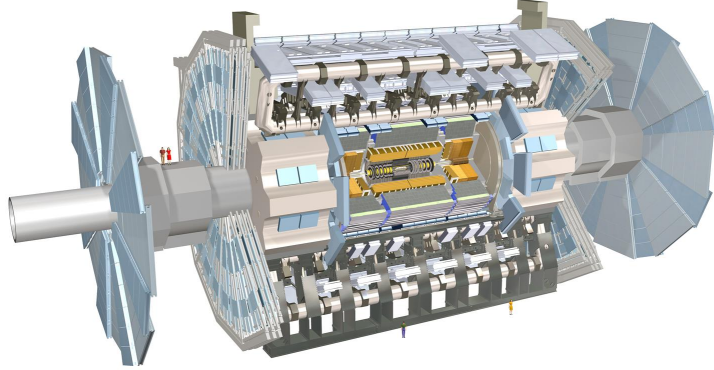


Figure 1.5: The ATLAS Experiment [18].

same purpose. To sum up, the Inner Detector measures charge and momenta of the particles, the calorimeters measure their energies, the Muon Spectrometer measures muon tracks and momenta and the magnets provide magnetic fields, which curve the trajectories of the charged particles, allowing for the identification of particle momenta.

The ATLAS detector cannot record the data for every collision due to a high data rate. Hence a selection process carried out by the Trigger System selects events with distinguishing characteristics that make them interesting for physics. The process divided in three stages.

The Level-1 trigger uses a subset of ATLAS data from the calorimeter and the muon chambers. The decision to keep a data from an event is taken in less than 2.5  $\mu\text{s}$  after the event has occurred. If so, the event data are read from the pipelined storage buffers of all detectors. This trigger reduces the event rate to  $\sim 100 \text{ kHz}$  [17].

The Level-2 trigger is a large array of custom processors that analyse in greater detail specific regions of interest identified by the Level-1 system for each event. In the mean time, the full event data are collected into buffers. The decision whether to keep an event or not is done within 10 ms. A few thousand events per second pass Level-2, and have their data passed on to Level-3.

The Level-3 trigger is a large farm of CPUs which perform a detailed analysis of the full event data and make a decision whether to store an event within 1 s. About 300-600 events per second are left after the Level-3 analysis, and these are passed on to a data storage system for offline analysis.

## 1.5 Particle detectors

Particle detectors, or radiation detectors, have first come into use at the end of the 19th century. In 1895 Wilhelm Röntgen used a photographic plate onto which he shone X-rays. Soon after, in 1912, Victor F. Hess discovered cosmic rays during a balloon flight. This paved the way for development of particle detectors. A cloud chamber was designed – a chamber filled with a supersaturated vapour of water or alcohol. If a highly energetic particle traversed the chamber, the mixture ionised, creating condensation nuclei. These traces were visible and were photographed. The particle detectors developed later relied on different types of interactions between the incident particles and the detector material, e.g. transition radiation, Cherenkov radiation and ionisation. By coupling a scintillating

## 1.5. PARTICLE DETECTORS

---

material with a photomultiplier tube (PMT), a scintillation detector was invented in 1944. An incident particle would hit the scintillating material, producing light. The PMT would multiply this signal and convert it into an electrical signal.

The bubble chamber invented in 1952 used a superheated transparent liquid – a liquid heated just below its boiling point. A particle ionised the liquid, forming microscopic bubbles along its trajectory. Then followed the spark chamber and the multi-wire proportional chamber (MWPC) where the particle ionised the gas, causing a spark between two parallel plates at a high potential difference. The MWPC was later upgraded to a time projection chamber to improve the particle trajectory reconstruction. Very important detectors were ionisation chambers, which measured the induced current of the free ionised charges moving in an externally applied electric field.

A special type of detectors was the Cherenkov detector. Cherenkov discovered in 1934 that a particle propagating through a dielectric at a velocity higher than the speed of light in said dielectric emits electromagnetic radiation. An example of this radiation is the blue glow in nuclear reactors, as shown in figure 1.2. An example of a modern Cherenkov detector is the ring-imaging Cherenkov detector (RICH), which allowed for identification of electrically charged particles.

Finally in the 1960s, semiconductor detectors were introduced. Their principle of operation is similar to that of an ionisation chamber, with the difference that a semi-conductive material is used as an ionisation medium instead of gas. Nowadays an ensemble of several types of detectors is used as a specialised detector system. Many considerations need to be taken into account when designing such a system: detector geometry, segmentation, event rate, efficiency, sensitivity, readout, support structures, cabling, cooling, cost etc.

Particle detectors can be divided in two groups: tracking detectors and calorimeters. The former are designed to measure particle momentum, charge, origin and direction of flight, with a minimal impact on their flight path or energy with the aim to optimise the spatial resolution. The calorimeters, on the other hand, measure the energy of the particles by stopping them. This means that they need to be heavy and dense. A typical physics experiment nowadays consists of a tracking detector enclosed by a calorimeter. This way the energy, charge and momentum can be derived for every particle created in the collision.

## Chapter 2

# Diamond detectors for radiation detection

Diamond has been known for over two millennia, valued for its mechanical properties and its appearance. When the procedures for its synthesis were discovered, diamond made its way to a broad range of industries which exploit its mechanical and electrical properties. The discovery of the Chemical Vapour Deposition (CVD, described below) as a new synthesis process gave rise to a range of new applications. Purer specimens are used in electronics, high-power switching devices, electrochemical systems, radiation detectors, quantum computing etc. Recently it was found that it also exhibits superconductivity [20]. This thesis focuses on the use of diamond for radiation detection. An example of such a diamond sensor is shown in figure 2.1.

Compared to a natural diamond, a CVD diamond used as a particle detector has almost no impurities (foreign atoms like nitrogen or boron). If proper procedures are followed, the diamond lattice can be grown very uniformly. This in turn improves electrical properties of the grown sample. Such a diamond is an almost perfect thermal and electrical insulator. However, under certain conditions it behaves like a semiconductor. For this reason this chapter first introduces semiconductor detectors and describes the principle of signal formation in semiconductors. Then it focuses on the diamond sensor.

**Microwave plasma-assisted chemical vapour deposition** (MPCVD or short CVD) [21, 22] is a process where a material is deposited from a gas onto a substrate, involving chemical reactions. It takes place in enclosed chambers – furnaces – with careful regulation of the temperature, pressure and gas mixture.

Synthetic diamond is grown at 700–900 °C at a pressure of 20–100 mBar, with a mixture of hydrogen and methane gas. High-power microwaves (1–60 kW) ionise the gas mixture into plasma, creating carbon radicals and atomic hydrogen. The carbon atoms are the building blocks and are deposited on the substrate (growth surface). At such a low pressure, both graphitic and diamond bonds are formed. The abrasive atomic hydrogen etches away the graphitic bonds, leaving only diamond bonds in place.

The speed of the growth can be anywhere between 0.1 and 10 µm per hour. The detector grade samples are grown at a rate of the order of 1 µm per hour, with target thicknesses between 100 µm and 500 µm. The area of the samples, however, depends entirely on the substrate used. Diamond can be deposited on various materials: diamond, silicon, tungsten, quartz glass etc.

The substrate material must be able to withstand the high temperatures during the CVD process.

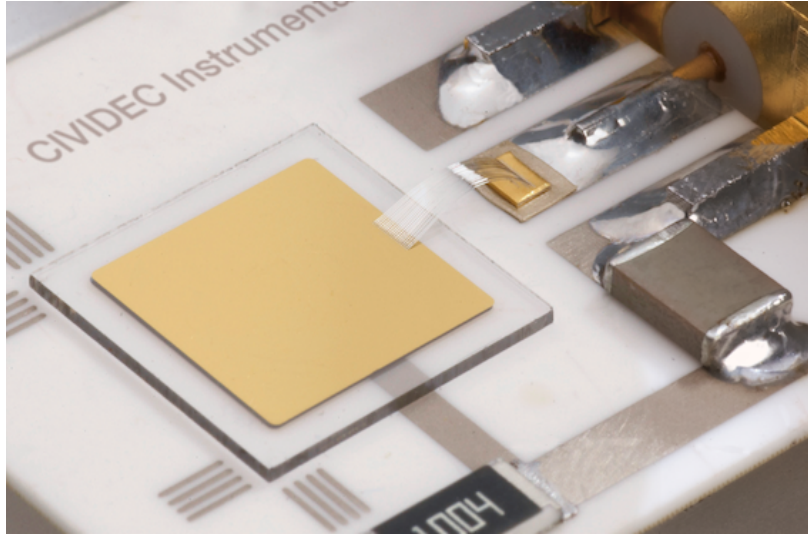


Figure 2.1: A pCVD diamond pad detector [23].

Carbon atoms form bonds with atoms in the existing crystal structure. This is the homo-epitaxial growth where the newly deposited atoms retain the orientation of the structure in the substrate. Mirror-polished high-pressure high-temperature (HPHT) synthetic single crystal diamonds have been most widely used as a substrate. Other non-diamond substrates need to be pre-treated by being polished using diamond powder. Powder particles remain on the surface, acting as seeds for the growth of small crystals or grains. These grains grow and at some point merge with the adjacent ones, gradually making up a compact material. The substrate side is later polished away. These diamonds are *polycrystalline* (pCVD) whereas those grown on a diamond substrate are *single crystal* (sCVD) diamonds. The area of the former can be large - up to  $75\text{ cm}^2$  in the case of detector grade diamonds, which can be further cut into smaller parts. The sCVD diamonds, on the other hand, can currently only achieve sizes up to  $8\text{ mm} \times 8\text{ mm}$ .

## 2.1 Semiconductor detectors

Semiconductor is a class of solids whose electrical conductivity is between that of a conductor and that of an insulator – of the order of  $10^{-5}\text{ }\Omega^{-1}\text{ cm}^{-1}$  [24]. Semiconductors consist of atoms with four electrons in their valence band, e.g. silicon–Si or germanium–Ge, or as combinations of two or more different materials, e.g. gallium arsenide–GaAs. The atoms in the lattice form valence bonds with adjacent atoms, creating solid crystal structures.

Semiconductor particle detectors are devices that use a semiconductor material to detect radiation. They operate on the principle of an ionisation chamber. An incident particle deposits some of its energy in the crystal lattice, ionising the atoms along its trajectory. The freed charge carriers start drifting in an externally applied electric field, inducing current on the electrodes. The induced signal is amplified and read out by the electronics in the detector signal chain.

Semiconductor detectors are most widely used as photodiodes. In high-energy physics experiments they found use in tracking applications, e.g. the Insertable B-Layer shown in figure 2.2 [25], which was installed in ATLAS in 2014. First, they can be produced in thin layers to minimise the impact on the path of the incident particles. Second, their low sensor capacitance allows for a fast signal response. Third, they are highly efficient and highly resistant to radiation damage.



Figure 2.2: The Insertable B-Layer – a silicon particle tracker installed in the ATLAS experiment in 2014 [26].

Finally, the industrial processes allow for a fine spatial segmentation, which in turn improves the track resolution of the detector systems.

Semiconductor sensors come in several configurations. The simplest type is a diode. Diodes are used for particle counting and radiation monitoring. Next is a strip detector, a more finely segmented detector made out of long parallel sensing areas or strips. Normally each strip has its own signal line for readout. Usually the strip detectors are used in pairs – one detector is placed on top of the other at an angle to increase the spatial resolution in both axes. The third and the most finely segmented is a pixel detector, consisting of a 2D array of independent sensing areas – pixels. In tracking applications, pixel detectors are used where the requirement for a high detection resolution and granularity requirement is the highest. Due to their high production cost and a high number of signal channels, they can only cover limited areas. Strip detectors, on the other hand, can be used to cover larger areas in several consecutive layers.

## 2.2 Principles of signal formation in semiconductors

Particles can interact with the sensor in several ways, e.g. via bremsstrahlung [27], elastic or inelastic scattering or nuclear reactions [28]. Bremsstrahlung is radiation created when a particle is decelerated due to interaction with the electric field of the core of an atom. Elastic scattering is deflection of the particle's trajectory due to the pull from the nucleus while preserving momentum. This is in principle an unwanted effect in semiconductors as it deteriorates the spatial resolution of the sensor. Inelastic scattering is the interaction through which an electron in the atom is *ionised*. A nuclear reaction is the direct interaction between the incident particle and the core of the atom. All these effects are competing and are dependent on the particle's mass, momentum, charge etc. The scope of this chapter is to discuss the ionisation mechanism in semiconductors.

The binding energy of the electrons forming valence bonds between atoms in the crystal lattice is within the *valence band* [24]. To break a bond and excite the electron into a *conduction band*, a sufficient energy has to be applied. The minimal energy required is equal to the energy band gap  $E_g$  of the semiconductor. Typical  $E_g$  values are 0.7 eV in Ge, 1.12 eV in Si and 1.4 eV in

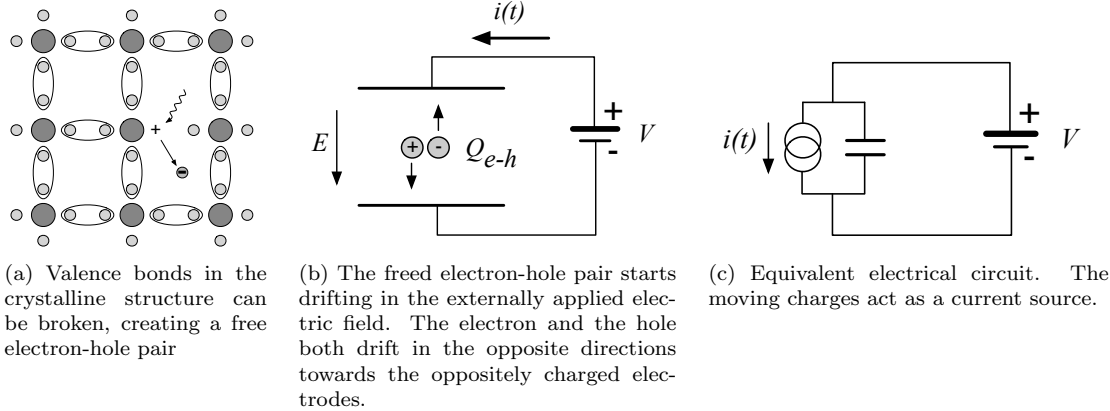


Figure 2.3: In the equivalent electrical circuit diagram the electron-hole creation and drift can be modelled as a current source with a capacitor in parallel.

GaAs. Diamond with its 5.5 eV band gap is considered an insulator. The separation between the conductive and the valence band is referred to as *band gap* where no electron states may exist.

An electron excited into the conduction band leaves behind a positively charged ion with a vacancy – a hole – in its valence band, as shown in figure 2.3a. A free *electron-hole pair* is thus created. The free electron travels through the crystal until it is recombined with another hole. Similarly the positive charge of the hole attracts a bound electron in the vicinity, causing it to break from the current bond and moving to the vacancy, thus leaving behind a newly created hole. The process continues, making it look like the hole is traveling through the crystal [24].

Both the electron and the hole are referred to as *charge carriers*. Without an externally applied electrical field, they propagate in random directions. Therefore on average there is no overall motion of charge carriers in any particular direction over time.

However, if an external electric field is applied to the crystalline structure, the free electrons and holes drift toward the positive and negative potential, respectively, as shown in figure 2.3b. While drifting, the charges couple with the electrodes, inducing current in the circuit, which is explained by the Shockley–Ramo theorem below. Upon reaching the electrodes the charges stop inducing the current. An equivalent electrical circuit is shown in figure 2.3c.

### 2.2.1 Signal induction by moving charges

Signal induction in a conducting plane by a point-like charge, which couples with an electrode, is derived in [29, 30]. The electrode can in this case be modelled as an infinite conducting plane. When a point charge  $q$  is created (e.g. an electron-hole pair created via ionisation), its electrostatic field lines immediately couple with the electrode, as seen in figure 2.4a. The electric field on the metal surface due to a point-like charge  $q$  at the distance  $z_0$  is

$$E_z(x, y) = \frac{q z_0}{2\pi\epsilon_0(x^2 + y^2 + z_0^2)^{\frac{3}{2}}}, \quad E_y = E_x = 0. \quad (2.1)$$

A mirror charge appears on the conducting plane, with a charge density distribution

$$\sigma(x, y) = \epsilon_0 E_z(x, y) = \frac{q z_0}{2\pi(x^2 + y^2 + z_0^2)^{\frac{3}{2}}}. \quad (2.2)$$

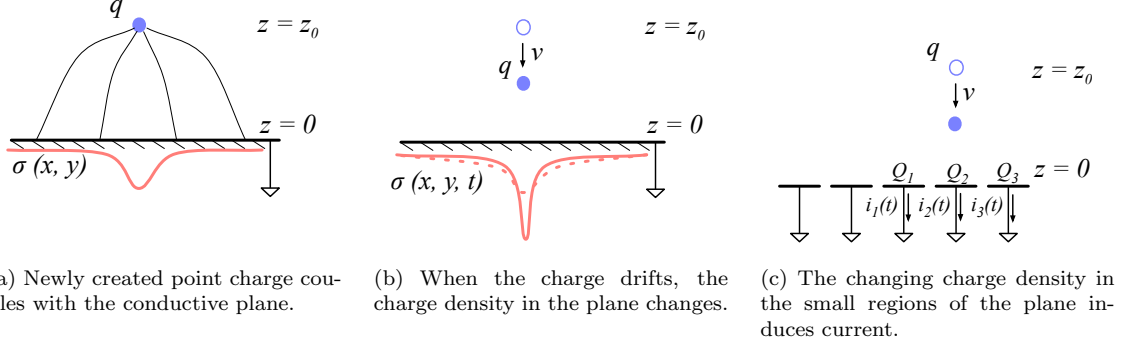


Figure 2.4: A point-like charge inducing current in a conductive plane.

The charge density integrated over the entire plane yields a mirror charge  $Q$ , which is an opposite of point charge  $q$ :

$$Q = \int_{-\infty}^{\infty} \int_{-\infty}^{\infty} \sigma(x, y) dx dy = -q. \quad (2.3)$$

The plane is then segmented into infinitely long strips with a width  $w$  whereby each of the strips is grounded, as shown in figure 2.4c. Considering a charge density distribution 2.2, the resulting mirror charge on a single strip  $Q_2$  directly below the point charge ( $x = 0, y = 0$ ) yields

$$Q_2(z_0) = \int_{-\infty}^{\infty} \int_{-w/2}^{w/2} \sigma(x, y) dx dy = -\frac{2q}{\pi} \arctan\left(\frac{w}{2z_0}\right) \quad (2.4)$$

If the charge starts moving towards the conducting plane, the mirror charge density distribution also changes, as shown in figure 2.4b. As a result the  $Q_2[z(t)]$  changes with time. The changing charge is in effect an induced electric current  $i_2(t)$ :

$$i_2(t) = -\frac{d}{dt} Q_2[z(t)] = -\frac{\partial Q_2[z(t)]}{\partial z} \frac{\partial z(t)}{\partial t} = \frac{4qw}{\pi[4z(t)^2 + w^2]} v. \quad (2.5)$$

The movement of the point-like charge therefore induces current in the conducting plane. The induced current is linearly dependent on the velocity of the point-like charge.

### 2.2.2 Shockley-Ramo theorem

W. Shockley [31] and S. Ramo [32] independently proposed a theory which explains how a moving point charge induces current in a conductor. The Shockley-Ramo theorem can therefore be used to calculate the instantaneous electric current induced by the charge carrier or a group of charge carriers. It can be used for any number of electrodes. It states that the current  $I_n^{\text{ind}}(t)$  induced on the grounded electrode  $n$  by a point charge  $q$  moving along a trajectory  $\mathbf{x}(t)$  reads

$$I_n^{\text{ind}}(t) = -\frac{dQ_n(t)}{dt} = -\frac{q}{V_w} \nabla \Psi_n[\mathbf{x}(t)] v(t) = -\frac{q}{V_w} \mathbf{E}_n[\mathbf{x}(t)] v(t), \quad (2.6)$$

where  $\mathbf{E}_n(\mathbf{x})$  is the *weighting field* of electrode  $n$  in the case where charge  $q$  is removed, electrode  $n$  is set to voltage  $V_w = 1$  and all other electrodes are grounded. The weighting field is defined as the spatial differential of the *weighting potential*:  $\mathbf{E}_n(\mathbf{x}) = \nabla \Psi_n(\mathbf{x})$ . In the case of two parallel electrodes, the weighting field is  $E_w = -\frac{d\Psi}{dx} = -1/d$ , where  $d$  is the distance between the electrodes. The resulting induced current is therefore

$$i(t) = \frac{q}{d} v_{\text{drift}}(x, t), \quad (2.7)$$

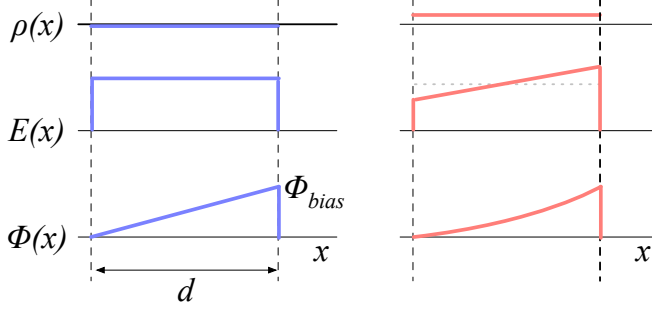


Figure 2.5: Left figure shows a profile of a diamond sensor only with an externally applied electric field. In the figure on the right a uniformly distributed space charge is added in the diamond, contributing to the internal electric field distribution. The induced current signal is proportional to the electrical field.  $d$  is the thickness of the diamond sensor.

whereby  $v_{\text{drift}}$  is the drift velocity of the point-like charge.  $d$  is defined by the dimensions of the sensor. The drift velocity is a function of the externally applied electric field, as defined in section 2.3. If the electric field is set to a constant value, the induced current is directly proportional to the drifting charge. By integrating the current the number of moving charges can be deduced:

$$Q = \int i(t)dt. \quad (2.8)$$

### 2.2.3 Thermal excitation

Electrons can be thermally excited to the conduction band. The intrinsic concentration of thermally excited electrons  $n_i$  in semiconductors is proportional to [24]

$$n_i \propto \exp\left(-\frac{E_g}{2k_B T}\right) \quad (2.9)$$

wherein  $k_B = 1.381 \times 10^{-23} \text{ m}^2 \text{ kg s}^{-2} \text{ K}^{-1}$  is the Boltzmann constant,  $E_g$  is the energy band gap of the semiconductor and  $T$  is the temperature in K. Due to the small band gap in semiconductors a significant amount of electrons already occupies the conduction band at room temperature due to thermal excitation, according to the probabilistic distribution. To reduce this effect semiconductor sensors are doped with donors and acceptors, forming a diode [24]. The diode is then inversely biased to deplete the material of all free charges. Doped silicon fulfils most of the needs for particle physics requirements and is therefore the most widely used material for particle detection. Diamond with its high energy band gap on the other hand only has a negligible number of thermally excited electrons at room temperature. Therefore a p-n junction is not needed, which simplifies the sensor production. In addition, heavy irradiation degrades p-n junctions. To prevent a thermal runaway the sensors need to be cooled. Diamond on the other hand does not need a complex cooling system, which reduces the production cost.

### 2.2.4 Space charge

Gauss law states that

$$\frac{d^2\Phi(x)}{dx^2} = \frac{dE(x)}{dx} = \frac{\rho(x)}{\epsilon} \quad (2.10)$$

where  $\rho(x)$  is the space charge distribution,  $E$  is the electrical field and  $\Phi$  is the voltage potential. In an ideal diamond, the externally applied high voltage potential on the two electrodes decreases linearly through the sensor. The electrical field is therefore constant throughout the sensor and the space charge distribution across it equals 0. However, space charge may be introduced in the material either by means of accumulating of charge carriers in the lattice or already during sensor production. Space charge can be either permanent or changing – sometimes it is possible to reduce it, as is shown in chapter 3. All in all, it is very important to reduce it because it affects the shape of the electrical signal. Since the drift velocity of the charge carriers is proportional to the electrical field, the charges change their velocity while drifting through the space charge region. Figure 2.5 compares the voltage potential, the electrical field and the space charge for an ideal sensor as well as for that with a uniformly distributed positive space charge.

### 2.3 Carrier transport in a diamond sensor

This section describes the carrier transport phenomena in diamond. This theory provides the basis for discussion about the measurements in chapter 3. Table 2.1 compares the properties of diamond and silicon. Some of these values are revisited and used in the course of this thesis.

Property	Diamond	Silicon
Band gap energy $E_g$ (eV)	5.5	1.12
Electron mobility $\mu_e$ ( $\text{cm}^2 \text{ V}^{-1} \text{ s}^{-1}$ )	1800 [33]	1500 [24]
Hole mobility $\mu_h$ ( $\text{cm}^2 \text{ V}^{-1} \text{ s}^{-1}$ )	2500 [33]	450 [24]
Breakdown field ( $\text{V cm}^{-1}$ )	$10^7$	$3 \times 10^5$
Resistivity ( $\Omega \text{ cm}$ )	$> 10^{11}$	$2.3 \times 10^5$
Intrinsic carrier density ( $\text{cm}^{-3}$ )	$< 10^3$	$1.5 \times 10^{10}$
Mass density ( $\text{g cm}^{-3}$ )	3.52	2.33
Atomic charge	6	14
Dielectric constant $\epsilon$	5.7	11.9
Displacement energy (eV/atom)	43	13 – 20
Energy to create an e-h pair (eV)	13	3.6
Radiation length (cm)	12.2	9.6
Avg. signal created/ $\mu\text{m}$ (e)	36	89

Table 2.1: Comparison diamond – silicon [24, 33].

When the charge carriers are freed in a semiconductor with no space charge and without an externally applied electric field, they scatter in random directions with a thermal velocity  $v_{\text{th}}$  [24]. Their integral movement due to thermal excitation equals zero.

**Diffusion** is caused by the concentration gradient. In its presence the integral movement is in the direction of the lower concentration until an equilibrium is reached. The concentration profile dissolves with time forming a Gaussian distribution with variance  $\sigma(t) = \sqrt{Dt}$  [24].

**Drift** is caused by an externally applied electrical field. In that case the carriers move along the field lines.

**Drift velocity**  $v_{\text{drift}}(E)$  is the speed at which the charge carriers drift through the diamond sensor [24].

**Mobility**  $\mu$  is a proportionality factor between the  $v_{\text{drift}}$  and the electric field  $E$  at low electric fields:  $v_{\text{drift}} = \mu(E)E$ . Its units are in  $\text{cm}^2 \text{ V}^{-1} \text{ s}^{-1}$ .

**Phonon transport** is the transfer of energy of the moving charges to the lattice.

**Saturation velocity**  $v_{\text{sat}}^e$  is a velocity limit above which the carriers cannot reach. This is due to increasing phonon scattering at a high electric field. The  $v_{\text{sat}}^e = v_{\text{sat}}^h = (14.23 \pm 0.12) \times 10^6$  cm/s for both positive and negative charge carriers has been derived from the measurements in [34]. The approximation for  $v_{\text{drift}}$  is [35]

$$v_{\text{drift}}(E) = \mu(E)E \sim \frac{\mu_0 E}{1 + \frac{\mu_0 E}{v_{\text{sat}}}}. \quad (2.11)$$

It can be retrieved experimentally via the transit time measured with the Transient Current Technique (TCT) [36]. This technique enables the measurement of transit time  $t_t$  of the carriers through the sensor with the thickness  $d$ .

$$v_{\text{drift}}(E) = \frac{d}{t_t(E)}. \quad (2.12)$$

The velocities for holes and electrons usually differ. In diamond, the holes travel approximately 30 % faster than electrons at room temperature [33].

## 2.4 Radiation-induced current signals

When a highly energetic particle travels through the sensor, it interacts with atoms in the lattice. It ionises the valence electrons, creating electron-hole (e-h) pairs on its way. It can either deposit only a fraction of its energy and exit the sensor on the other side or it can get stopped in the sensor, depositing all of its energy. A special case is when it interacts with the core of the atom in the bulk of the sensor by means of a nuclear interaction. All these various types of interactions produce different amounts and different spatial distributions of e-h pairs.

The two most frequent types are shown in figure 2.6. The first figure shows the interaction of an incident minimum-ionising particle – MIP. The electrons and holes created all along the trajectory of the particle immediately start drifting towards the positive and negative electrode, respectively. At  $t = 0$  all charges drift, contributing to the maximum induced current. Those closest to the electrodes have a very short drift path. They stop inducing current upon reaching the electrode. The resulting current signal is a triangular pulse with a sharp rising edge and a linear falling edge. Gradually all the charge carriers reach the electrode. The accumulated charge  $Q_s$  equals to the sum of the contributions of the positive and negative charge carriers drifting through the sensor.

The second type of interaction happens when the particle is stopped in the diamond close to the point of entry. Most of its energy is deposited in a small volume close to the electrode. A cloud of charge carriers is created and the charges with the shorter path to the electrode disappear almost instantly. The carriers of the opposite charge, however, start drifting through the sensor to the other electrode. In an ideal diamond sensor, their velocity is constant throughout the drift up until they are collected at the opposite electrode. The contribution of the first charge cloud is a short peak. The cloud drifting through the sensor, on the other hand, induces a current signal with a flat top. The resulting signal has a shape of a rectangle, with a spike in the beginning. The accumulated charge  $Q_s$  is equal to a half of the deposited charge by the stopped particle.

The two aforementioned types of interactions have well defined signal responses. Nuclear interactions on the other hand yield various results. The resulting signal shape depends on the decay products of the interaction, which can be  $\alpha$ ,  $\beta$  or  $\gamma$  quanta or other nuclei, inducing a mixed shaped signal.

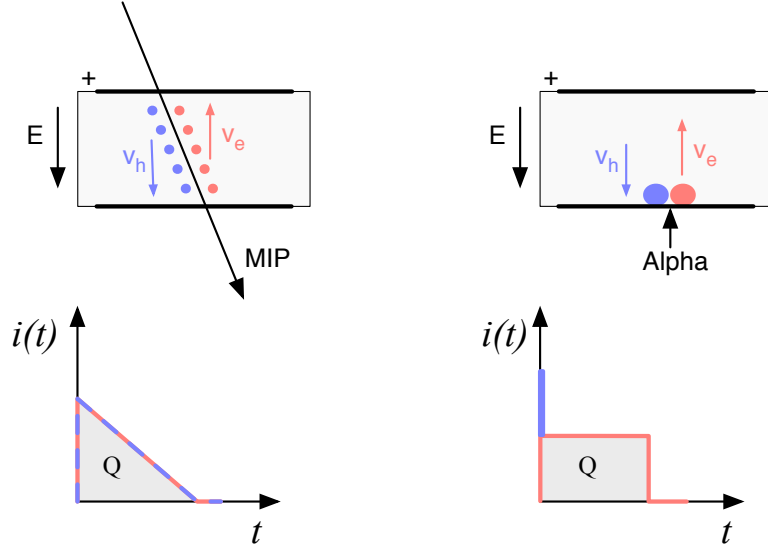


Figure 2.6: Charge carrier drift in diamond for  $\beta$  and for  $\alpha$  particles crossing the sensor at  $t = 0$ .

#### 2.4.1 Mean energy loss

The energy that a particle traversing the sensor deposits is dependent on its mass and velocity. A mean energy loss of a particle traversing the detector as a function of the momentum is given with the Bethe-Bloch equation [37]:

$$-\left\langle \frac{dE}{dx} \right\rangle = \frac{4\pi}{m_e c^2} \cdot \frac{n z^2}{\beta^2} \cdot \left( \frac{e^2}{4\pi\epsilon_0} \right)^2 \cdot \left( \ln \left( \frac{2m_e c^2 \beta^2}{I \cdot (1 - \beta^2)} \right) - \beta^2 \right) \quad (2.13)$$

The resulting function is shown in figure 2.7. The  $x$  axis is calculated for muon mass. At a momentum of around 300 MeV/c an incident muon deposits the lowest amount of energy. Hence it is referred to as the *minimum ionising particle*. The longer it travels through the material, the more it slows down and the faster it loses the energy. Such an energy deposition curve is referred to as a Bragg peak [38].

#### 2.4.2 Signal fluctuation

Two important sensor properties are the magnitude of the signal and the fluctuations of the signal at a given absorbed energy. They determine the relative resolution  $\Delta E/E$ . For semiconductors the signal fluctuations are smaller than the simple statistical standard deviation  $\sigma_Q = \sqrt{N_Q}$ . Here  $N_Q$  is the number of released charge pairs, i.e. the ratio between the total deposited energy  $E_0$  and the average energy deposition  $E_i$  required to produce an electron-hole pair. [39] shows that the standard deviation is  $\sigma_Q = \sqrt{F N_Q}$ , where  $F$  is the Fano factor [39] (0.08 for diamond and 0.115 for silicon [40]). Thus, the standard deviation of the signal charge is smaller than expected,  $\sigma_Q \approx 0.3 \sqrt{N_Q}$ . The resulting intrinsic resolution of semiconductor detectors is

$$\Delta E_{\text{FWHM}} = 2.35 \Delta E = 2.35 \sqrt{F E_i} \quad (2.14)$$

wherein  $E_i(Si) = 3.6$  eV and  $E_i(Di) = 13$  eV. E.g., for an  $\alpha$  particle with energy  $E_\alpha = 5.5$  MeV the calculated resolution in diamond is equal to  $\Delta E_{\text{FWHM}} = 5.6$  keV. This defines the minimum achievable resolution for energy spectroscopy with semiconductors.

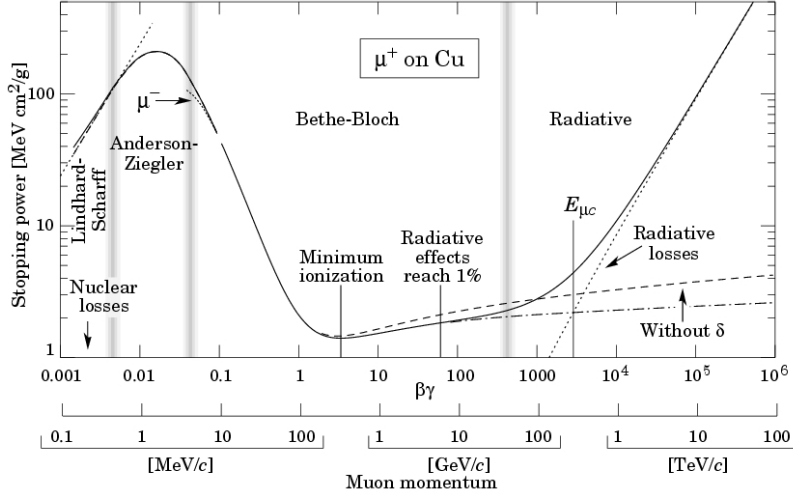


Figure 2.7: Stopping power according to the Bethe-Bloch formula [37].

### 2.4.3 Charge collection

The total measured charge  $Q_i$  is the integral of the induced current:

$$Q_i = \int i_{\text{ind}}(t) dt. \quad (2.15)$$

The expected charge  $Q_0$  can be calculated using the thickness of the sensor  $d$  and the average number of e-h pairs created per  $\mu\text{m}$   $\delta_d$ , which is 36 eh/ $\mu\text{m}$  for diamond according to table 2.1. The expected charge created by a MIP flying through a sensor with a thickness  $d = 500 \mu\text{m}$  perpendicular to the electrodes is

$$Q_{\text{MIP}} = \delta_d \cdot d \cdot q = 18 \times 10^3 \text{ eh} \cdot q = 2.9 \text{ fC} \quad (2.16)$$

where  $q = 1.6 \times 10^{-19} \text{ C}$  is the elementary charge. If a particle stops in the sensor, it deposits all its energy. In this case the number of created e-h pairs is calculated according to equation 2.17 using  $E_{\text{eh}}$ , the energy required to create an e-h pair. For diamond this value is 13 eV according to table 2.1. For a 5.5 MeV  $\alpha$  particle emitted from an  $^{241}\text{Am}$  source the expected charge is

$$Q_\alpha = \frac{E}{E_{\text{eh}}} \cdot q = \frac{5.5 \text{ MeV}}{13 \text{ eV}} \cdot q = 4.25 \times 10^5 \text{ eh} \cdot q = 68 \text{ fC}. \quad (2.17)$$

where  $E$  is the energy of the incident particle, which is almost for a factor of 24 larger than expected charge of a MIP. The charge collection efficiency (CCE) is the ratio between the measured and expected charge:

$$CCE = \frac{Q_i}{Q_0} = \frac{Q_i}{\delta_d \cdot d} \cdot 100\%. \quad (2.18)$$

The charge collection distance (CCD) is a measure of an average path that the charge carriers travel before getting trapped:

$$CCD = \frac{Q_i}{\delta_d} \quad (2.19)$$

and is given in units of  $\mu\text{m}$ .

Carriers that get trapped stop contributing to the overall induced current on the electrodes. The more charges are trapped along their drift path, the more the current induced on the electrodes is

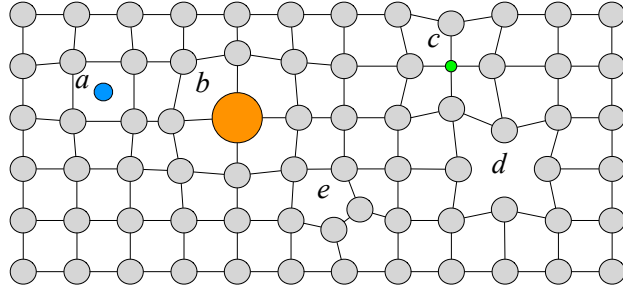


Figure 2.8: Impurities and non-uniformities in the crystal lattice due to radiation damage.

decreased. This in turn yields a lower integrated charge. An expected CCE for non-irradiated sCVD diamonds is close to 100 %. For highest quality non-irradiated pCVD diamonds it ranges between 40 % and 60 %. In other words, high-quality pCVD diamonds already have traps introduced by means of grain boundaries, which are created in the growing process, as well as some impurities, e.g. nitrogen. Traps can also be created by damaging the diamond using radiation (discussed in section 2.5). The more the sensor is irradiated, the larger number of traps is introduced in the material and the higher is the probability that the carriers are stopped on the way, reducing in turn the integrated charge. Therefore the CCD and CCE can be used as a means to quantify the detector damage due to radiation.

#### 2.4.4 Charge trapping

Various types of lattice defects can be created in diamond, similar to those in silicon [41]. Figure 2.8 shows several examples of lattice damage:

- a) foreign interstitial (e.g. H, Li),
- b, c) foreign substitutional (e.g. N, P, B),
- d) vacancy and
- e) self interstitial.

These non-uniformities form new energy levels in the band gap. These intermediate levels can trap moving charge carriers. Different types of lattice damage have different energy levels. The carriers trapped in a shallow trap – an energy level close to the conduction band – have a high probability of being thermally excited back into the conduction band whereby they continue drifting towards the electrode. Their activation energy is therefore low. Those trapped in a deep trap close to the middle of the band gap need a much higher activation energy, which in turn increases the average time to their release due to thermal excitation.

The energy band jumping goes the other way, too. The carriers in the valence band may use the intermediate energy levels as “stepping stones” to jump to the conduction band and start drifting in the externally applied electric field. These intermediate energy levels are referred to as the generation centres of leakage current.

The charge carriers that drift through the bulk get stopped in the charge traps with a certain probability. The trapping probability is proportional to the density of traps. In pCVD diamond, the charge trapping is the highest on the substrate side (CCD $\sim$ 0) and is gradually reduced towards the growth side.

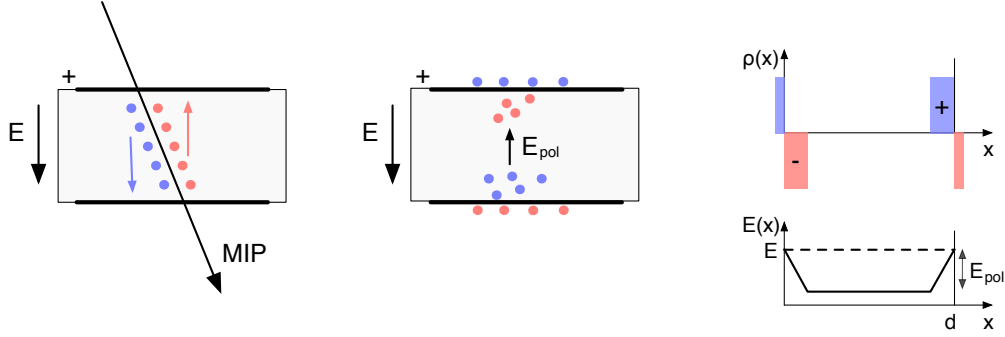


Figure 2.9: Polarisation due to space charge. The dashed line represents the contribution of the externally applied electric field. The built up space charge reduces the field in the middle of the sensor.

In the case of uniform trapping in sCVD diamond, the number of carriers in the moving charge cloud is gradually reduced. This in turn reduces the induced current. The number of drifting carriers per unit of length follows a decaying exponential function

$$I(t) = I_0 + I(0) \cdot e^{-\frac{t-t_0}{\tau}}, \quad (2.20)$$

where  $I(0)$  is the initial induced current,  $I_0$  is the end current,  $t$  is time,  $t_0$  is temporal displacement of the pulse and  $\tau$  is the decay time constant. This value describes how long it takes before the amplitude of the pulse decreases to 63 % of its initial height.

#### 2.4.4.1 Polarisation

Space charge may be introduced in the material by means of accumulating of charge carriers in local defects (i.e. charge trapping) or in the interface between the diamond and the metal electrode. The accumulated space charge deforms the electric field. This process is referred to as *polarisation* [42].

An example of creation of polarisation is with a MIP particle shown in figure 2.9. The created electrons and holes drift towards their respective electrodes. The amount of trapped charge is proportional to the density distribution and so the holes tend to get trapped close to the negative electrode and vice versa. The electric field formed by the trapped charge counteracts the applied electric field, leading to a reduced field in the centre of the diamond bulk. Since the electrodes are connected to a current source they charge up more due to electrostatic induction. The externally applied HV is conserved and so is the integral over the electric field. The reduction of the electric field in the centre of the bulk is compensated by an increase in electric field close to the electrodes. The actual shape of the electric field is defined by the distribution of space charge, which itself depends on the type and distribution of traps, the trapping and de-trapping times, the type of incident radiation and the rate at which charge carriers are created.

This effect is undesirable because it affects the shape of the electrical signal. Since the drift velocity of the charge carriers is proportional to the electrical field, the charge carriers change their velocity while drifting through the space charge region. As discussed in [42], the main techniques to reduce polarisation are to either increase or alternate the bias voltage or to use a UV light to excite and release the trapped charges. Chapter 3 investigates several other procedures.

#### 2.4.4.2 Priming/pumping

Priming or pumping [43] is a process of irradiating the diamond with ionising radiation with a goal to improve the sensor properties. The priming process strongly reduces the concentration of active carrier trapping centres. This leads to an enhancement of electronic properties of such material. The improved transport properties due to a reduced number of active charge traps give rise to an increased charge collection efficiency. Diamond is usually primed for several hours using a strong  $\beta$  source, preferably a  $^{90}\text{Sr}$  source with the activity of at least 50 MBq. It then remains primed from a few minutes to several days, depending on the quality of the material. A direct exposure to light results in an immediate return to an non-primed state.

## 2.5 Radiation damage

Exposure to radiation degrades sensors by deforming the crystal lattice and introducing charge traps in the material.

Radiation damage varies with the type of radiation and its energy. There are several models existing [44, 45] that try to explain the impact of irradiation and to provide *damage factors* to compare the radiation damage between different particles. The standard way is to convert the fluence into *1 MeV neutron equivalent fluence* [46]. Some models have been extensively verified with simulations and with experiments. In these experiments the charge collection in sensors is measured before and after irradiation. This procedure is repeated several times, with a measurement point taken after every irradiation. Then the charge collection for this set of measurements is plotted as a function of fluence by a specific particle at a specific energy. From this a damage constant can be extracted, as shown in section 2.5.1. Damage constants have to be measured across a range of energies and types of radiation to properly quantify the damage in the sensors.

Diamond is an expensive material and the technology is relatively new as compared to silicon. Therefore few institutes are carrying out diamond irradiation studies. To join the efforts, the RD42 collaboration [47] has been formed. It gathers the experimental data from diamond irradiation studies.

Sensors degrade via non-ionising energy loss (NIEL). Unlike with silicon, the experimental results for diamond so far show no significant correlation with the NIEL (non-ionising energy loss) model [44], which correlates detector efficiency with the number of lattice displacements.

Therefore an improved model with parameters tuned for diamond material was proposed [45], correlating the diamond efficiency with the number of displacements per atom (DPA) in the material, taking recombination into account while omitting the phonon interactions. The displacement energy (see table 2.1), which is three times higher in diamond than in silicon, is the major contributor to the different behaviour of the two sensor materials.

If the energy transfer from an incident particle to the nucleus of an atom in the lattice is higher than the lattice binding energy (i.e. displacement energy), the atom is displaced from its original position. The newly formed vacancy may act as a trap for drifting charge carriers. The more displacements that form in the crystal, the higher is the probability that a drifting carrier gets trapped. However, different types of particles interact differently with the material. In addition, the mechanisms of interaction at low energies are different to those at high energies. To assess the damage for individual particles at a range of energies, simulations need to be run first. The simulation shown in [45] shows the DPA model for a range of energies of proton, pion and neutron irradiation in diamond. Figure 2.10 contains the simulation results as well as the superimposed empirical results of several RD42 irradiation campaigns. According to the figure, a 300 MeV pion

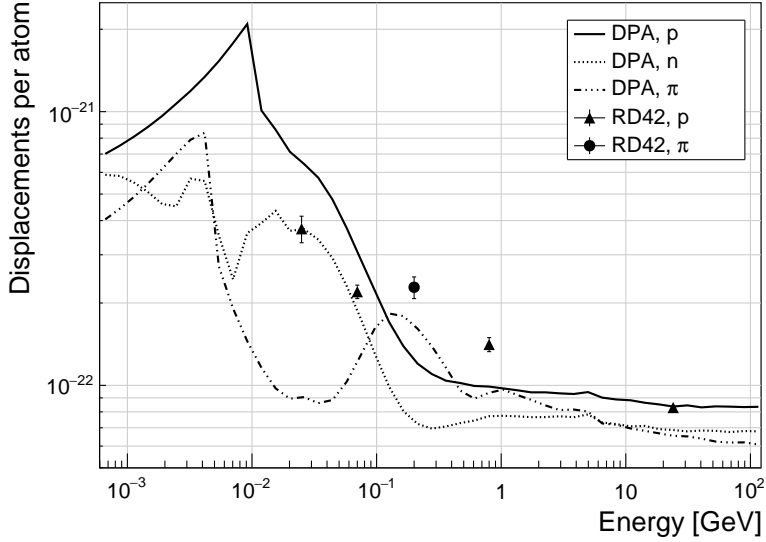


Figure 2.10: Diamond radiation damage - a model based on displacements per atom [45]. The figure shows the DPA as a function of the kinetic energy for protons, neutrons and pions. Added are data points for protons and pions by RD42 [48].

beam damages the diamond material twice as much as a 24 GeV proton beam. RD42 data points have been normalised to damage by 24 GeV protons. This value has been chosen because radiation damage at this energy and radiation type is well understood at CERN and within the high-energy physics community.

### 2.5.1 Irradiation damage factor

The irradiation damage factor  $k_\lambda$  is a means to quantify irradiation damage of a specific type of radiation at a specific energy. Via this factor different types of irradiation can be compared. It is obtained experimentally by measuring the CCD of a number of samples at various irradiation steps and fitting the equation 2.21 to the data.  $\lambda$  is the measured CCD,  $\lambda_0$  is the CCD of a non-irradiated sample and  $\Phi$  the radiation dose. As a reference, the damage factor for 24 GeV protons is set to  $1 \times 10^{-18} \mu\text{m}^{-1} \text{cm}^2$ .

$$\frac{1}{\lambda} = \frac{1}{\lambda_0} + k_\lambda \cdot \Phi \quad (2.21)$$

## 2.6 Temperature effects

The band gap energy in diamond is equal to  $E_g = 5.5$  eV while the average energy to produce an electron-hole pair is  $E_{\text{eh}} = 13$  eV. This means there is excessive energy deposited in the diamond bulk. An incident 5 MeV  $\alpha$ -particle stops within  $\sim 10\text{--}15 \mu\text{m}$  of the bulk, transferring all its energy to the lattice during deceleration. A part of this energy directly ionises the carbon atoms, creating free electron-hole pairs.

The remaining energy, however, is converted into lattice vibrations – phonons [49, 33]. In other words, the lattice within the ionisation volume of approximately  $\sim 15 \mu\text{m} \times \sim 2 \text{ nm}$  [33] is briefly

heated up. The hot plasma then cools down to the temperature of the surrounding material by means of heat dissipation, i.e. phonon transport.

A free electron may bind with a free hole into a bound state (not recombination) – the exciton [50]. The exciton binding energy is 80 meV, which introduces an energy level within the band gap just under the conduction band. At higher temperatures (e.g. room temperature) the lattice provides enough energy to thermally excite the electron from the exciton state back to the conduction band. At lower temperatures, however, the exciton lifetime increases, which means that it takes longer for the electrons to get re-excited to the conduction band. The re-excitation lifetime at room temperature is  $\sim$ 30 ps, increasing to  $\sim$ 150  $\mu$ s at 50 K [33]. This means that some of the bound electrons do not even start drifting within the period of  $\sim$ 10 ns, which is the expected carrier drift time. Some are finally freed (dissociated), but at that point the drift-induced current is so low that it is hidden in the electronics noise. Other may even recombine and therefore do not drift. The effective area of the measured current pulse is therefore smaller than that of a pulse induced by all the carriers drifting at the same time. This in effect reduces the measured collected charge. The longer the time constant, the lower the measured collected charge, as shown in section 3.4.2.1.

### 2.6.1 Collected charge as a function of temperature

The area below the current pulse is proportional to the charge collected by the diamond detector. The collected charge is measured as a function of temperature. First, the amplitude values of the averaged pulses at a bias voltage of  $\pm$ 500 V and across the temperature range between 4 K and 295 K have to be integrated. Then a calibration factor is used to derive the charge for all data points. The results of such measurements have been presented in [33]. Chapter 3 shows the results of the measurements taken in the scope of this thesis.

## 2.7 Electronics for signal processing

This section describes the electronics of a detector, starting with a description of signal amplifiers and then discussing the digitisation and signal processing. All these stages are necessary to extract information from the sensor. First, the signal has to be amplified. Then it is digitised and finally processed in a specially designed processor or a logic unit. A more detailed description of the detector chain can be found in [51].

### 2.7.1 Signal preamplifiers

The signal charge generated in the sensor by a single energetic particle is of the order of a few fC. The range of the induced current for single particles is typically between  $10^{-7}$  A ( $\beta, \gamma$  radiation) and  $10^{-6}$  A ( $\alpha$  radiation), assuming pulse lengths of 10 ns (measured values available in chapter 3). Signals as low as these have to be pre-amplified before processing. Depending on the measurement, several types of signal amplifiers can be used. The preamplifiers are designed to minimise electronic noise while maximising gain, thus maximising the signal-to-noise ratio (SNR). In addition, a bandwidth limit must be optimised to minimise the information loss due to signal shape deformation. A critical parameter is the total capacitance, i.e. the sensor capacitance together with the capacitance load of the preamplifier. The SNR improves with a lower capacitance. Several types of amplifiers can be used, all of which affect the measured pulse shape. Two preamplifiers are used most commonly, a current and a charge sensitive amplifier. Both are described below.

### 2.7.1.1 Current amplifier

Figure 2.11a shows the equivalent circuit of a current source and a current amplifier. An amplifier operates in current mode if the source has a low charge collection time  $t_c$  with respect to the  $R_i C_d$  time constant of the circuit. In this case the sensor capacitance discharges rapidly and the output current  $i_o$  is proportional to the instantaneous current  $i_i$ . The amplifier is providing a voltage gain, so the output signal voltage  $u_o$  is directly proportional to the input voltage  $u_i$ :

$$u_o(t) = A \cdot R_i \cdot i_i(t), \quad (2.22)$$

whereby  $i(t)$  is the induced current calculated using the Shockley-Ramo theorem.

The detector capacitance  $C_d$  together with the input resistance of the amplifier  $R_i$  defines the time constant of the signal, as shown in figure 2.11b. The higher  $C_d$ , the slower is the response of the amplifier. For the case of the diamond sensor, which has the capacitance of the order of 2 pF [52] and the input resistance of 50  $\Omega$ , the resulting time constant is  $\tau = 10^{-10}$  s. This yields the signal rise time  $t_r \sim 2.2\tau = 2.2 \times 10^{-10}$  s.  $t_r$  is a function of the input bandwidth limit:

$$t_r = \frac{0.34}{\text{BW}} \quad (2.23)$$

where BW is the cutoff frequency. To ensure that the signal is not distorted significantly, the  $t_r$  must be shorter than 10 % of the pulse width:

$$t_r < \frac{\text{FWHM}}{10}. \quad (2.24)$$

For a 500  $\mu\text{m}$  thick diamond with a bias voltage of 500 V and electron collection, the drift velocity is  $v_{\text{drift}} = 6 \times 10^6 \text{ cm/s}$  [33]. An  $\alpha$  particle with the energy of 5.5 MeV induces a current

$$i(t) = \frac{Q}{d} v_{\text{drift}} = 8 \mu\text{A} \quad (2.25)$$

where  $Q=68 \text{ fC}$  according to equation 2.17. The drift time  $t_{\text{drift}}$  of charge carriers through the sensor equals the pulse FWHM and is

$$\text{FWHM} = t_d = \frac{d}{v_{\text{drift}}} = 8.3 \text{ ns}, \quad (2.26)$$

which means that the maximum rise time must be  $t_r = 0.83$  ns according to equation 2.24. The minimum bandwidth limit for observing  $\alpha$  pulses for such a system is therefore 400 MHz according to equation 2.23.

### 2.7.1.2 Charge-sensitive amplifier

In order to measure integrated charge in the sensor, a feedback loop is added to the amplifier, as shown in figure 2.12a. The feedback can be used to control the gain and input resistance, as well as to integrate the input signal. The charge amplifier is in principle an inverting voltage amplifier with a high input resistance.

In an ideal amplifier the output voltage  $u_o$  equals  $-Au_i$ . Therefore the voltage difference across the capacitor  $C_f$  is  $u_f = (A + 1)u_i$  and the charge deposited on the capacitor is

$$Q_f = C_f u_f = C_f (A + 1) u_i. \quad (2.27)$$

Since no current can flow into the amplifier, all of the signal current must charge up the feedback capacitance, so  $Q_f = Q_i$ .

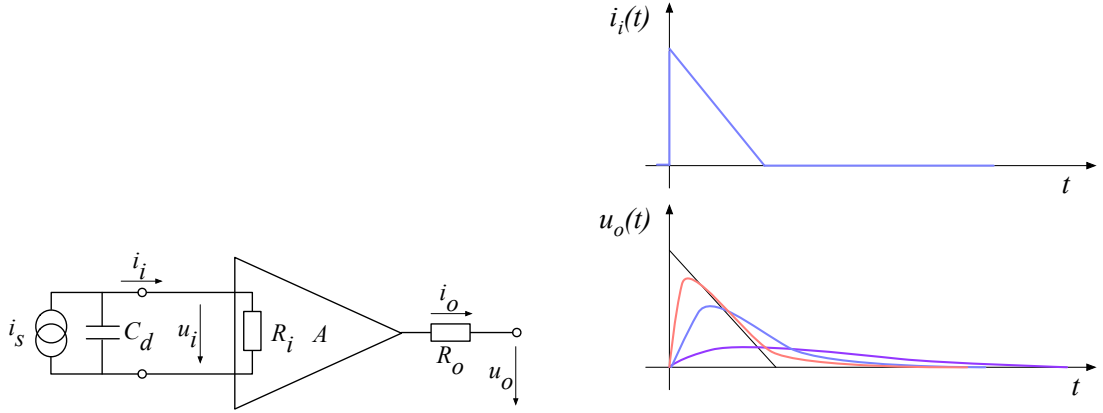


Figure 2.11: Left: a simplified equivalent circuit of a current amplifier. Right: an input and an output signal of the current amplifier. The black line represents the output at  $C_d = 0$  whereas the red, blue and purple line show the response for increasing  $C_d$ .

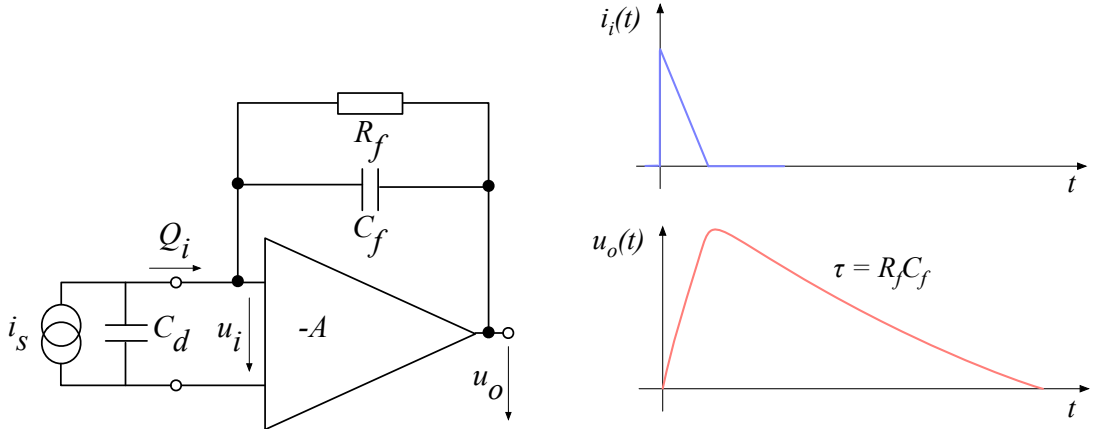


Figure 2.12: Left: a simplified equivalent circuit of a charge amplifier. Right: an input and an output signal of the charge amplifier.

In reality, however, the response of charge-sensitive amplifiers is much longer than duration of the current pulse from the sensor. In addition, a resistor is added to the feedback line in parallel to the capacitor. The resistor and capacitor define the decay time constant of the pulse, as shown in figure 2.12b. This is necessary to return the signal to its initial state to be ready for a new measurement.

A MIP deposits 2.88 fC in a 500  $\mu\text{m}$  thick diamond. In a pCVD diamond sensor with a quoted CCE of 35 % the most probable value (MPV) of the collected charge is 1 fC. The low and high end (the latter only due to cut-off for high amplitudes) of the Landau distribution are at  $\frac{2}{3} \times \text{MPV}$  and  $10 \times \text{MPV}$ , therefore at 0.67 fC and 10 fC. To ensure a good separation between the noise floor and the signal, the noise RMS (root-mean-square) must be 5 times lower than the signals with the lowest charge deposition – below 0.133 fC, which equals 836  $e^-$ . For an amplifier with the gain of

10 mV/fC with such a noise floor, the voltage noise RMS on the output is 1.3 mV.

### 2.7.2 Analogue electronic noise

The electronic noise determines the ability of a system to distinguish different signal levels. The analogue signal contains ample information about the type and energy of incident radiation, which can quickly be erased or altered if the signal properties change. Therefore the noise contributions to the signal must be well understood to qualify the information the signal is carrying. In electrical circuits there are five common noise sources:

- Thermal noise
- Shot noise
- Flicker noise
- Burst noise
- Avalanche noise.

The last two contributions can be eliminated if present, so the focus is on the first three.

Considering  $n$  carriers of charge  $e$  moving with a velocity  $v$  through a sample of length  $l$ , the induced current  $i$  at the ends of the sample is

$$i = \frac{Q \cdot v_{\text{drift}}}{d} = \frac{nev}{d} \quad (2.28)$$

where  $d$  is the distance travelled. Two mechanisms contribute to the total noise: velocity fluctuations (thermal noise) and number fluctuations (shot noise, flicker noise). They are statistically uncorrelated and can therefore be added in quadrature.

**Thermal noise** or Johnson–Nyquist noise [53, 54] is the dominant noise contribution in the use case for diamond detector signal amplification and therefore defines the limitations of the detector system. This noise type is generated by the random thermal motion of charge carriers. The frequency range of the thermal noise is from 0 to  $\infty$  with a predominantly uniform distribution (white noise). The resulting signal amplitude has a Gaussian distribution. The spectral noise voltage density is

$$e_n^2 = 4k_B RT \quad (2.29)$$

where  $k_B$  is the Boltzmann constant,  $R$  is the input resistance of the amplifier and  $T$  its temperature. The total noise on the output depends on the frequency [30]:

$$u_{\text{on}}^2 = \int_0^\infty e_n^2 A^2(f) df. \quad (2.30)$$

Assuming a uniform gain across the frequency range between the low and the high cut-off  $\Delta f = f_{\text{max}} - f_{\text{min}}$ , the equation is simplified into

$$u_o = A \sqrt{4k_B RT \Delta f}, \quad (2.31)$$

where  $u_o$  is the RMS of the open-loop equivalent voltage. This equation shows that it is possible to reduce the noise RMS by either (1) reducing the input bandwidth, (2) reducing the resistance or (3) decreasing the temperature.

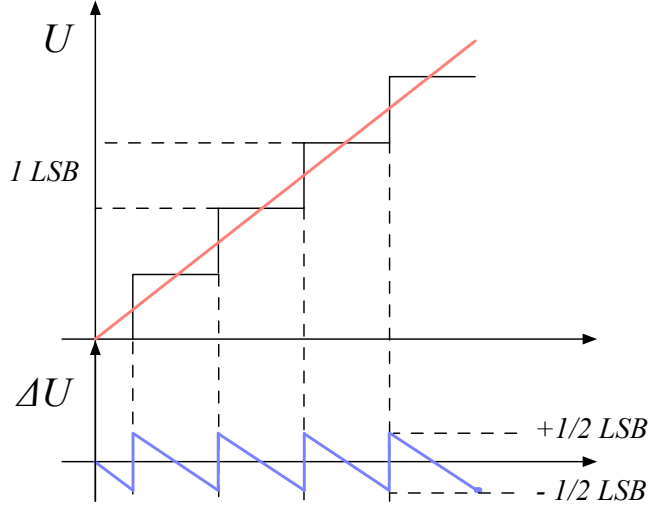


Figure 2.13: Input signal digitisation and quantisation error.

**Shot noise** or Poisson noise is a type of electronic noise which can be modeled by a Poisson process. It occurs whenever charge carriers are injected into a sample volume independently of one another. The spectral noise current density in this case is proportional to the DC current:

$$e_i^2 = 2qI. \quad (2.32)$$

**Flicker noise** occurs when charge carriers are trapped and then released after a characteristic time  $\tau$ . For a number of traps with different  $\tau$ , the spectral noise density yields a near  $1/f$  distribution [30]. This noise contribution becomes more pronounced in heavily irradiated sensors with a high number of introduced charge traps.

### 2.7.3 Analogue-to-digital converters

An analogue-to-digital converter (ADC) is a device that converts the analogue electrical signal on the input to its digital representation - a series of digital values. This involves a quantisation – *sampling* of the signal at a defined sampling period, resulting in a sequence of samples at a discrete time period and with discrete amplitude values. The resolution of the ADC is the number of output levels the ADC can quantise to and is expressed in bits. For instance, an ADC with a resolution equal to  $n = 8$  bit has a dynamic range of  $N = 2^n = 256$  steps. The resulting voltage resolution  $Q_{\text{ADC}}$  at the input voltage range of  $V_{\text{ADC}} = \pm 50$  mV is then

$$Q_{\text{ADC}} = \frac{V_{\text{ADC}}}{2^n} = \frac{100 \text{ mV}}{2^8 \text{ bit}} = 0.39 \text{ mV/bit}. \quad (2.33)$$

With a sampling period of  $t_s = 1$  ns the sampling rate is  $f_s = 1$  GS/s (gigasample per second).

**Quantisation error and quantisation noise** (or a round-off error) is a contribution to the overall measurement error due to digitisation (rounding). The quantisation error is defined as a difference between the actual analog value and the closest digitised representation of this value, therefore by the least significant bit (LSB), as seen in figure 2.13. The input signal amplitude is typically much

larger than the voltage resolution. In this case the quantisation error is not directly correlated with the signal and has an approximately uniform distribution. The probability density function  $P(x)$  therefore has a rectangular shape bounded by  $(-\frac{1}{2}\text{LSB}, \frac{1}{2}\text{LSB})$ :

$$P(x) = \begin{cases} \frac{1}{\text{LSB}}, & -\frac{1}{2}\text{LSB} \leq x \leq \frac{1}{2}\text{LSB} \\ 0, & \text{otherwise.} \end{cases} \quad (2.34)$$

The height equal to  $\frac{1}{\text{LSB}}$  preserves the integrated probability of 1. The variance of the distribution is

$$\sigma^2 = \int P(x)(x - \mu)^2 dx. \quad (2.36)$$

The population mean is  $\mu = 0$ , therefore

$$\sigma^2 = \int_{-\frac{1}{2}\text{LSB}}^{\frac{1}{2}\text{LSB}} \frac{1}{\text{LSB}} x^2 dx = \frac{x^3}{3\text{LSB}} \Big|_{-\frac{1}{2}\text{LSB}}^{\frac{1}{2}\text{LSB}} = \frac{\text{LSB}^2}{12}. \quad (2.37)$$

The RMS of the quantisation noise is defined as the square root of the variance:

$$\Delta Q_{\text{ADC}} = \sqrt{\sigma^2} = \frac{1}{\sqrt{12}} \text{LSB} \sim 0.289 \text{ LSB}. \quad (2.38)$$

For the example above the quantisation error equals  $\Delta Q_{\text{ADC}} = 0.11 \text{ mV}$ . The error depends strongly on the linearity of the ADC, but this is out of scope of this document as the devices used have ADCs with a sufficient linearity.

#### 2.7.4 Digital signal processing

The digitised signal can be processed to extract useful information. Therefore after the signal amplification and digitisation the signal is routed in a device which handles the digital analysis. The signal can either be processed immediately (in real time) or it can be saved to a data storage for analysis at a later stage (offline). Devices carrying out the processing can be multipurpose (e.g. Field Programmable Gate Arrays) or dedicated (e.g. Application-Specific Integrated Circuits).

**Field Programmable Gate Array** (FPGA) is an integrated circuit designed to be reprogrammable and reconfigured after manufacturing. It consists of a set of logic gates that can be interconnected in numerous combinations to carry out a set of logic operations. Many such logic operations can take place in parallel, making the FPGA a powerful tool for signal processing. FPGAs are often used during system development or in systems in which the requirements might change with time. They can be reprogrammed in the order of seconds. In addition, the logic design only needs minor changes when migrating to a newer version of the FPGA chip of the same vendor. FPGAs also offer a faster time-to-market with comparison to application-specific solutions, which have to be developed. On the other hand, the price per part can be significantly higher than for the application-specific solutions. Also, their other major disadvantages are a high power consumption and a relatively low speed as compared to more application-specific solutions. However, today's solutions are capable of clock speeds higher than 500 MHz. Together with the integrated digital signal processing blocks, embedded processors and other modules, they are already very powerful and versatile. All in all, FPGAs are a good choice for prototyping and limited production, for projects with limited requirements for speed and complexity.

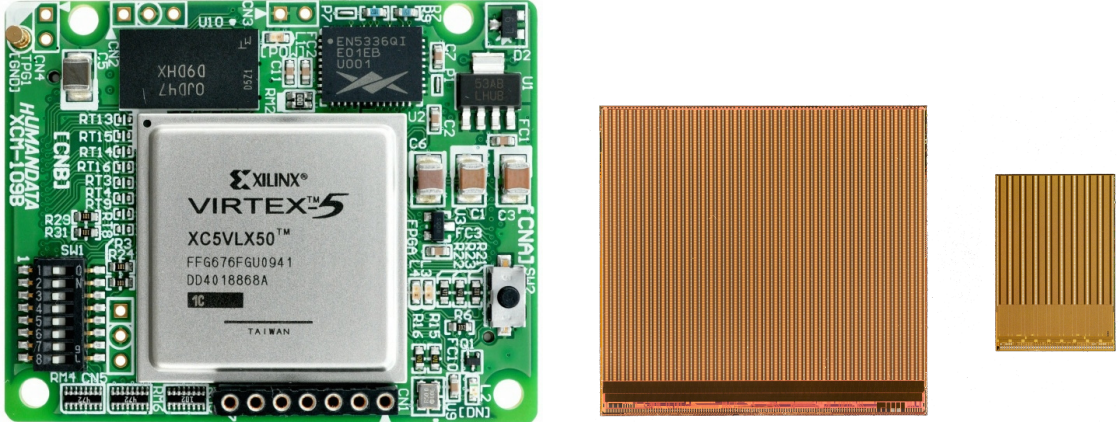


Figure 2.14: An example of a Xilinx Virtex 5 FPGA [55] and an FE-I4 and FE-I3 ASIC chip [56].

**Application-Specific Integrated Circuit** (ASIC) is an integrated circuit designed for a specific use. The design cannot be modified after chip production, as is the case with FPGAs. On the other hand, ASICs can be optimised to perform a required operation at a high speed and at a low power consumption. In addition, due to the specific design the size of the chip can be much smaller. ASICs can be designed as hybrid chips, containing both a digital and an analog part. Finally, ASICs can be designed to withstand much higher irradiation doses than FPGAs and can therefore be used in harsh environments like in space or in particle colliders. To update the chip, the design has to be submitted to a foundry, which produces new chips with a turnover time of several months. The costs of a submission are high, but the price per part can be reduced significantly with a high volume. To sum up, ASICs are used for high volume designs with well defined requirements where some stringent constraints in terms of power consumption and speed have to be met, or in the case where a high radiation hardness and/or a mixed analogue/digital signal processing are required.



## Chapter 3

# Diamond irradiation study

The aim of the study in this chapter is to find the operational limitations of diamond detectors for spectroscopy and tracking applications. The chapter contains the measurement results of data taken with diamond sensors. First the measurement setup is described in section 3.1. Then the measured particle spectra are shown in section 3.2. This is followed by a study of effects of the irradiation damage on the electrical signal of the diamond detector. The last section shows the results of the measurements of irradiated diamond samples at cryogenic temperatures. The studies compare the experimentally acquired data with the theory from the previous chapter and define limitations of the diamond detectors in terms of radiation and temperature.

Diamond sensors are mainly used for two types of measurements: particle counting and spectroscopy. The first type of measurements depends on the sensor efficiency – its ability to detect all or at least a known percentage of incident particles. The energy of the particles is not so important; what bears the information is the rate and the spatial distribution. Here the particles do not necessarily stop in the bulk – they exit the sensor with a slightly lower energy. In spectroscopy, on the other hand, the particles stop within the sensor, depositing all their energy. This energy is then measured by collecting the freed charge carriers. The goal of the experiments described in this chapter is to:

1. Quantify the charge collection efficiency of the sCVD diamond in counting mode,
2. Quantify the efficiency degradation as a function of fluence,
3. Quantify the macroscopic effects on charge carrier behaviour as a function of fluence and
4. Define limitations for use in spectroscopy.

The results discussed here show that there are several limitations for using diamond as a radiation detector. All of them need to be taken into account when designing a new measurement device. The irradiation study allows for an estimation of the lifetime of the detector and a prediction of the longterm signal degradation as a function of fluence. The result of the study is a correction factor, which can be applied during data analysis to ensure that the analysis results are stable despite the detector degradation.

### 3.1 Measurement setup

The first step of designing a measurement setup is to define the measurement conditions, such as temperature, type of radiation and its flux. The second step is to ensure that the setup is insensitive

### 3.1. MEASUREMENT SETUP

---

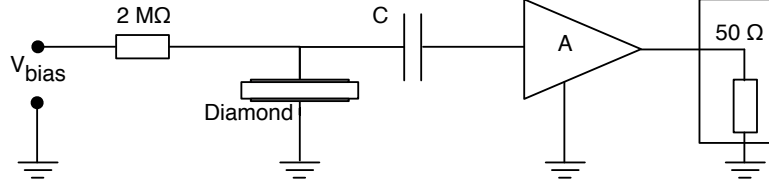


Figure 3.1: Diagram of a diamond detector readout chain.

to external electromagnetic interferences and that it minimises electrical noise in the system. The setup needs to be calibrated before use.

The measurements using diamond that are explained in these chapters have been carried out using several measurement setups, but they are all similar in terms of the electrical signal chain. The measurement chain consists of three main parts: a diamond sensor, a signal preamplifier and a readout device, as seen in figure 3.1. The preamplifier is capacitively coupled with the diamond. The signals propagating along the analogue chain are in the GHz bandwidth range with amplitudes of the order of tens of  $\mu\text{V}$ . This gives rise to the importance of shielding from external radio-frequency (RF) interferences. Also, the carrier and the preamplifier have to have a matched impedance. Finally, the system needs to be grounded properly.

#### 3.1.1 Preamplifiers

Two preamplifiers are used for the measurements. *CIVIDEC Cx* (figure 3.2a) is a charge sensitive amplifier. Its high SNR is achieved due to a low equivalent noise charge of  $300 \text{ e}^-$  with an additional  $30 \text{ e}^-$  per each pF of the sensor capacitance. A reported gain of  $\sim 12 \text{ mV/fC}$  makes it a good choice for spectroscopic measurements with diamond sensors. *CIVIDEC C2* (figure 3.2b) [51] is a fast current preamplifier with a 2 GHz bandwidth limit. Both are embedded in an RF-tight aluminium box to reduce the noise pickup. Both have an AC coupled input and a  $50 \Omega$  output.

A 2 GHz bandwidth limit defines the minimum rising time equal to  $t_r \simeq \frac{0.34}{BW} = \frac{0.34}{2 \times 10^9} = 170 \text{ ps}$ . A system with a CIVIDEC C2 amplifier is capable of measuring pulses with a minimum FWHM  $\simeq 170 \text{ ps}$ . In practice, this value is for a factor of 3 higher than the rise time, therefore  $\sim 500 \text{ ps}$ .

The initial peak in the  $\alpha$  pulse (shown in figure 2.6) has a lower FWHM; for example, if a positive charge carrier travelling through the bulk takes  $t_1 \sim 6 \text{ ns}$  to reach the electrode on the opposite side ( $d_1 \sim 500 \mu\text{m}$ ), the carrier with the opposite charge and a shorter path to the closer electrode – max.  $d_2 \sim 10 \mu\text{m}$  – only takes  $t_2 \sim \frac{d_2}{d_1} t_1 \times 140 \% = 170 \text{ ps}$  (higher percentage due to slower electron drift). Such a short drift time induces a current pulse that is too narrow for the system to detect.

##### 3.1.1.1 Calibration

The amplifiers were calibrated using a square signal generator with a known amplitude step of  $U_{\text{in}} = (252 \pm 5) \text{ mV}$ . A 2 GHz oscilloscope with a 10 GS/s sampling rate was used to carry out the calibration.

**Cx charge sensitive amplifier** calibration necessitates an injection of a well known charge. Therefore the signal from a pulse generator is routed through a capacitor with a calibration capacitance  $C_{\text{cal}} = (0.717 \pm 0.014) \text{ pF}$  and then to the input of the amplifier. The pulse area behind the capacitor is  $a_{\text{cal}} = (5.0 \pm 0.5) \text{ pVs}$ , with the signal amplitude on the output amounting to  $U_{C_x} = (1.95 \pm 0.05) \text{ V}$ .

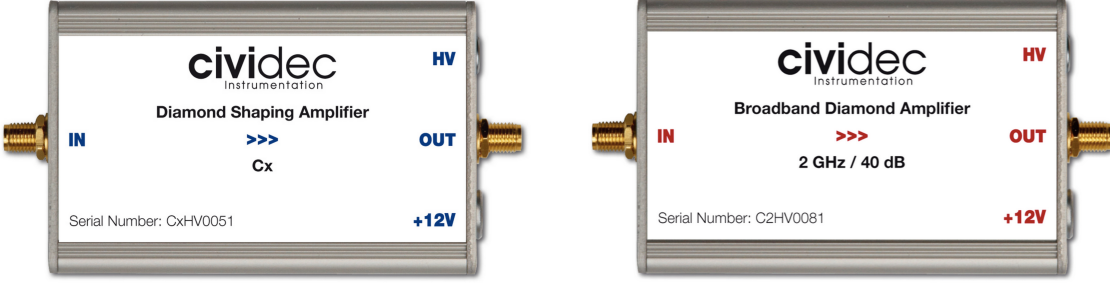


Figure 3.2: CIVIDEC Cx and CIVIDEC C2 amplifiers used for the charge and current measurements.

The input voltage step combined with the calibration capacitance yields a calibration charge

$$Q_{\text{cal}} = C_{\text{cal}} \cdot U_{\text{in}} = (181 \pm 5) \text{ fC}. \quad (3.1)$$

The gain of the Cx amplifier when comparing the integrated input charge to the output amplitude is

$$A_{\text{Cx}}^Q = \frac{U_{\text{Cx}}}{Q_{\text{cal}}} = (9.3 \pm 0.4) \text{ mV/fC} \quad (3.2)$$

whereas the factor between the area of the input current pulse and the output amplitude is

$$A_{\text{Cx}}^a = \frac{U_{\text{Cx}}}{a_{\text{cal}}} = (390 \pm 40) \text{ mV/pVs}. \quad (3.3)$$

The area-based amplification factor  $A_{\text{Cx}}^a$  can be used as an estimate for the integrated charge of a current pulse. However, it has a higher uncertainty ( $\sim 10\%$ ) than the amplitude-based factor  $A_{\text{Cx}}^Q$  ( $\sim 4\%$ ) due to the measurement limitations of the oscilloscope and to RC time constant uncertainty (see figure 2.11b).

**C2 current amplifier** calibration only requires the measurement of the amplitude gain. To keep the output signal amplitude within the  $\pm 1 \text{ V}$  linear range of the amplifier, the input signal amplitude has to be minimised. The signal from the generator is therefore routed through a 36 dB attenuator to decrease its amplitude to  $U_{\text{inAtt}} = (3.95 \pm 0.05) \text{ mV}$ . Two amplifiers with different gains have been measured, because both are used for the measurements. The output of the first amplifier amounts to  $U_{\text{C2-1}} = (860 \pm 5) \text{ mV}$ . This yields the amplification gain

$$A_{\text{C2-1}} = \frac{U_{\text{inAtt}}}{U_{\text{C2-1}}} = (217 \pm 3). \quad (3.4)$$

The second amplifier has the output equal to  $U_{\text{C2-2}} = (632 \pm 5) \text{ mV}$  with the resulting gain of  $A_{\text{C2-2}} = (152 \pm 3)$ .

### 3.1.2 Diamond samples

The sCVD diamond sensor samples used for these studies have been acquired from Element Six (E6) [57]. They all have the same standard dimensions of  $4.7 \times 4.7 \text{ mm}^2$ . One sample with dimensions of  $5.6 \times 5.3 \text{ mm}^2$  produced by IIa Singapore [58] has also been characterised at CERN [52]. The target thickness for all samples is  $500 \mu\text{m}$ . Table 3.1 shows all diamond samples used for this study. Two of them are measured before and after irradiation and then compared.

### 3.1. MEASUREMENT SETUP

---

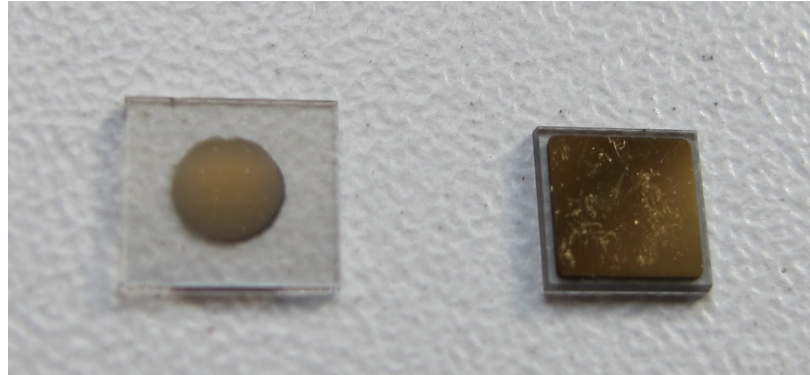


Figure 3.3: Two scCVD diamond samples: A IIa 1scdhq (left) and an E6 S37 (right).

Name	Type	Producer	Dimensions [mm <sup>2</sup> ]	Thickness [μm]	Electrode	Irradiated
S37	sCVD	E6	4.7 × 4.7	548	Cr/Au	no
S50	sCVD	E6	4.7 × 4.7	537	Cr/Au	no
S52	sCVD	DDL	4.7 × 4.7	515	DLC/Pt/Au	$3.6 \times 10^{14} \frac{\pi}{cm^2}$
S79	sCVD	E6	4.7 × 4.7	529	Cr/Au	$1 \times 10^{14} \frac{\pi}{cm^2}$
ELSC	sCVD	E6	4.7 × 4.7	491	Cr/Au	no
1scdhq	sCVD	IIa	5.6 × 5.3	460	Cr/Au	no

Table 3.1: Diamond sensor samples used.

The diamond samples have quoted impurity densities of  $\leq 2 \times 10^{14} \text{ cm}^{-3}$  and nitrogen incorporation of  $\leq 10^{-9}$  [33]. The electrodes were added by various companies and institutes. For instance, S52 was metallised by a company DDL (now defunct) while the Physics Department of the University of Firenze, Italy metallised the S79. There are also several techniques for producing the electrodes. The DDL contacts consist of three layers: DLC (diamond-like carbon)/Pt/Au with 4/10/200 nm thicknesses, respectively. The metallisation for S79, on the other hand, is made up of Cr/Au with a total thickness of  $\sim 400$  nm. The area coverage also differs from sample to sample. Diamonds must not be metallised until the very edge as the proximity of contacts with a high potential difference may lead to bias voltage shorts on sensor edges. However, the areas not covered by the metallisation are less efficient because the fringe fields at the edges are not as strong as in between the electrodes. This effectively reduces the sensitive area of the sensors. In the diamonds used here the effective area is anywhere from 9 mm<sup>2</sup> to 18 mm<sup>2</sup>. The leakage current is below 1 nA, but increases for the irradiated samples. The capacitance is of the order of  $(2.0 \pm 0.3)$  pF for 1scdhq.

#### 3.1.3 Readout devices

Electrical signals in diamond detectors are in the GHz frequency range. To preserve the information in the signals, the readout device with a high bandwidth limit must be used. For instance, a 20 MHz limit is enough for the spectroscopic measurements with the Cx charge amplifier, but is insufficient for the current measurements with the C2 amplifier.

Two devices are used take data shown in this chapter. The first choice is a 2 GHz LeCroy WaveRunner 204MXi-A. This specific model has a sufficiently high bandwidth limit for the fast current preamplifier signals. It offers a reliable solution for analogue signal readout of limited amounts of data. The second device is DRS4 [59], an analogue data acquisition device developed by PSI, Switzerland, capable of recording up to four waveforms at a time at a steady rate of up to 500 Hz. Its 700 MHz bandwidth limitation is sufficient for the signal from the charge and the current amplifier.

### 3.1.4 Setup for the $\beta$ detection efficiency study

A charge collection efficiency study of the diamond sensors has been carried out at CERN in the North Hall test beam facility. There a straight high-energy particle beam of 120 GeV/c  $\pi$  is provided to the users to calibrate their detectors. The beam has a transverse spread of  $\sigma = 10$  mm in both axes. The particle rate is of the order of  $10^4 \pi \text{ cm}^{-2} \text{ s}^{-1}$ . A diamond sensor embedded in a printed circuit board (PCB) carrier has been placed in the beam spot perpendicular to the beam and connected via an SMA connector directly to a charge sensitive amplifier. The amplified signal is read out using a LeCroy oscilloscope and a DRS4 analogue readout system. A computer is used as a controller and data storage for the readout device. A beam telescope is used as a reference detector. It is a device that helps to cross-check the measurements of the devices under test (DUTs) and to carry out spatially resolved studies on the DUTs. It consists of several pixellated sensor planes, such as FE-I4 [60], placed in series, which can track a particle's trajectory with a precision of a few  $\mu\text{m}$ . The sensor planes are positioned in front of the DUT and behind it. Then the beam telescope acts as a trigger system – it triggers the readout of both the telescope data and DUT data when both the planes in front and behind the DUT record a hit by an incident particle. A particle detected by all the planes within the DUT window and the DUT itself counts towards its efficiency whereas a hit missed by the DUT means that the DUT is not 100 % efficient. To discard the hits that miss the DUT completely, a region of interest (ROI) can be chosen in the beam telescope planes. The equation for calculating the sensor efficiency is therefore

$$\epsilon = \frac{N_{\text{DUT}} \wedge N_{\text{telescope}}}{N_{\text{telescope}}} \quad (3.5)$$

for an ROI smaller than the sensitive region of the diamond.

### 3.1.5 Room temperature $\alpha$ -TCT setup

Room-temperature TCT measurements have been carried out in the laboratory. The setup consists of a diamond sensor embedded in a PCB carrier, a current amplifier and an oscilloscope. To measure  $\alpha$  particles, their energy loss during their trajectory has to be minimised. Therefore the diamond is placed inside a vacuum chamber to avoid energy loss in air. The chamber is a steel tube with a diameter of 5 cm. On one side it is connected to a vacuum pump via a steel hose. A feedthrough with an SMA connector is placed on the other side. A CIVIDEC C2 current amplifier is connected directly onto the feedthrough. The amplified output is connected to the oscilloscope via an SMA cable. An  $^{241}\text{Am}$  source with a diameter of 2 cm and a height of 0.5 cm is fixed onto the sensor carrier (figure 3.4a, figure 3.4b). Then the carrier is inserted in the chamber and fixed in place using an air-tight clamp. The pump can then be switched on. It is capable of providing an inside pressure as low as  $10^{-4}$  mbar after approximately one hour of operation.

### 3.1.6 Cryogenic $\alpha$ -TCT setup

This TCT study is a follow-up of an extensive diamond TCT study at cryogenic temperatures [33]. The experiment at cryogenic temperatures has been carried out at the Central Cryogenic Laboratory at CERN. The room-temperature TCT setup has to be modified to allow for measurements at temperatures as low as 4 K. It consists of three parts:

1. a cryostat – a thermally insulated cylinder containing liquid helium,
2. an inlet – an air-tight mechanical tube with valves and feedthroughs at the top that is lowered in the liquid helium and

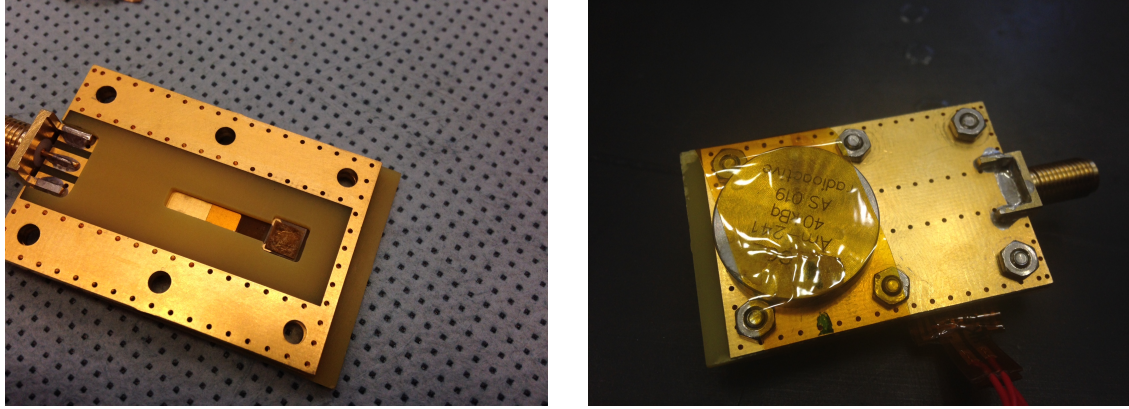


Figure 3.4: Positioning of the  $\alpha$ -source on top of the sensor carrier.

3. a diamond sample embedded in a PCB carrier with a fitted temperature sensor, a heater and cables leading to the feedthroughs.

The setup is described in detail in [33].

When the diamond sample is placed in the PCB carrier and the  $^{241}\text{Am}$   $\alpha$  source is in place, the inlet is sealed and lowered in the empty cryostat. Then the inside volume of the inlet is evacuated down to  $10^{-5}$  mbar while the liquid helium is flowing into the cryostat. To improve the thermal contact between the diamond and the coolant, a small amount of helium gas is added inside the evacuated inlet, setting the vacuum to around  $10^{-3}$  mbar. This value changes with time, because the gas condenses on the walls of the inlet, reducing the number of floating particles. For this reason the helium gas has to be added on a regular basis. Every addition causes a significant undershoot of the sample temperature, which has to be corrected for using a heater placed on the back of the PCB carrier. Also, the added gas deteriorates the vacuum inside the inlet. Furthermore, at approximately 60 K the helium gas has to be evacuated from the inlet to avoid a potential explosion due to the expansion of the gas with temperature.

When the sample is cooled to 4 K, the minimum temperature achievable by means of liquid helium without over-pressurising it, the measurements can begin. A temperature sensor placed on the back of the PCB carrier is used to measure the temperature of the sample. After every measurement, the current through the heater is increased, heating up the sample to the next temperature point. The initial temperature time constant of the order of tenths of seconds at low temperatures increases with temperature. Even more so when helium is evacuated from the inlet at 60 K, removing the thermal bridge between the wall of the inlet and the diamond sample. At the room temperature (RT), the time constant is already of the order of minutes.

## 3.2 Charged particle pulses and spectra

In previous chapter the ionisation profiles for different types of radiation were discussed. A  $\beta$  particle induces a triangular electric pulse whereas a pulse induced by an  $\alpha$  particle is rectangular. However, their amplitude, width and rise/fall time depend heavily on the type of interaction with the diamond, the purity of the diamond and the bandwidth of the amplifier and the oscilloscope. This section shows the signal pulses of  $\alpha$ ,  $\beta$  and  $\gamma$  radiation with their respective energy distributions for the case of a diamond detector.

Figure 3.5 shows a set of pulses and an averaged waveform for 5.5 MeV  $\alpha$ , 2.3 MeV  $\beta$  and 1.3 MeV  $\gamma$  radiation using an  $^{241}\text{Am}$ , a  $^{90}\text{Sr}$  and a  $^{60}\text{Co}$  source, respectively. The particles are measured with the non-irradiated sCVD diamond S37.  $\alpha$  particles always produce the same signal pulse with a noise RMS of 2.7 mV. The averaging suppresses the noise while retaining most the information. It does, however, smear the rising and falling edge, increasing the rising and falling time. The  $t_r$  is now of the order of 0.5 ns. The pulse count for  $\beta$  and  $\gamma$  is low, so the pulses with a high amplitude are not recorded. A trigger would need to be set very high to “catch” them with the oscilloscope. Both  $\beta$  and  $\gamma$  pulses look similar - triangular and with a wide range of amplitudes.

Histograms on the right hand side of figure 3.5 show distributions for of deposited charge as measured with a CIVIDEC Cx amplifier. The distribution of  $\alpha$  particles is a Gaussian function. The  $\beta$  distribution follows a Landau function. This is due to scattering of  $\beta$  in the sensor. Some  $\beta$  maintain a straight trajectory while traversing the sensor. Those create a Gaussian-like distribution. Others scatter in the lattice, extending the effective length of the path and therefore increasing the number of excited e-h pairs. In some cases the  $\beta$  produce a shower of secondary particles, which in turn create more e-h pairs. Contributions from all types of interactions form a Landau distribution.

$\gamma$  distribution on the other hand is expected to be a convolution of signals created by photoelectric and Compton interactions. The expected distribution is an exponential. The acquired data are taken with a self-trigger set to 20 mV to minimise noise contribution.

### 3.2. CHARGED PARTICLE PULSES AND SPECTRA

---

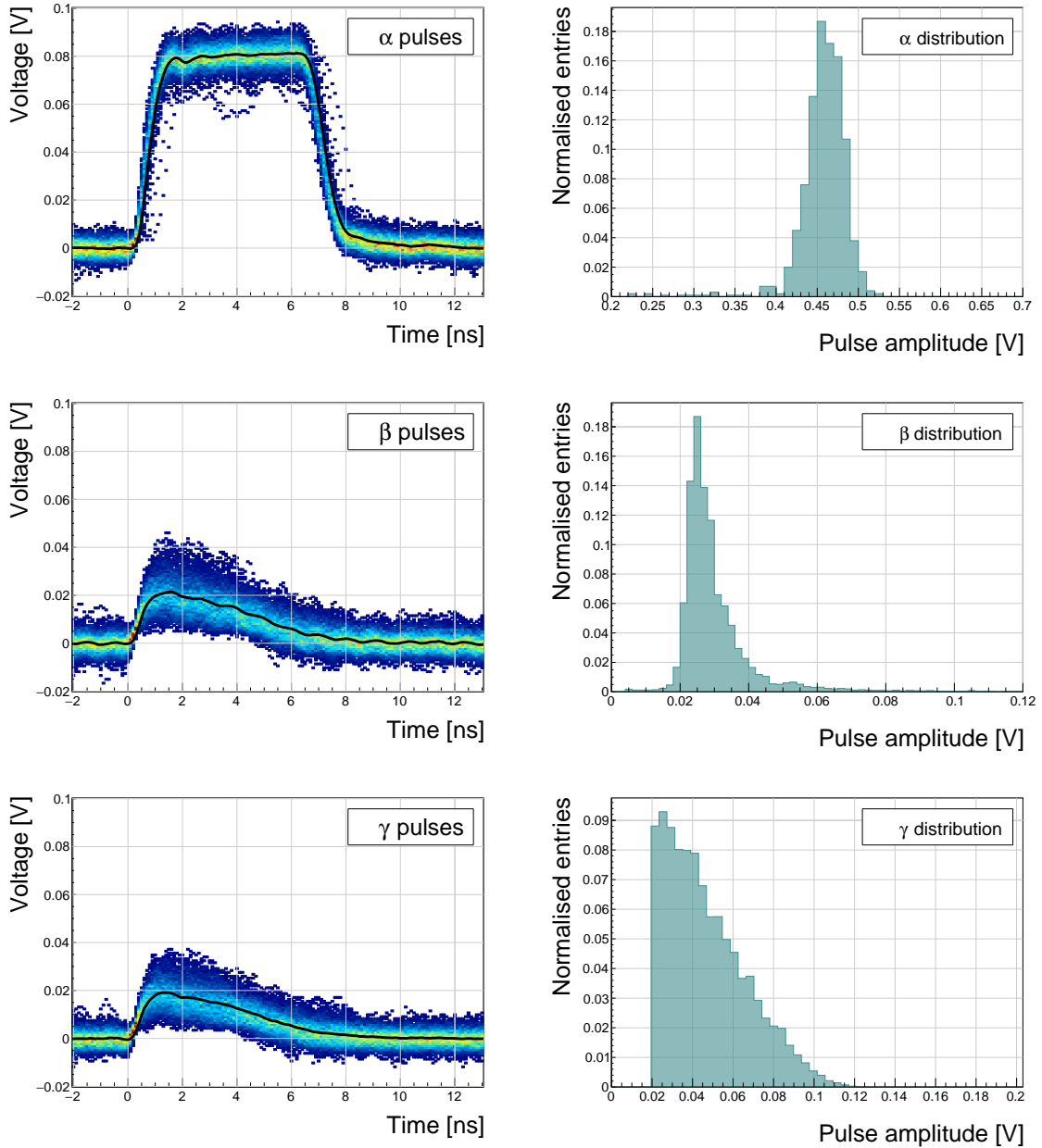


Figure 3.5: Superimposed and averaged pulses (left figures, current amplifier) and distributions of deposited energy (right figures, charge amplifier) for three types of radiation. Note the scale on the x axis of the distributions.

### 3.3 Radiation limitations

This section quantifies the decrease in charge collection efficiency as well as the effects on long-term measurement stability in irradiated sCVD diamonds.

#### 3.3.1 Irradiation study

This subsection contains a study of the effects of 300 MeV pion irradiation on the charge collection efficiency of sCVD diamond detectors. To carry out this study, two diamond samples were irradiated with 300 MeV pions ( $\pi$ , kinetic energy 191.31 MeV). The irradiation campaign took place at the Paul Scherrer Institute (PSI) [61] where the machine provides a flux of  $1.5 \times 10^{14} \pi \text{ cm}^{-2}$  per day. The quoted uncertainty on the measurement of the delivered dose is  $\pm 20\%$ . In addition, a deviation in beam energy can have a significant effect on the damage in the sensor, considering the pion damage curve in figure 2.10 at a  $\pi_{300 \text{ MeV}}$  point (191 MeV kinetic energy), which sits on a steep section of the DPA curve. The target fluences for S79 and S52 were  $(1 \pm 0.2) \times 10^{14} \pi \text{ cm}^{-2}$  and  $(3.6 \pm 0.7) \times 10^{14} \pi \text{ cm}^{-2}$ .

A test beam campaign was carried out to observe the charge collection efficiency at different bias voltage settings. The efficiency values acquired are used to determine the effective drop in efficiency as a function of fluence. This is to test if the collected charge  $Q$  is inversely proportional to the fluence  $\Phi$ , as per equation 2.21. A procedure defined by a collaboration researching diamond behaviour RD42 has been applied to the measured values to extract the damage factor described in section 2.5.

Subsection 3.3.2 contains measurements and results of a long-term stability study using  $\alpha$  and  $\beta$  particles. In particular, charge collection efficiency with  $\beta$  and  $\alpha$  radiation as a function of time is measured. To investigate the effect of decreased charge collection of irradiated diamond with time, TCT (transient current technique) is employed. Finally, a procedure that improves the pulse shapes and the charge collection efficiency is proposed.

##### 3.3.1.1 300 MeV $\pi$ radiation damage factor

Three diamonds – non-irradiated S37 and irradiated S52 and S79 – were tested in a  $\pi_{120 \text{ GeV}/c}$  test beam in the SPS North Experimental Area at CERN [62] before and after irradiation. The goal was to estimate the charge collection efficiency and charge collection distance as a function of fluence. The samples were primed prior to data taking using a  ${}^{90}\text{Sr}$  radioactive source. The data were then taken at a range of bias voltages ranging from 30 V to 900 V, yielding between  $0.06 \text{ V}/\mu\text{m}$  and  $1.8 \text{ V}/\mu\text{m}$  electrical field in the bulk. Every data point contained approximately  $5 \times 10^4$  measured particles. The charge deposited by the particles was measured using a CIVIDEC Cx charge preamplifier.

The integrated amplitude spectrum is a Landau distribution. Its most probable value (MPV) is used to calculate the most probable collected charge  $Q_i$ :

$$Q_i [\text{e}^-] = \frac{1}{1.6 \times 10^{-19}} Q_i [\text{C}] = 6'241 \cdot Q_i [\text{fC}] = 6'241 \cdot \frac{\text{MPV} [\text{mV}]}{A [\frac{\text{mV}}{\text{fC}}]}, \quad (3.6)$$

where  $A = 9.3 \text{ mV/fC}$  is the preamplifier gain factor and  $1 \text{ e}^- = 1.6 \times 10^{-19} \text{ C}$ .

The CCD for the three measured samples at a bias voltages ranging from  $0.2\text{--}1.6 \text{ V } \mu\text{m}^{-1}$  calculated using equation 2.19 is shown in figure 3.6. S37 exhibits a full collection distance already at  $0.4 \text{ V } \mu\text{m}^{-1}$  whereas the irradiated samples have a more gentle increase of CCD with increasing bias voltage. It is evident that at  $1 \text{ V } \mu\text{m}^{-1}$  the maximum CCD has not been reached in the case

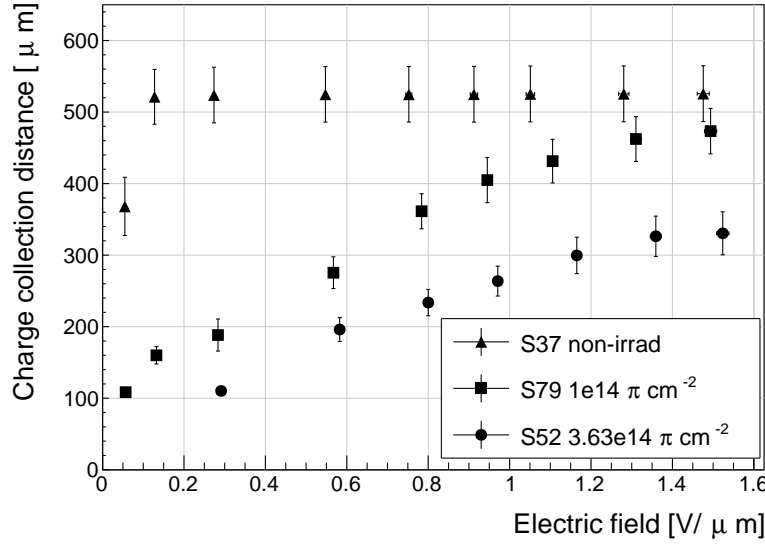


Figure 3.6: The figure shows the CCD for S37, S79 and S52 at a range of bias voltage settings.

of S79 and S52. Nevertheless, to compare the measured data point with those provided by RD42, the CCD at  $1 \text{ V}\mu\text{m}^{-1}$  has to be taken.

Data points with the maximum CCD obtained in the test beam measurements are plotted as a function of fluence in figure 3.7. Equation 2.21 is fitted to the data points and a damage factor  $k_\lambda = (4.4 \pm 1.2) \times 10^{-18} \mu\text{m}^{-1} \text{cm}^2$  is obtained. The value is for a factor of two higher than the damage factor obtained by RD42. This could be due to an insufficient priming time ahead of the measurement. The samples were only exposed to the radioactive source for 30 min and might not have achieved the maximum charge collection (effect of priming shown in figure 3.8). In addition, the diamond samples have not been polished and re-metallised after irradiation, as is the case for the RD42. A study of effects of re-metallisation on the charge collection has been done in [63] and supports this theory. Furthermore, with only two samples measured, the statistical uncertainty is high. For a better fit another measurement point at a higher fluence would need to be added. Nevertheless, it can be concluded that the 300 MeV pions damage the diamond bulk significantly more than the 24 GeV protons, as shown in chapter 2.

Another diamond irradiation study has been carried out using the Beam Conditions Monitor (BCM) at the CMS experiment [42]. The BCM's diamond sensors have been exposed to radiation from beam collisions with a wide spectrum of energies and particle types. The damage factors measured are an average of  $3.5 \times 10^{-17} \mu\text{m}^{-1} \text{cm}^2$  and  $9.2 \times 10^{-16} \mu\text{m}^{-1} \text{cm}^2$  for pCVD and sCVD diamonds, which is for a factor of 58 and 1500 higher than the RD42. These low charge collection efficiencies, however, are purported to be convoluted with other effects, such as polarisation, which will be discussed later in the chapter.

### 3.3.2 Long-term measurement stability

An important requirement for particle detectors is a stable performance over long periods of time. For instance, charge collection for a defined radiation type and quantity must not change over time or has to change in a predicted way. The stability of diamond detectors depends on many factors, e.g.

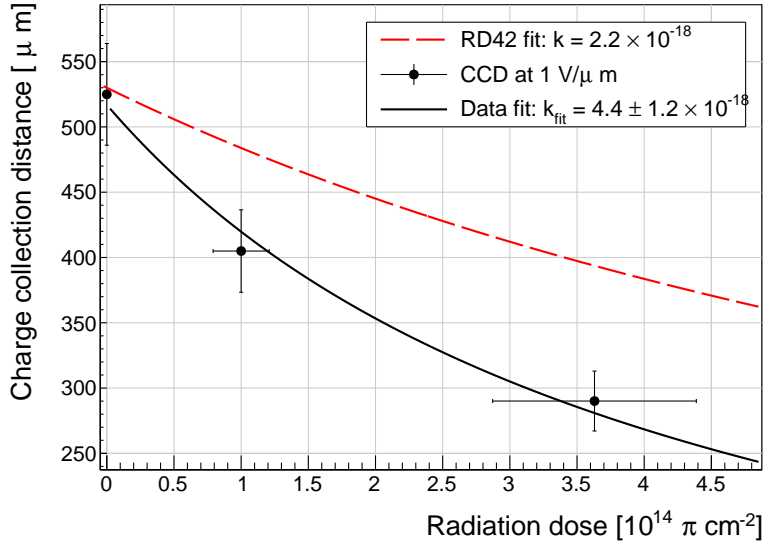


Figure 3.7: The charge collection distance at 1 V/ $\mu\text{m}$  bias voltage for the three diamond samples is plotted as a function of fluence. It is compared to the RD42 data for pion irradiation. The data points are about 15–25 % lower than expected from the RD42 data [48].

material purity, polishing process, electrode material, irradiation damage etc. The aim is to study the behaviour of diamond under controlled conditions, with the goal to understand its limitations. One of these limitations is the fluence as it can affect the long-term stability of the sensor during operation.

The three diamond samples (S37, S79 and S52) have been exposed to two different types of ionising radiation for a longer period to see if their behaviour changes over time. Two parameters have been observed in particular:

1. Charge collection of  $\beta$  particles and
2. Charge collection and ionisation profile of  $\alpha$  particles.

### 3.3.2.1 $\beta$ long-term stability

The diamond samples have undergone a long-term stability test at room temperature using  $\beta$  radiation. This has been done using a  ${}^{90}\text{Sr}$  source emitting  $\sim 2.28$  MeV electrons via  ${}^{90}\text{Y}$  decay at a rate of approximately  $10^4 \text{ e}^- \text{ cm}^{-2} \text{ s}^{-1}$  as measured using a real-time particle counting application described in chapter 5. To simulate the initial conditions in HEP experiments, the sensors must not be primed before starting the measurements. The measurement setup consists of a diamond sample (S37, S52 or S79) with the CIVIDEC Cx spectroscopic amplifier, a silicon diode with a CIVIDEC C6 amplifier for triggering and a  ${}^{90}\text{Sr}$  source on top. A particle emitted by the source traverses the sensor bulk and hits the silicon diode, triggering the analogue signal readout. The source is left on the top for the course of the experiment. The measurements, however, are taken at discrete times. For every data point, approximately  $10^4$  triggers have to be recorded. The offline analysis of the recorded signal pulse amplitudes yields a Landau distribution for every data point. The current charge collection relative to the initial charge collection for every sample is plotted as a function of the received  $\beta$  dose in figure 3.8. It shows that, for the irradiated samples, the charge collection efficiency improves when the diamond sensor is primed with a  $\beta$  source. The effect is negligible for

### 3.3. RADIATION LIMITATIONS

---

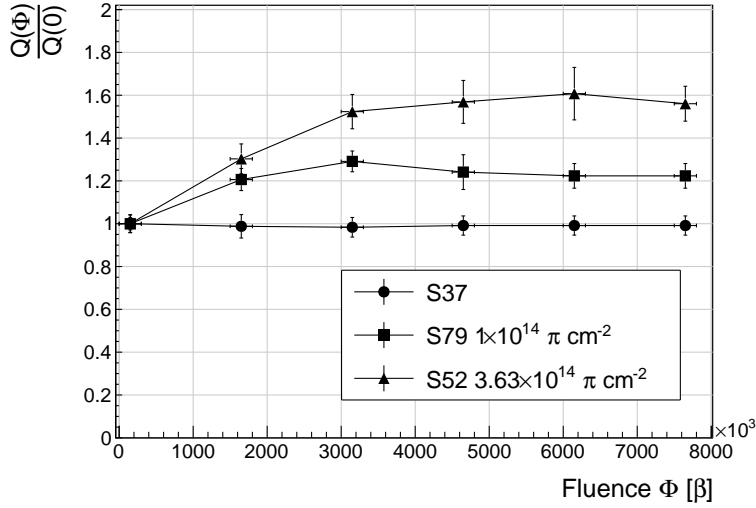


Figure 3.8: Relative increase of charge collection over time due to priming with the  $^{90}\text{Sr}$  radioactive source. The charge collection for the non-irradiated S37 stays constant. The bias voltage for this measurement is 1 V/ $\mu\text{m}$ .

the non-irradiated high-quality S37. Both relative increases are significant – 22 % for S79 and 55 % for S52. At a fluence of approximately  $4 \times 10^6$  particles the charge collection is stabilised. At that point S79 achieves close to a full efficiency (in absolute values – not shown) whereas S52 reaches approximately 50 %.

To sum up, diamond provides a stable measurement of the  $\beta$  radiation detection after reaching a stable state. Even if damaged by radiation, it reaches a stable charge collection at a fluence of  $\sim 4 \times 10^6$  MIPs. Its efficiency decreases with a high fluence. However, the decrease can be accounted for if the damage factor and the rate and energy of the particles are known.  $\gamma$  radiation has a similar impact on the diamond as the  $\beta$ . The incident photons, if they interact with the diamond, prime the bulk, increasing the charge collection efficiency. The difference, however, is that the interaction probability (cross-section) is lower for gammas [64, 65].

#### 3.3.2.2 $\alpha$ long-term stability

This part discusses the stability of irradiated diamond sensors during  $\alpha$  measurements. An  $^{241}\text{Am}$  source has been used, emitting  $\alpha$  particles with a mean energy of 5.5 MeV with an average rate of  $7 \text{ s}^{-1}$ .

To test the stability of the diamond during  $\alpha$  measurements, the samples have been biased at +500 V and exposed to up to  $8 \times 10^3$   $\alpha$  hits while measuring their charge collection efficiency using the CIVIDEC Cx spectroscopic amplifier. The charge collected at every measurement point  $Q(\Phi)$  is compared to collected charge of the first measurement  $Q(0)$ . The resulting ratio  $\frac{Q(\Phi)}{Q(0)}$  for all samples is shown in figure 3.9. Each measurement point is an average of 30 consecutive  $\alpha$  hits. The observations are the following:

- $Q(\Phi)$  for the non-irradiated S37 is stable as compared to  $Q(0)$  over the course of the measurement.
- The initial efficiency of the irradiated S52 and S79 starts decreasing already at a low  $\alpha$  count.

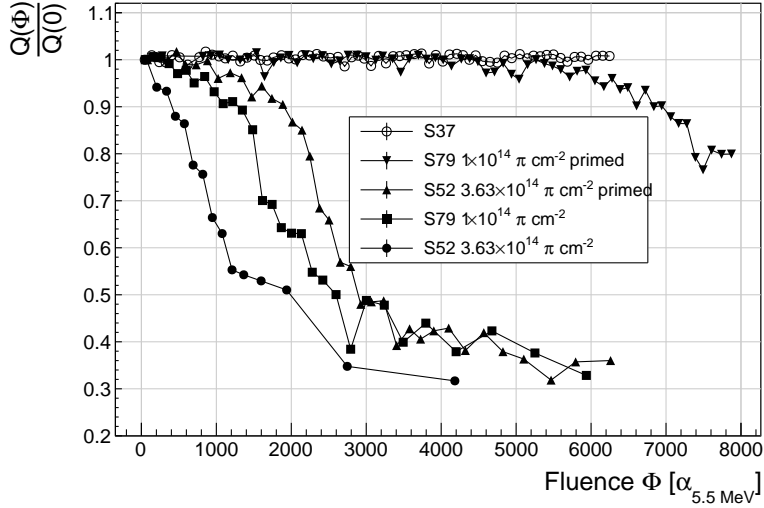


Figure 3.9: A relative drop in charge collection efficiency as a function of the received  $\alpha$  dose for non-irradiated and irradiated diamond samples.

- The charge collection efficiency of the unprimed irradiated samples drops much faster than after priming.
- The particle count rate decreases with decreased efficiency, which is clearly seen in the unprimed S52 data where the data points at a low efficiency are much further apart.

The absolute values are not shown here because only the relative drop is of interest in the scope of the long-term stability tests.

To investigate this sudden drop in efficiency, the current pulse shapes using a CIVIDEC C2 current amplifier have to be observed, as shown in figure 3.10. The shape of the pulse holds more information about the charge carrier properties in the sensor than solely the value of the integrated charge. This time only the primed S79 sample has been tested. Both the hole and the electron collection are observed to determine whether they behave differently or not.

The first observation in the raw acquired data in figures 3.10 is that the initially stable pulses start deteriorating; several different shapes start appearing gradually, some still very similar to those from the beginning while the others with almost zero amplitude.

A more dedicated analysis of the first observation has been carried out as follows: at the beginning of the test when the diamond is still operating stably, 60 pulses are recorded. An average pulse is calculated. This is a *reference pulse* for the subsequent measurement points. Then an RMS of the individual pulses  $\sigma_n$  with respect to the reference pulse is calculated and the resulting RMS values are summed together into  $\sigma(0)$  and divided by the number of summed values:

$$\sigma(0) = \frac{\sum_{n=1}^{60} \sigma_n}{60}. \quad (3.7)$$

All the subsequent data points also consist of a set of 60 pulses. At every data point the summation of the RMS values of the individual pulses with respect to the reference pulse  $\sigma(0)$  is calculated according to equation 3.7. The ratio between the reference  $\sigma(0)$  and discrete values  $\sigma$  gives a measure of the change of the pulse shape with respect to the reference pulse at the start of the measurement. Therefore the initial value is 1 and it decreases if the RMS values of subsequent data

### 3.3. RADIATION LIMITATIONS

---

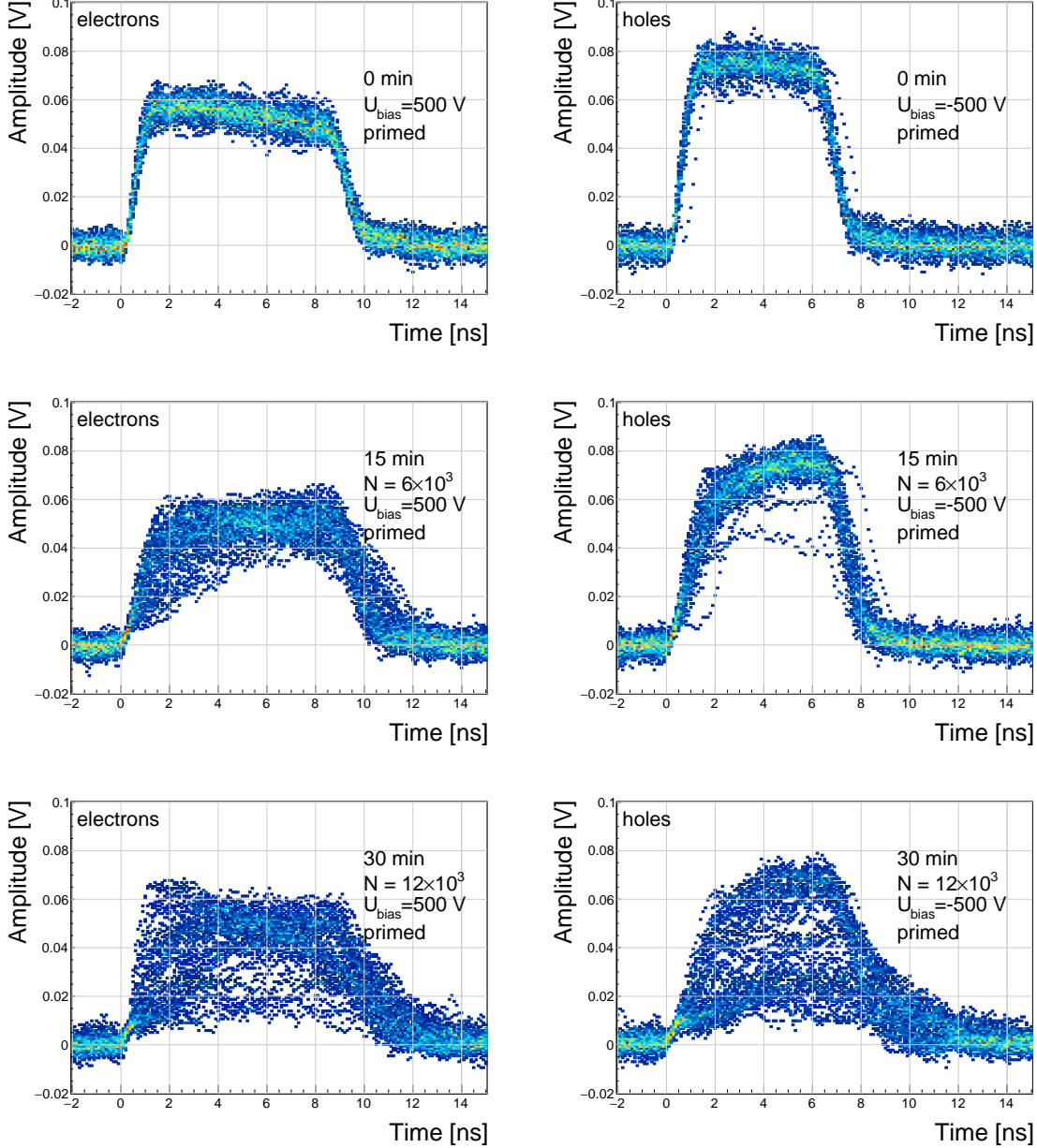


Figure 3.10: The signal of the irradiated and primed S79 deteriorates with time for both polarities. Every plot contains 60 superimposed pulses.

points are higher. Figure 3.11 shows the ratio  $\frac{\sigma(0)}{\sigma(\Phi)}$ . From the data obtained it can be concluded that the initial pulse shape quickly starts deteriorating. In fact, the deterioration of the shape follows an approximate exponential decay function before it settles at the lowest value. The resulting decay constants for electrons and holes are  $\tau_e = (4400 \pm 150) \alpha^{-1}$  and  $\tau_h = (3300 \pm 140) \alpha^{-1}$ . The electrons retain the initial shape for longer. The deteriorated shapes also seem to be for a factor of 2 better than those of the holes.

**Discussion** One hypothesis is that this behaviour is caused by space-charge build-up. Charge carriers get stopped in the charge traps in the bulk for a long time, building up regions of space-

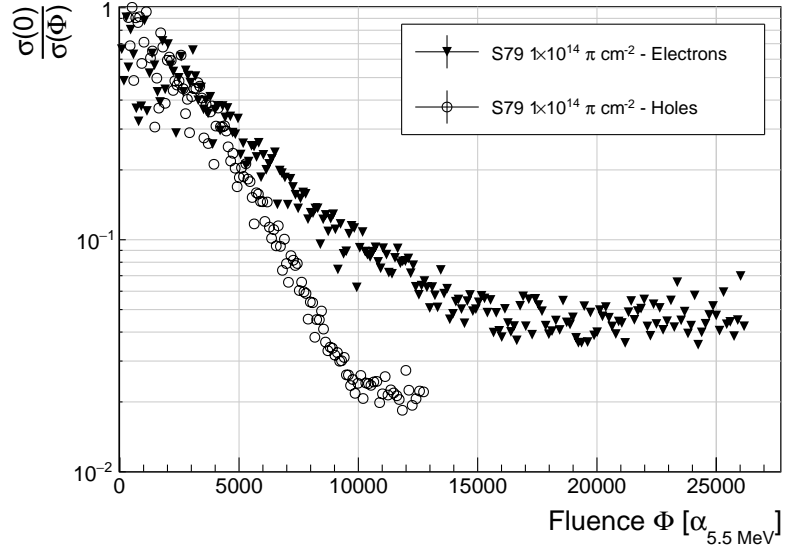


Figure 3.11: Deterioration of the pulse shapes with time.

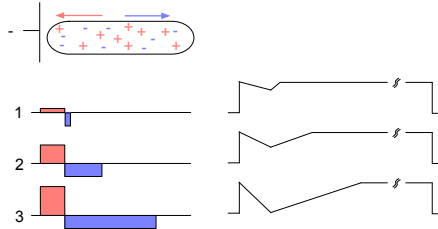


Figure 3.12: Space-charge build-up at the electrode. The figure shows the  $\sim 15 \mu\text{m}$  long charge cloud that is created by an  $\alpha$  particle. The positive charge carriers get trapped in charge traps in the damaged surface at the electrode. The positive space charge attracts the negative carriers, which form a negative space charge region. Both regions gradually grow, eventually creating a barrier in the electric field distribution, as shown on the right side of the diagram.

charge. The built up space-charge creates an internal electric field – polarisation. This field in turn affects the speed of the drifting charge carriers. Since the movement of the carriers is inducing the electric current, the field gradient can be observed in the current signal. The fact that the signal shapes vary significantly might be due to a very non-uniform electric field, suggesting a complex polarisation in the sensor.

Figure 3.12 shows how the space-charge might be built up at the entry point of the  $\alpha$  particle. The assumption is that the first few  $\mu\text{m}$  of diamond surface are significantly more damaged than the rest of the material. Therefore the probability that charge carriers would get trapped at the edge of the sensor is higher. If the sensor is biased as shown in the figure, the positive charge cloud drifts towards the adjacent electrode while the negative cloud drifts through the sensor to the opposite one. Therefore most of the trapped carriers at the adjacent electrode are positive, forming a strong positive space-charge barrier in the first few  $\mu\text{m}$  of the sensor (1). The negative carriers created by subsequent  $\alpha$  particles are attracted by the positive space charge and get trapped close

### 3.3. RADIATION LIMITATIONS

---

to the positive space-charge (2). This negative space-charge region is gradually stretched inwards (3). Together the two regions form a barrier which counteracts the externally applied electrical field. Such a distortion of the field prevents the charge carriers from drifting freely within the space-charge region. Only those negative carriers that diffuse through this barrier can start drifting towards the positive electrode. Others either recombine or are trapped, contributing to the build-up of the barrier.

This hypothesis explains the gradual loss of collected charge in figure 3.9 and the pulses with a slow rising edge in figures 3.10. However, this simple picture cannot explain the electron pulses with a negative slope. Further reading regarding the space-charge build-up is available in [66, 67, 68], however, no direct explanation of the observed phenomenon has been given.

**Restoring the pulse shapes** Finally, an effort has been made to find a way for the pulse shapes to return to their initial state. Five methods are listed:

1. No source, with bias voltage,
2. No source, without bias voltage,
3. Priming with  $\gamma$  at a rate of  $400 \text{ s}^{-1}\text{cm}^{-1}$  without bias voltage,
4. Priming with  $\beta$  at a rate of  $1'000 \text{ s}^{-1}\text{cm}^{-1}$  with bias voltage and
5. Priming with  $\beta$  at a rate of  $1'000 \text{ s}^{-1}\text{cm}^{-1}$  without bias voltage.

Before starting each method, the diamond sample S79 is first primed using a  $^{90}\text{Sr}$  source for approximately one hour. Then the bias voltage is switched on and an  $^{241}\text{Am}$  source is put on top. The pulses produced by the incident  $\alpha$  particles have a proper rectangular pulse at the beginning, but then start changing – first gradually and later increasingly more in an erratic way, as described in the text above. After approximately 30 minutes, one of the methods is tested. When a “healing” procedure is started, a set of 60 pulses is taken at irregular points of time to observe the change in the pulse shape and to assess the quality of the “healing” procedure. Then the bias voltage is switched off and the sample is primed again to reset its state before starting the next measurement.

The results depicted in figure 3.13 show that the methods (3) and (5) improve the shape, method (2) helps slowly, (1) does not show any change with time and (4) at first improves, but then significantly degrades the shape. The effect observed in method (4) has already been described in [69]. The “healing” process therefore depends on the rate of radiation, the bias voltage and the time of exposure. The ionising radiation creates free charges, which quickly recombine close to the place of generation. It is likely that they also release the charges trapped during the measurement, reducing the overall effect of the space-charge. The traps get filled with both flavours of carriers, thus they are neutralised. The pulse shape gradually returns to its initial state.

Procedure	Source	Type of radiation	Bias voltage	Effectiveness
1	/	/	ON	no
2	/	/	/	slow
3	$^{60}\text{Co}$	$\gamma$	/	YES
4	$^{90}\text{Sr}$	$\beta$	ON	no
5	$^{90}\text{Sr}$	$\beta$	/	YES

Table 3.2: Effectiveness of healing procedures.

**Summary** The shape of the pulses caused by  $\alpha$  radiation changes with time for irradiated samples. The shape of the pulses gets distorted. The charge collection decreases and its spread increases. The signal shapes are probably affected by a non-uniform electric field, which is caused by polarisation

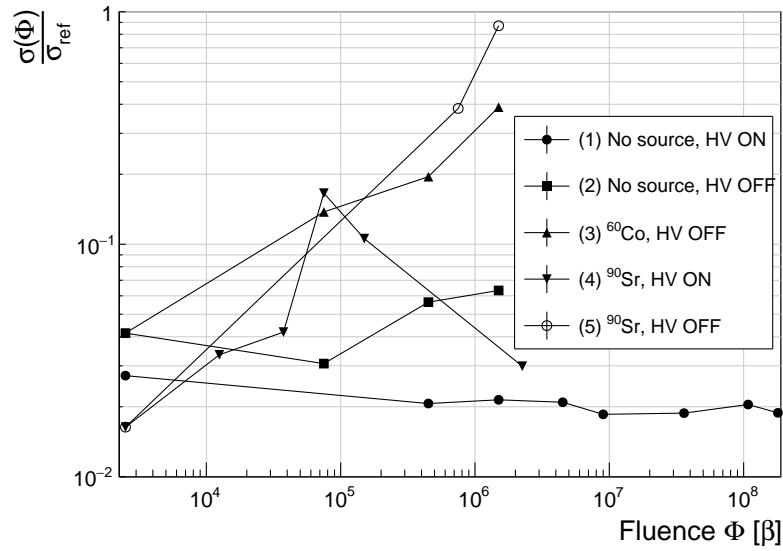


Figure 3.13: Comparison of the five procedures for the “healing” process for an irradiated diamond that had been exposed to  $\alpha$  radiation with a rate of  $7 \text{ s}^{-1}$ , with the bias voltage switched on, for at least 30 minutes.

in the sensor. The signal degradation happens even faster for non-primed diamonds. To “heal” the diamond – to bring the pulse shapes back to their initial shape – the sample must be primed using a  $\beta$  or a  $\gamma$  source for several minutes without bias voltage. Switching to the inverse polarity for a few seconds helps a bit, but in a long run distorts the signal, preventing it from returning to the initial shape.

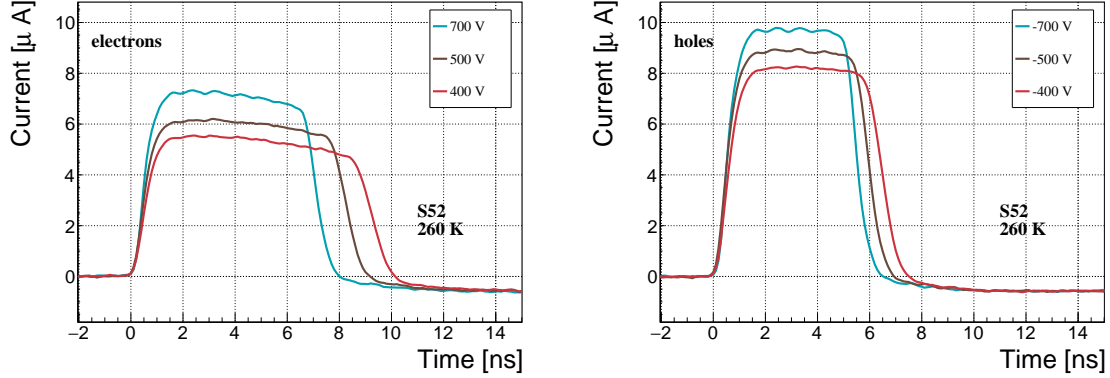


Figure 3.14: Varied bias voltage at a fixed temperature of 260 K.

## 3.4 Temperature limitations

A test has been carried out to evaluate the effect of temperature on the output signal of the diamond sensors. A cryostat filled with liquid helium is used to cool down the sensor during the measurement process. The current signal response to  $\alpha$ -particles is measured at 18 temperature points between 4 K and 295 K. At every temperature point a set of 300 pulses is recorded at a range of positive and negative bias voltages and averaged in the analysis.

### 3.4.1 Temperature-variant $\alpha$ -TCT before irradiation

Three sCVD diamond samples have been tested at a range of temperatures using the  $\alpha$ -TCT technique to verify the consistency of the results with those obtained by H. Jansen in [33].

The resulting averaged pulses of the non-irradiated sample S52 at the 260 K temperature point and a bias voltage of  $\pm 700$  V,  $\pm 500$  V and  $\pm 400$  V are shown in figure 3.14. The pulses induced by positive charge carriers are shorter than those induced by electrons, which means that holes travel faster in diamond. The area of the pulse, however, is the same for both polarities, which corresponds to the fact that the same amount of charge carriers is drifting in both cases.

Figure 3.15 shows pulses at a bias voltage set to  $\pm 500$  V across the range of temperatures between 4 K and 295 K. Several conclusions can be drawn by observing their shape. First, the pulse shapes change with decreasing temperature. The pulse time gets shorter and higher, hinting at the faster carrier drift velocity  $v_{\text{drift}}$ . Second, between 150 K and 75 K there is a significant change in shape – the time constant of the rising edge increases significantly and the pulse area decreases [33]. From 75 K down to 4 K there is no significant change. Last, the top of the pulse at the S52 is not flat, which means that a portion of the drifting charge is lost along the way. This is due to the built up space-charge, likely by means of crystal defects or impurities introduced during production.

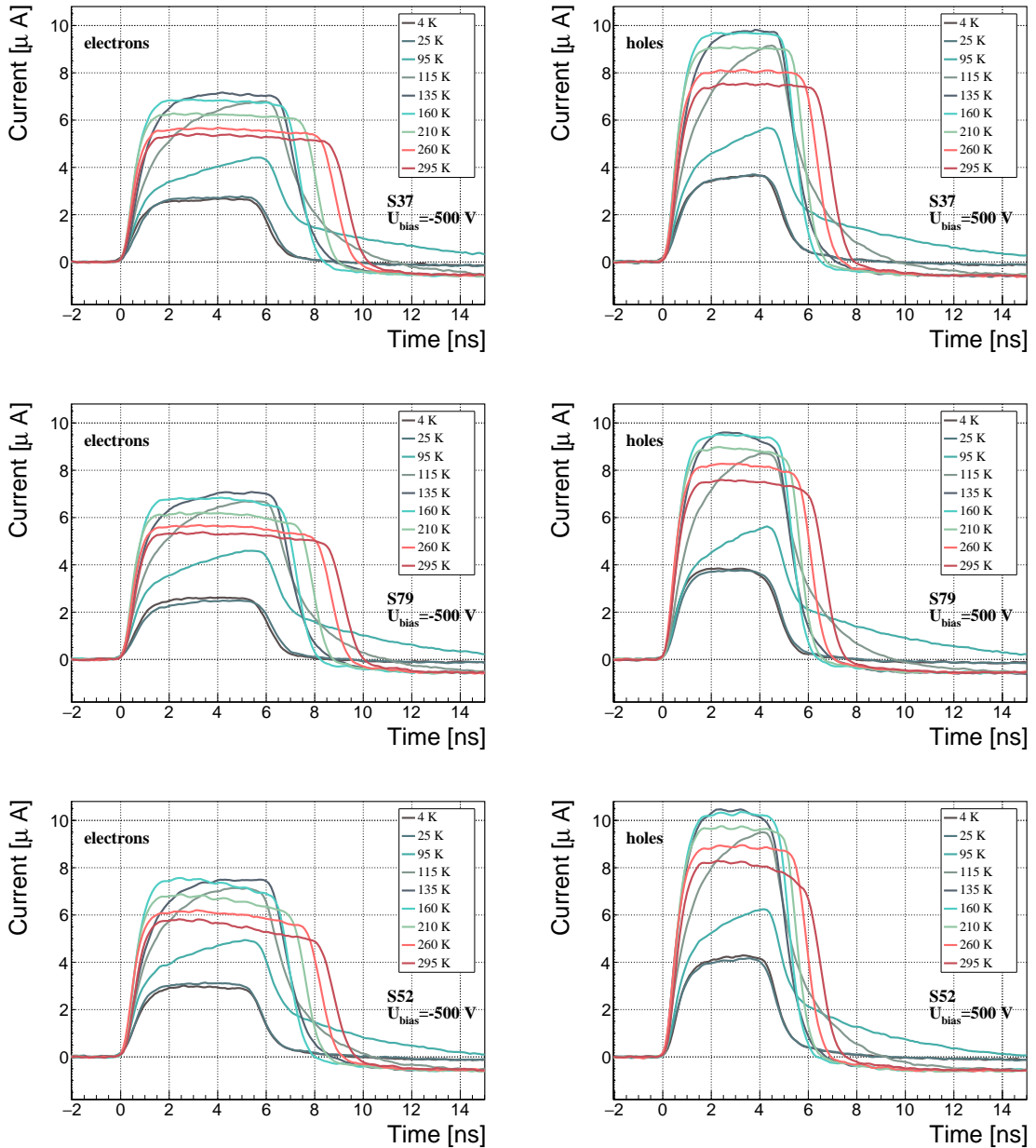


Figure 3.15: Three non-irradiated diamond samples: S37, S79 and S52. Several data points between 4 K and 295 K at a bias voltage of  $\pm 500$  V (electrons and holes). The tilted top of the pulse on the bottom left figure is due to built-up space charge.

### 3.4. TEMPERATURE LIMITATIONS

---

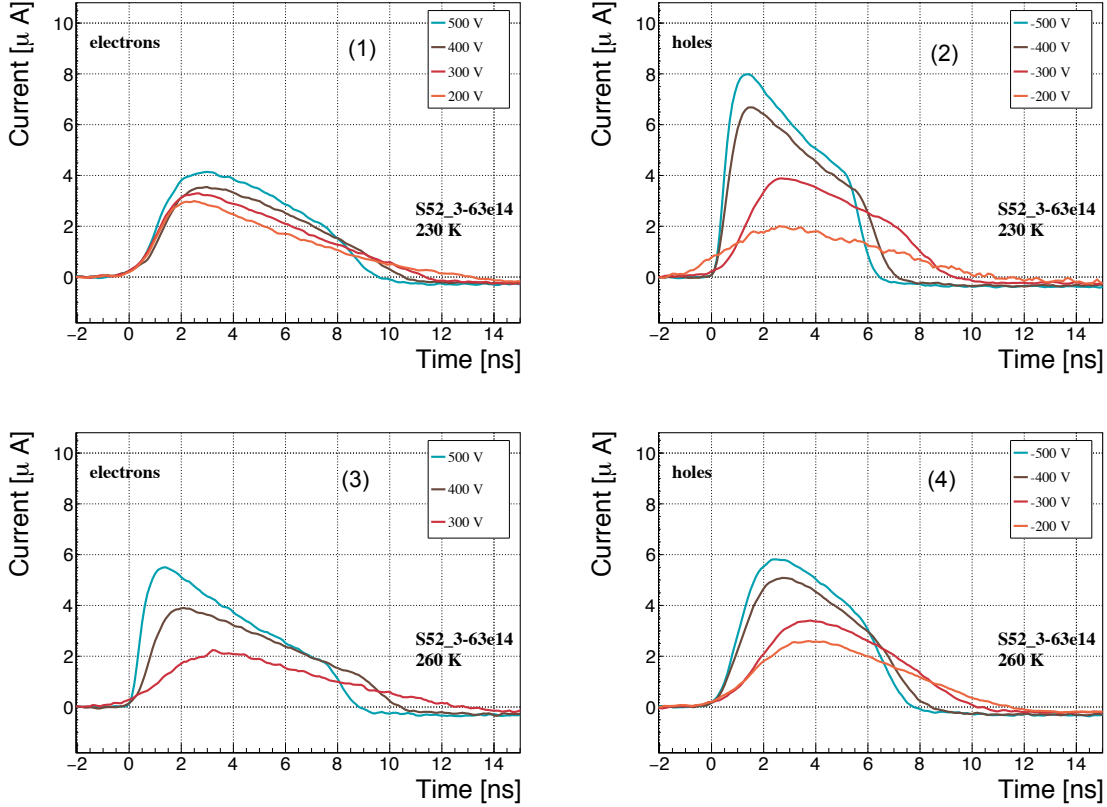


Figure 3.16: Varied bias voltage at a fixed temperature for an irradiated sample.

#### 3.4.2 Temperature-variant $\alpha$ -TCT after irradiation

The irradiated S79 and S52 have been re-tested in the cryostat after irradiation. The aim is to observe how their pulse shapes change with decreasing temperature, in particular the decaying top of the pulses, as shown in figure 3.16. The decay time gives information on trapping of charge carriers while travelling through the diamond bulk. A variation of the decay time constant as a function of temperature might help to reveal the type and energy level of the charge traps. To observe these effects, a number of requirements have to be met. First, the diamond samples are intentionally not primed prior to the experiment because priming would improve the pulse shapes and change the decay time constant of the signal. Second, keeping in mind that the pulse shape of irradiated diamonds changes with time, the duration of the measurement of an individual data point has to be short – of the order of 30 seconds. Last, the sequence of the bias voltage settings is important, the reason for which is explained below. Temporal pulse changes are unavoidable. For instance, one measurement point takes approximately one minute. After the measurement, the bias voltage polarity is swapped for a few seconds to bring the diamond back into its initial state. A few seconds with respect to a minute is not enough, but due to time constraints this cannot be avoided. Therefore when the bias voltage is set to the next value, there is still some residual effect of the previous measurement. Similar to the effects of polarisation, this effect is also decreasing the pulse height. This can be observed in figure 3.16, which shows the resulting pulses of S52 for bias voltages of  $\pm 200$  V,  $\pm 300$  V,  $\pm 400$  V and  $\pm 500$  V at 230 K and 260 K. In this case the measurement sequence is: 230K (200 V, 300 V, 400 V, 500 V, -500 V, -400 V, -300 V), 260 K (-200 V, -300 V, -400 V,

-500 V, 500 V, 400 V, 300 V). The changes in pulse shapes for holes at 230 K and 260 K cannot be attributed to the temperature change. Instead, the explanation lies in diamond polarisation. This means that, when exposed to an electric field with  $\alpha$  measurements ongoing, an internal electric field of inverse polarity builds up in the diamond, which effectively reduces the overall electric field. This internal field does not dissipate when the external bias voltage is switched off. The diamond becomes polarised. When switching the polarity of the external bias voltage, the internal and external electric field point in the same direction at the beginning, increasing the overall electric field and with it the pulse height. In figure 3.16 this happens when switching from 500 V (figure 3.16a) to -500 V (figure 3.16b) at 230 K. The built up polarisation contributes to the pulse having a sharp rising edge and a high amplitude. This effect decays during the next two voltage points. There are a handful of ways to avoid this polarisation effect in the data:

1. After every data point invert the bias voltage and leave it to return to a neutral state for the same amount of time,
2. Make a hysteresis of data points, going from minimum negative to maximum positive bias several times,
3. Reduce the measurement time at every bias voltage setting.

Options (1) and (2) are very time consuming and would increase the overall experiment time significantly. The third option would worsen the resulting averaged pulses. Finally an alternative option has been chosen: alternating the starting bias voltage polarity and the sequence of bias voltages at every temperature point. With this option, a minimum systematic error in analysing the pulse shapes is attained.

Figure 3.17 shows the irradiated S52 and S79 as well as the non-irradiated S37 for comparison, all at a bias voltage of  $\pm 500$  V and at several temperature points between 4 K and 295 K. It is evident that radiation damage affects the shape of the pulses by means of charge trapping across all temperatures.

### 3.4. TEMPERATURE LIMITATIONS

---

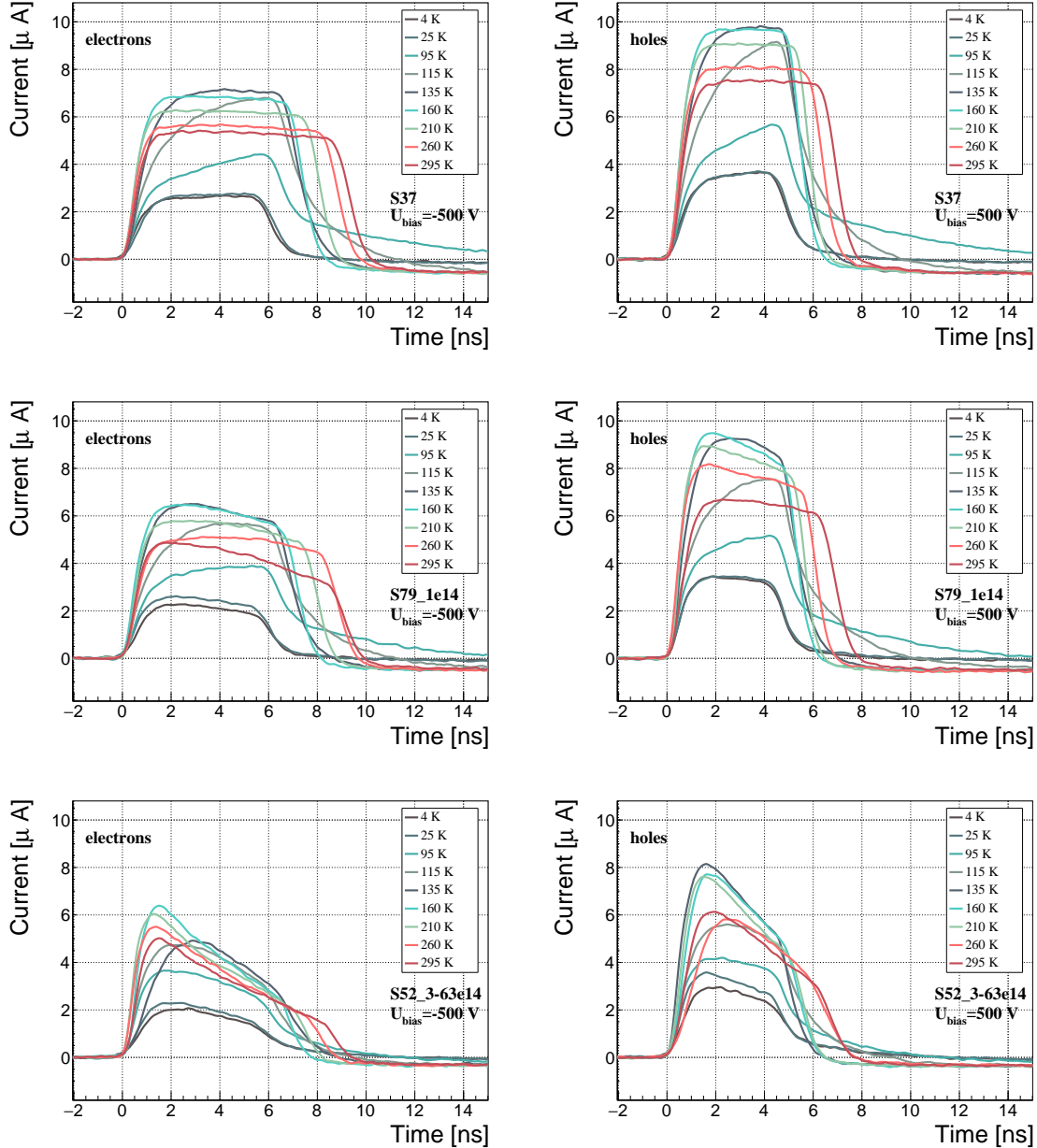


Figure 3.17: Non-irradiated S37 and irradiated S79 and S52. Several data points between 4 K and 295 K at a bias voltage of ±500 V.

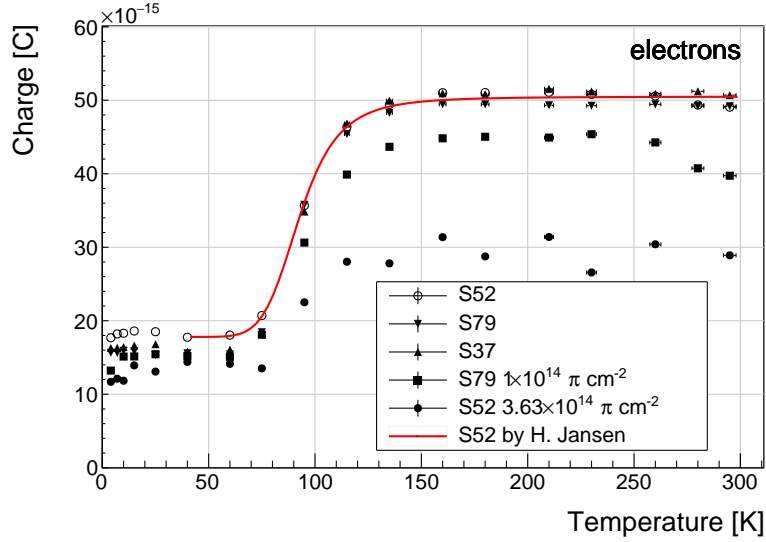


Figure 3.18: Collected charge for electrons as a function of temperature.

#### 3.4.2.1 Collected charge as a function of temperature

The collected charge as a function of temperature for electrons and holes is plotted in figures 3.18 and 3.19, respectively. The red line shows the results from [33]. The new contribution are the data points for the irradiated samples. The focus is on the temperature range between 4–75 K and 150–295 K whereby the creation/decay of excitons is not dominating the pulse shapes. The values for all samples are fairly stable in the range between 4 K and 75 K and between 150 K and 295 K. However, in the values for the irradiated S52 some excursions can be observed. This is due to the sequence of the measurement steps, which results in a hysteresis effect explained in the preceding text.

The collected charge drops significantly from 150 K down to 75 K. In the non-irradiated samples the values in the lower temperature range are approximately 30 % of those in the high range. For the irradiated samples this difference is lower: 35 % for S79 and 50 % for S52.

The highest two temperature points of the S79 are lower due to a change in the measurement setup.

An interesting detail in figure 3.18 is that the ratio between the values for non-irradiated samples and their irradiated counterparts at the lower temperature range is different than at the higher range. In other words, the charge loss due to irradiation damage is lower for temperatures between 4 K and 75 K than for temperatures between 150 K and 295 K. The irradiated S52 collects 78 % of the initial charge in the low temperature range, but only 59 % of the initial charge for the high range. The values for S79 for these two temperature ranges are 100 % and 90 %, meaning that the drop in charge collection efficiency after irradiation to  $1 \times 10^{14} \pi \text{ cm}^{-2}$  is negligible for temperatures below 75 K. To sum up, charge trapping is present in irradiated samples across the entire temperature range, which is evident from the pulse shapes. However, the effect on overall collected charge is reduced for temperatures between 4 K and 75 K.

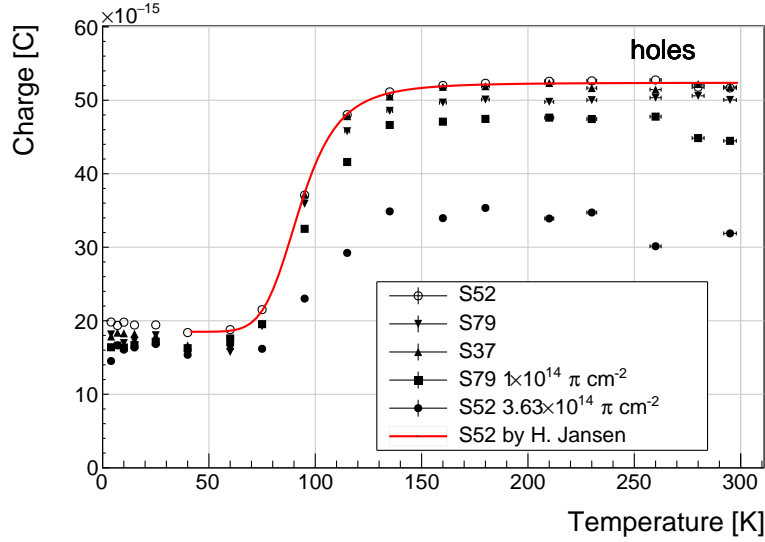


Figure 3.19: Collected charge for holes as a function of temperature.

### 3.4.2.2 Charge trapping

A decaying exponential function from equation 2.20 has been fitted to the decaying top of the averaged pulses at a bias voltages of  $\pm 400$  V and  $\pm 500$  V across all temperatures excluding the transitional range between 75 K and 150 K. The resulting decay time constants  $\tau$  are effective carrier trapping times. The values differ for individual temperature points due to changing pulse shapes with time by means of polarisation. This counts as a systematic error. Therefore the fitted  $\tau$  for  $\pm 400$  V and  $\pm 500$  V are averaged into one value representing the measurement at that temperature point. The time constants should be infinite for an ideal and non-irradiated sample.

As seen in figures 3.20a and 3.20b, the fitted values of the irradiated samples are fairly stable across all temperatures. There is a slight increase in the decay time constant of the S52 from  $(6.0 \pm 0.5) \times 10^{-9}$  s above 150 K to  $(8.5 \pm 0.9) \times 10^{-9}$  s below 75 K. This step is however not observable in the S79 data. With only one sample exhibiting this behaviour, the effect is not significant. Judging by the data acquired, the samples would need to be irradiated to doses above  $5 \times 10^{14} \pi \text{ cm}^{-2}$  to quantify this effect in detail. Building on this assumption, the conclusion is that the signal decay time constant for irradiated sCVD diamond is constant across the temperature range between 4 K and 295 K, excluding the transitional range between 75 K and 150 K where it cannot be quantified properly. All things considered, the values can be averaged into one single effective trapping time value for electrons and one for holes for further analysis. The effective trapping time is inversely proportional to the fluence [70]:

$$\frac{1}{\tau} = \beta \cdot \Phi \quad (3.8)$$

where  $\beta$  is the proportionality factor. A low  $\beta$  value would mean that the trapping centres in the sensor are created with a low rate. Figure 3.21 shows the inverse trapping times of the non-primed irradiated samples as a function of  $\pi_{300 \text{ MeV}}$  fluence.  $\beta$  is the slope of the fitted linear function. The fitted factors are  $\beta_e = (3.8 \pm 0.9) \times 10^{-16} \text{ cm}^2/\text{ns}$  and  $\beta_h = (3.4 \pm 0.8) \times 10^{-16} \text{ cm}^2/\text{ns}$ . Comparing to silicon detectors in [70], the value for the sCVD diamond is two times lower, meaning that it takes twice as much irradiation to create the same amount of charge traps in diamond than in silicon.

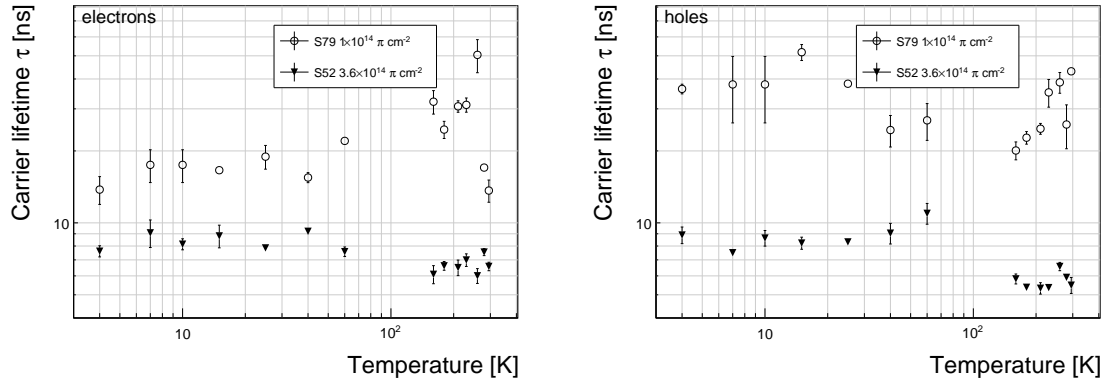


Figure 3.20: Charge carrier lifetime as a function of temperature for electrons and holes at  $\pm 400$  V and  $\pm 500$  V. The data points between 75 K and 150 K are omitted.

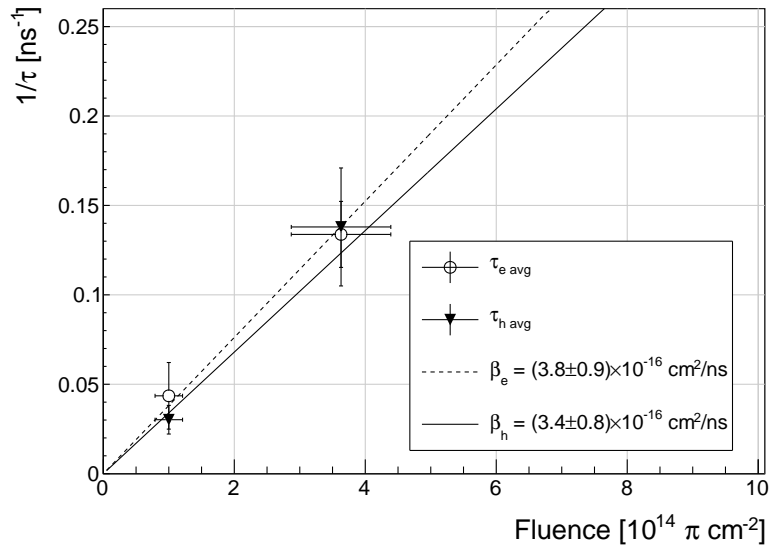


Figure 3.21: This figure shows the inverse charge trapping times averaged over all temperatures and plotted as a function of the  $\pi$  fluence.

### 3.5 Conclusion

This chapter gives an overview of the capabilities and limitations of diamond as a particle detector. Two effects on diamond are studied – radiation and temperature.

Two sCVD diamond detectors were irradiated with 300 MeV pions. They were tested alongside a non-irradiated sample to observe the changes in the ability to detect  $\alpha$ ,  $\beta$  and  $\gamma$  radiation. Their charge collection efficiency was measured in a test beam facility. The results were compared to the results from the RD42 collaboration and a DPA model. A radiation damage factor  $k_\lambda = (4.4 \pm 1.2) \times 10^{-18} \mu\text{m}^{-1} \text{cm}^2$  was obtained for  $\pi_{300 \text{ MeV}}$  particles. The data point was not in agreement with the data provided by RD42 nor with the model. Most likely this is because there was no diamond surface treatment done in between the measurements, as is the case in the study conducted by RD42. The results obtained in the course of these measurements are going to be fed into the existing pool of data in the RD42 collaboration.

The next step was to test the long-term capabilities for  $\alpha$  detection. The shape of the ionisation profile was investigated to determine the behaviour of the charge carriers in the irradiated diamond. An exponential decay was observed in the pulses of irradiated samples, proving that there are charge traps in the bulk that were created during irradiation. Then a long-term stability test was carried out. The results show that the irradiated diamond detectors do not provide a stable and reliable long-term measurement of  $\alpha$  particles. This might be due to a space-charge build-up in the bulk, which changes the electric field, affecting the charge carriers. A procedure to improve the pulse shape using  $\beta$  and  $\gamma$  radiation was proposed.

Finally, the diamond sensors were cooled down to temperatures between 4 K and 295 K. Their response to  $\alpha$  particles was observed. The results of the non-irradiated and irradiated samples were compared. The effect of reduction for the number of drifting charges due to exciton creation was observed in both sets of data. The second set had a superimposed effect of charge trapping during the drift, which was represented by an exponential decay in the signal. The decay time constant did not change with temperature. Therefore all temperature points for individual samples were averaged and the decay time constants were plotted as a function of fluence. Proportionality factors for defect production rate  $\beta_e = (3.8 \pm 0.9) \times 10^{-16} \text{ cm}^2/\text{ns}$  and  $\beta_h = (3.4 \pm 0.8) \times 10^{-16} \text{ cm}^2/\text{ns}$  for non-primed diamonds were extracted.

# Chapter 4

## Charge monitoring

### *The ATLAS Diamond Beam Monitor*

#### 4.1 Introduction

Particle detectors in high energy physics experiments need to meet very stringent specifications, depending on the functionality and their position in the experiment. In particular, detectors in the core of the experiment close to the collision point are subject to high levels of radiation. In addition, they need to operate with a high spatial and temporal segmentation to precisely measure trajectories of hundreds of particles within nanoseconds. Furthermore, they need to be highly efficient. In terms of the structure, their active sensing material has to be thin so as not to cause the particles to scatter or get stopped, which would have a negative effect on the measurements. This also means that they have to have a low heat dissipation so that the cooling system can be minimised or even avoided. Finally, they need to operate reliably for several years without a required intervention, because they are buried deep under tonnes of material and electronics.

The material of choice for the inner detector layers in the HEP experiments is silicon. It can withstand high doses of radiation, it is highly efficient (of the order of  $\sim 99.9\%$ ) and has a relatively low cost due to using existing industrial processes for its production. Its downside is that, with increasing irradiation levels, it needs to be cooled to increasingly low temperatures to ensure a stable operation. This is not the case with diamond. In addition, diamond has a lower radiation damage factor, which means it can operate in a radiation-heavy environment for a longer period.

The ATLAS Diamond Beam Monitor (the DBM) [71] is a novel high energy charged particle detector. Its function is to measure luminosity (described in section 4.2) and beam background (particles not originating in the collision point) in the ATLAS experiment. Given the DBM's position in a region with a high radiation dose, diamond was chosen as the sensing material. The monitor's pCVD diamond sensors are instrumented with pixellated FE-I4 front-end chips. pCVD diamond was chosen due to the durability of the sensors in a radiation-hard environment and to the size of its active area. The DBM is not the first diamond detector used in HEP, but it is the largest pixellated diamond detector installed thus far, as shown in figure 4.1. It was designed as an upgrade to the existing luminosity monitor called the Beam Conditions Monitor (BCM) [72] consisting of eight diamond pad detectors. The BCM is able to perform precise time-of-flight (ToF) measurements. The DBM complements the BCM's features by implementing a tracking capability. Its pixelated front-end electronics significantly increase the spatial resolution of the system, allowing it to distinguish particle tracks originating in the collision region from the background hits. This capability is a result

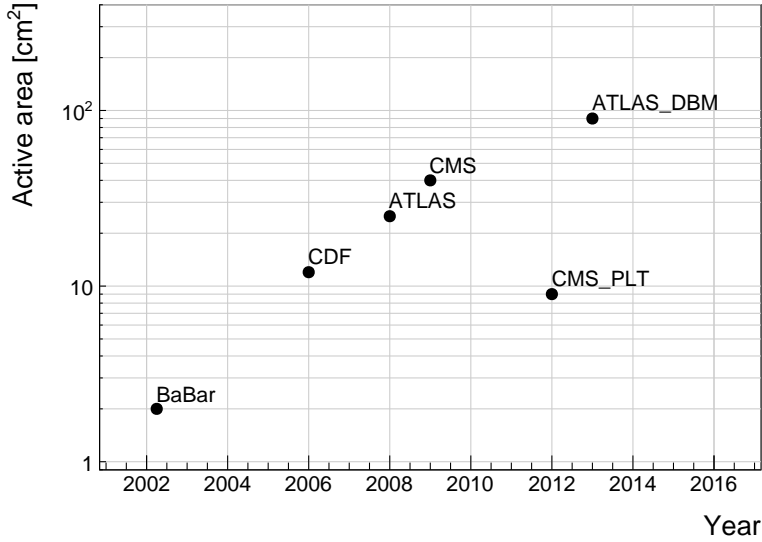


Figure 4.1: Diamond detectors installed in high-energy physics experiments in the last decade, sorted by the active sensor area. The first four detectors from the left are radiation monitors whereas the right two are pixel trackers.

of its projective geometry pointing towards the interaction region. This chapter first describes the principles of luminosity measurements. It then explains how the DBM carries out this task. Finally results from the commissioning and from the real collisions are presented.

## 4.2 Luminosity measurements

Luminosity is one of the most important parameters of a particle collider. It is a measurement of the rate of particle collisions that are produced by two particle beams. It can be described as a function of the beam parameters, such as: the number of colliding bunch pairs, the revolution frequency, the number of particles in each bunch and bunch dimensions. The first three parameters are well defined. However, the transverse bunch dimensions have to be determined experimentally during calibration measurements. The ATLAS experiment uses the *van der Meer scan* [73] during low-luminosity runs to calibrate the luminosity detectors – this scan is otherwise primarily used to check the beam alignment. This scan is performed by displacing one beam in a given direction and measuring the rate of interactions as a function of the displacement. The transverse charge density of the bunches can be estimated on the basis of the interaction rate. The calibrated luminosity detectors can then operate during high-luminosity runs.

One approach to luminosity monitoring is to count the number of particles produced by the collisions. Luminosity is then proportional to the quotient between the number of detected collisions and the cross-section of the proton-proton collisions. The cross-section is measured to be approximately 50 mbarn for inelastic interactions [74, 75] and 110 mb including elastic and single diffractive [76]. A detector has to be capable of distinguishing between particles that originate in the interaction point through the active sensor area and those originating elsewhere. If the detector has at least three layers of sensors, it can reconstruct the tracks of particles, determining whether they originate in the interaction point or elsewhere (see figure 4.2. This is one reason why detectors with a high timing and spatial segmentation are more suitable for these applications. The second reason is that,

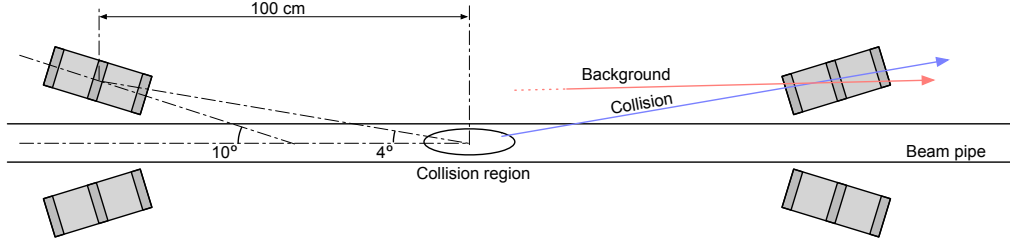


Figure 4.2: Position of the DBM in the ATLAS experiment.



Figure 4.3: A pCVD wafer [77]. The gold dots on the surface are the Cr/Au electrodes that are applied during the qualification test. The wafer is measured across the surface to find the regions with the highest efficiency.

with a high spatial segmentation, the detector does not saturate even at high particle fluencies.

### 4.3 Diamond pixel module

The two most important parts of the diamond pixel module are the sensor, which detects the incident radiation by means of ionisation (creation of charge carriers as explained in chapter 2), and the pixellated front-end chip, which collects the ionised charge with a high spatial segmentation, processes the recorded data and sends them to the readout system. This section describes these two parts of the module and their interconnection.

#### 4.3.1 Sensors

The DBM modules are instrumented with two types of sensors – pCVD diamond and silicon. The silicon sensors are used to allow for a comparative study of irradiation damage between silicon and diamond.

**Diamond sensors** The target material for this application is pCVD diamond. The reason for this is that the active area of an individual sensor must be approximately  $2\text{ cm} \times 2\text{ cm}$ , which is too large for the sCVD diamond. pCVD material is also cheaper, which decreases the production cost of a detector with a large active area. The material is provided by three companies: DDL (now defunct), E6 [57] and II-IV [78] and it is grown in 15 cm wafers, as seen in figure 4.3. The target

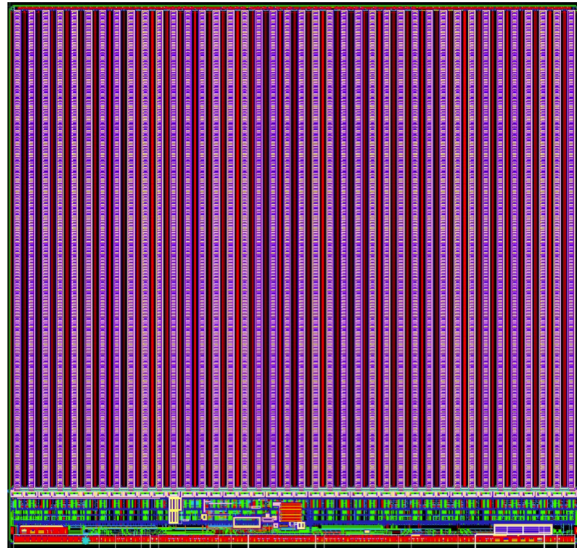


Figure 4.4: FE-I4 layout, top-down view. The purple area are pixels grouped into columns, the green area below is the common logic and the red strip at the bottom are the wire bond pads.

thickness of the wafers is 500  $\mu\text{m}$ . Minimum required charge collection efficiency is 40 % ( $\text{CCD} \geq 200 \mu\text{m}$ ) to ensure that the MPV of the collected charge for MIPs is still well above the noise of the electronics even after heavy irradiation. The nominal bias voltage is between 600 V – 1'000 V. On one side there is a single Cr/Au electrode applied across the entire surface. On the other side a pixellated metallisation is added.

**Silicon sensors** are standard  $n^+ -in-n$  planar sensors with a 200  $\mu\text{m}$  thickness and were fabricated at CiS [79], a company from Erfurt, Germany. They are designed to have nearly a 100 % efficiency when not irradiated. One side is segmented into pixels. Guard rings at the edges of the sensor provide a controlled drop in potential, reducing the possibility of sparking at maximum design bias voltages of the order of 1'000 V [60, 80].

### 4.3.2 Front-end electronics

The FE-I4 (front-end integrated circuit) [81] is an ASIC pixel chip designed specifically for the ATLAS pixel detector upgrade. It is built as a successor to the current pixel chip FE-I3, surpassing it in size of the active area (6× larger) as well as the number of channels/pixels (10× more). 336 such FE-I4 modules are used in the newly installed pixel layer called the Insertable B-Layer (IBL) [82]. The DBM is also instrumented with these chips. The FE-I4's integrated circuit contains readout circuitry for 26'880 pixels arranged in 80 columns on a 250  $\mu\text{m}$  pitch and 336 rows on a 50  $\mu\text{m}$  pitch. The size of the active area is therefore 20.0 cm × 16.8 mm. This fine granularity allows for a high-precision particle tracking. The chip operates at 40 MHz with a 25 ns acquisition window, which corresponds to the spacing of the particle bunches in the LHC. It is hence able to correlate hits/tracks to their corresponding bunch. Furthermore, each pixel is capable of measuring the deposited charge of a detected particle by using the Time-over-Threshold (ToT) method [60]. Finally, the FEI4 has been designed to withstand a radiation dose up to 300 Mrad. This ensures a longterm stability in the radiation-hard forward region of the ATLAS experiment.

Each pixel is designed as a separate entity. Its electrical chain is shown in figure 4.5. The bump-bond pad – the connection to the outside of the chip – is the input of the electrical chain,

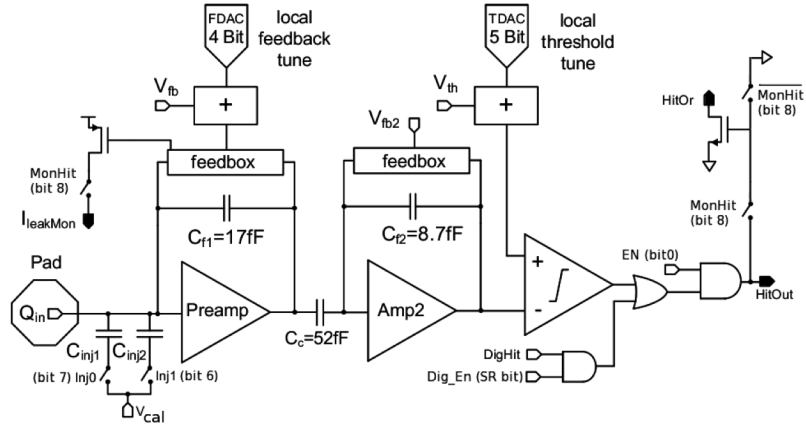


Figure 4.5: Schematic of an analog pixel. Courtesy of the FE-I4 collaboration.

connected to a free-running amplification stage with adjustable peaking time using a 4-bit register at the feedback branch. The analog amplifier is designed to collect negative charge, therefore electrons. The output is routed through a discriminator with an adjustable threshold. This value in effect defines the level at which the circuit detects a hit. In addition, there is an incrementing counter (25 ns sampling) that measures the time the signal is above the discriminator threshold. The value of the counter (Time-over-Threshold) is proportional to the collected charge. The logic gates at the end of the chain are used to enable/disable the pixel and to issue a HitOr flag – this signal is set whenever at least one of the pixels was hit and can be used as a trigger for data readout. The output of the chain – HitOut – is routed into the logic of the chip where it is buffered and sent out to the readout system. The module receives all its commands from the system via a 40 MHz LVDS line. The commands are either settings for the pixel registers or triggers that start the data readout. The data are sent via an LVDS line at 160 Mbit/s, four times faster than the input clock of the device, improving the data throughput. The FE-I4 has been successfully tested for trigger rates of up to 100 kHz, depending on the occupancy per trigger.

The DBM uses pCVD diamond with  $d_C = 500 \mu\text{m}$  thickness and silicon with  $d_{Si} = 200 \mu\text{m}$  thickness as a sensor material. The most probable value (MPV) of the deposited charge for a minimum ionising particle (MIP) is calculated with the formula  $Q_S = d \cdot E_{e-h}$  and equals 18'000 electrons and 17'800 electrons, respectively, at a full charge collection efficiency. This is not the case with the pCVD material, whereby the expected charge collection efficiency is of the order of 50 % – around 9'000 e. This value further decreases with irradiation. Therefore in order to detect the particles depositing energy on the far left side of the Landau spectrum, the threshold has to be set to a significantly lower value. On the other hand, if the threshold is set too low, the electronic noise above the threshold starts generating false hits. Typical noise amplitudes are 100 e for diamond and 125 e for silicon. A safe threshold range is approximately five times above this value. The target for the DBM is to set the threshold to 800 e.

The analog amplifier is implemented in two stages to get a fast rise time at a low noise and a low power consumption. The output signal of the analog amplifier has a triangular shape with a fast rise time and a long decay. The shape can be adjusted by tuning the amplifier feedback loop. Its ToT is proportional to the collected charge, but it needs to be calibrated first. This is done by means of two injection capacitors,  $C_{inj1}$  and  $C_{inj2}$  with well defined capacitances, seen in figure 4.5. First, the charge  $Q_{cal} = V_{cal} \cdot (C_{inj1} + C_{inj2})$  is injected into the analog chain. Then the length of the

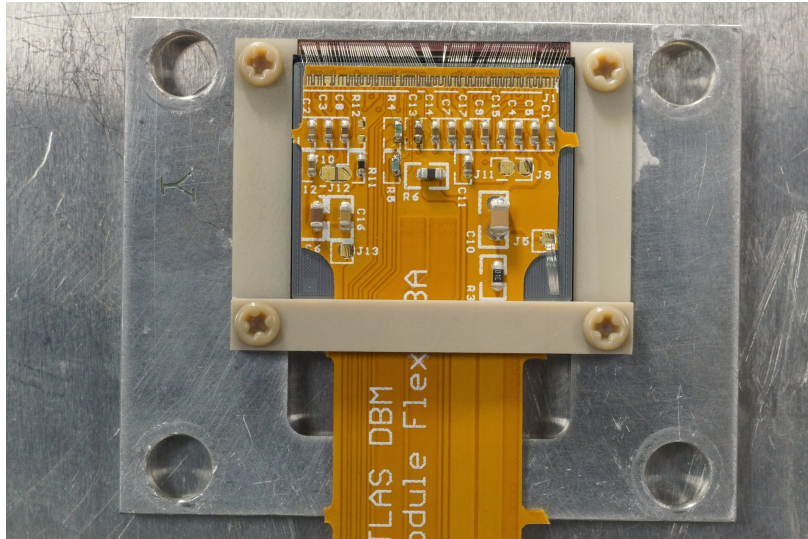


Figure 4.6: DBM module, top-down view. Visible is the flexible PCB with signal and power connections, the silicon sensor and a part of the FE-I4. Wire bonds from the PCB to the FE-I4 and to the sensor are also visible.

output pulse is measured and finally the feedback value is changed to either lengthen or shorten the pulse in order to get to the required duration  $t_{\text{cal}}$ . Typical values are  $Q_{\text{cal}} = 5'000 \text{ e} - 16'000 \text{ e}$  at the time  $t_{\text{cal}} = 5 \text{ ToT} - 10 \text{ ToT}$ . Target values depend on the sensor, the type of a radioactive source and the application. Therefore the initial threshold  $Th$  at 1 ToT and the calibrated value  $Q_{\text{cal}}$  at  $t_{\text{cal}}$  ToT yield a linear scale of collected charge with respect to time over threshold. However, in practice this relation is nonlinear for lower thresholds, but since the goal of the measurements is to track the particles rather than to measure their deposited energy precisely, this is sufficient.

## 4.4 Module assembly

A DBM single-chip module shown in figure 4.6 consists of a hybrid pixel module, a flexible PCB and the supporting mechanics (a ceramic plate and an aluminium plate). The chip arrives already bump-bonded to the sensor, be it diamond or silicon. First it is glued to the ceramic plate on one side and to the PCB on the other using Araldite 2011 or Staystik 672/472. Staystik is re-workable and has a very high thermal conductivity. The latter is important because the FE-I4 chips tend to heat up significantly and need a good heat sink. The problem is that it has a curing temperature of 160/170 °C. This temperature may cause some unwanted stress build-up between the FE-I4 and the diamond sensor due to different coefficients of thermal expansion, pulling them apart. This would disconnect the pixels, yielding large regions of the module insensitive to radiation. Araldite 2011 on the other hand can be cured at lower temperatures – down to room temperature – but it has a lower heat conductivity. In the end Araldite is used as a safer option despite longer assembly times. After curing, the module is wire-bonded and attached to the aluminium plate using screws made up of a radiation-resistant PEEK polymer. The gap between the screw head and the sensor edge is only 0.2 mm – 0.6 mm – the sensor displacement tolerance during gluing is of the order of 0.5 mm. Finally, the module is put in an aluminium carrier which protects it from mechanical damage or electrostatic discharges during the QA procedure.

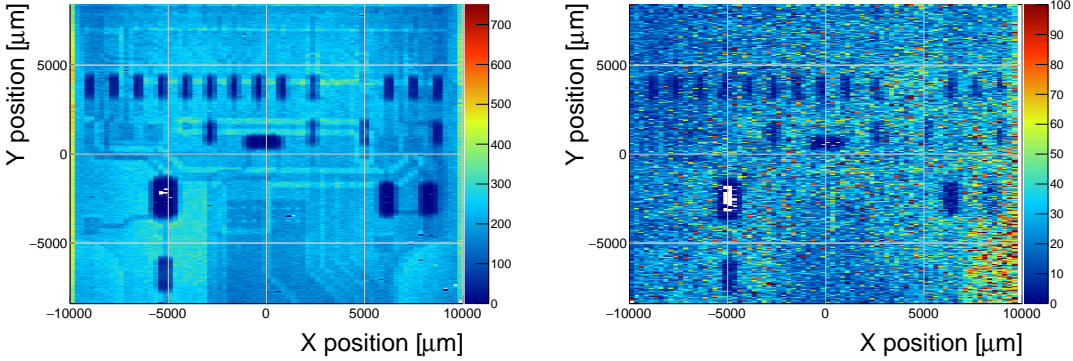


Figure 4.7: Occupancy scans for the silicon (left) and diamond sensor (right) to check for disconnected regions. Shadows of the electronic components are clearly visible because fewer electrons were able to traverse through a large amount of material.

## 4.5 Performance results

This section gives an overview of the performance results of the DBM modules achieved during the QC and the test beam campaign. Source tests were carried out to check for disconnected regions in the sensors and to measure the efficiency of individual modules. Only the modules with less than 3 % disconnected regions and more than 55 % efficiency were chosen for installation.

### 4.5.1 Source test results

The modules are tested in the lab using the Reconfiguration Cluster Element readout system [83] and a moving stage with two degrees of freedom. They are placed onto the stage and connected to the readout system and the power supplies. After ensuring the low and high voltage connectivity they are checked for digital signal connectivity. If everything is operational, a series of automated tests is run. Each of these tests calibrates a certain value within a pixel, whether it is the signal threshold or the value for integrated charge. These are tuned so that the response to a predefined calibration signal is uniform for all pixels across the sensor. This procedure is referred to as *tuning* [60]. When the modules have been tuned, a  $^{90}\text{Sr}$  radioactive source is used for source tests. Two characteristics of each module are checked: 1) operation and connectivity of individual pixels and 2) sensor efficiency.

#### 4.5.1.1 Pixel connectivity

The first test is carried out to determine the number of disconnected pixels in the matrix. Pixel connectivity is the most important qualification factor in the QC procedure. However, the only way to check it at the moment is to fully assemble a module and test it using a radioactive source. If the module turns out to be of poor quality, it is disassembled and sent for rework. Lead time of this operation is of the order of one month.

The test for disconnected regions is carried out by moving the module under the source in X and Y direction so that the exposure over the entire plane is uniform. The resulting occupancy map reveals the pixels that are not electrically coupled to the sensor via bump bonds. The occupancy scans are shown in figures 4.7a and 4.7b. The silicon module has a very uniform occupancy plot. So much so that the features of the overlaying flexible PCB can be observed. The rectangular shadows are the passive components whereas the lines are the traces in the PCB. Furthermore, a circular-

## 4.5. PERFORMANCE RESULTS

---

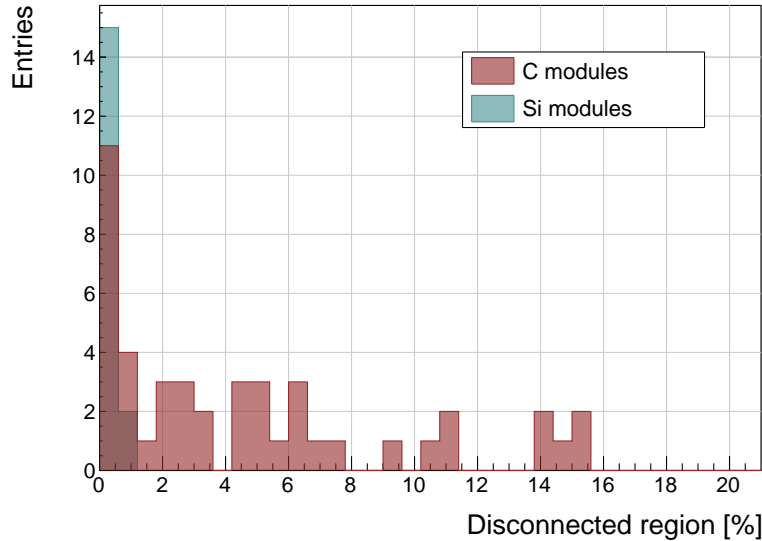


Figure 4.8: Disconnected regions for all modules derived from the occupancy scans.

shaped edge of the PCB can be seen on the bottom right side of the plot. These darker areas are such because fewer electrons can penetrate the material with a high density. In the case of the diamond, the features of the PCB can be observed as well, but are much less distinguishable as the plot is much more granulated – less uniform. This high variance in the diamond’s detection ability is due to the grain boundaries in the pCVD material which trap the drifting charges, rendering some regions significantly less efficient.

A significant number of the tested diamond sensors exhibit very poor connectivity. As shown in figure 4.8, the disconnected regions on the faulty modules range from 0.1 % to 16 % of the overall active surface. In some cases (not shown in the figure) the sensor only had a 20 % connectivity or has even completely detached from the chip. In the end the modules with less than 3 % disconnected pixels have been accepted. Silicon modules are performing as expected, with a minimum number of disconnected pixels.

### 4.5.1.2 Pseudo-efficiency

Only the modules that passed the pixel connectivity test undergo the second test stage in which the sensor’s efficiency is estimated. A scintillator is placed underneath the module and is used as a trigger. A particle that crosses the DBM module and hits the scintillator, triggers the module readout. In the end, the number of triggers is compared to the number of hits/clusters recorded by the module. These are shown in figures 4.9a and 4.9b.

However, the resulting ratio is only an estimate of the sensor’s detection efficiency. This is because the  $\beta$  particles scatter around the setup and sometimes hit the scintillator from other directions without traversing the module, producing empty triggers. Therefore the real sensor efficiency can only be measured in a high energy particle beam and using a beam telescope as a reference detector to measure the particle trajectories. Nonetheless, this *pseudo-efficiency* gives a rough estimate of the sensor’s quality.

Figure 4.10 shows the distribution of pseudo-efficiencies for all modules that underwent the QC. The threshold setting for silicon and diamond modules is 3000 e and 1100 e (or 1500 e for

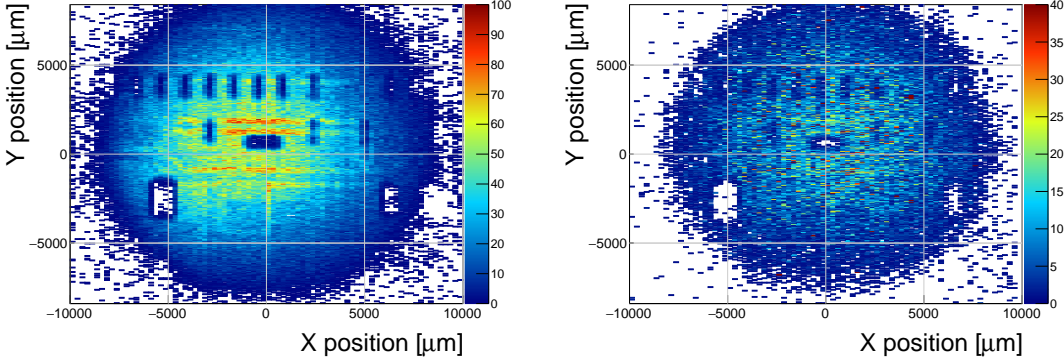


Figure 4.9: Pseudo-efficiency scans for the silicon (left) and diamond sensor (right) to estimate the efficiency of the sensors.

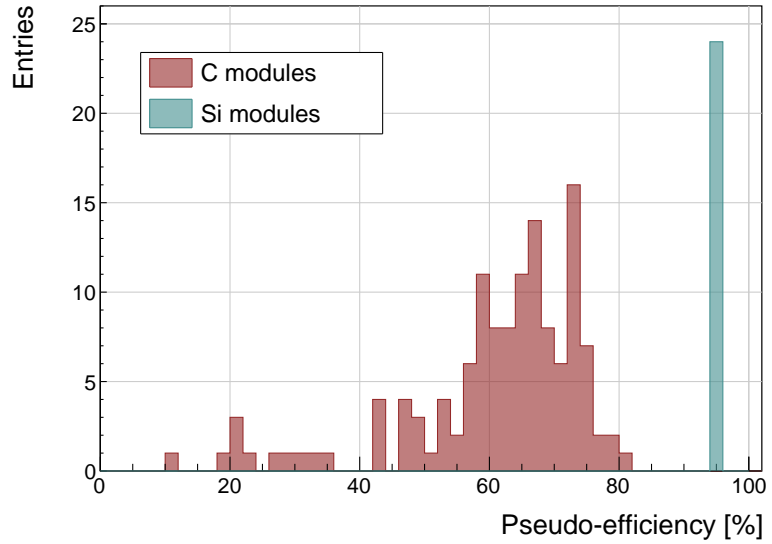


Figure 4.10: Pseudo-efficiencies for all modules at various threshold and voltage settings.

those modules that were noisy at lower thresholds). The majority of the silicon modules yield the pseudo-efficiency of  $(94.3 \pm 0.2)\%$ . Silicon sensors have a quoted 99.9 % efficiency [60], so this value is underestimated by about 5 %. The measured pseudo-efficiency of the diamond modules is  $(65 \pm 7)\%$ , with outliers down to 10 %. The value depends on the diamond quality, the set threshold and the applied bias voltage. The latter two settings are varied to check the behaviour of the modules under various conditions. Analogue to the offset between the pseudo-efficiency and efficiency of silicon, the actual efficiency of the measured pCVD diamond sensors is expected to be approximately 5 % higher.

#### 4.5.2 Erratic current

A very important parameter for qualifying a module is the erratic current [84] in the sensor. This term describes the leakage current in pCVD diamond that becomes unstable. It can develop gradually or can be triggered with a  $\beta$  source. Spikes appear in the otherwise stable leakage current.

## 4.5. PERFORMANCE RESULTS

---

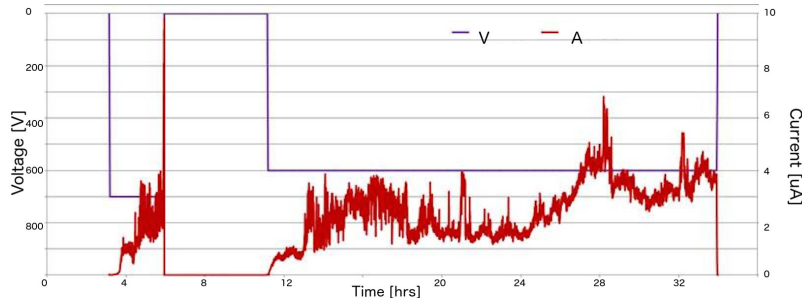


Figure 4.11: Erratic current in a DBM diamond module. The purple and the red signal line represent the applied negative bias voltage and the measured leakage current.

They can be up to three orders of magnitude higher than the base current. Sometimes the current also suddenly increases for a few orders of magnitude and stays at that level (e.g. from the initial 1 nA to 3  $\mu$ A). An example of such behaviour is shown in figure 4.11.

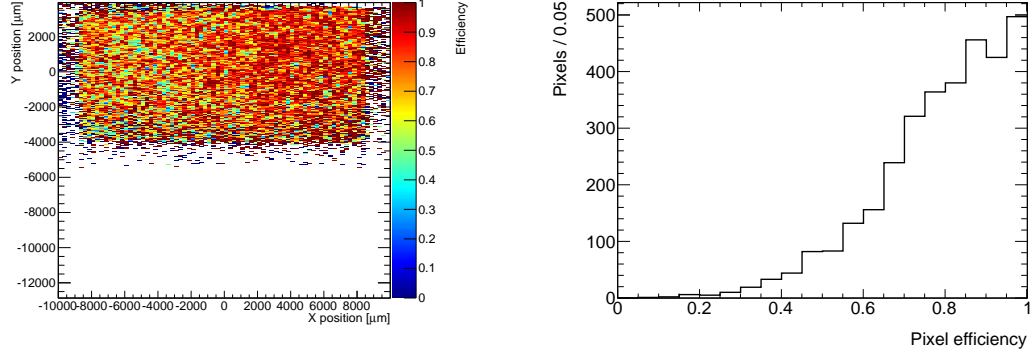
The amplitude differs in magnitude from sensor to sensor. This effect is still not fully explained, but the hypothesis is that the moving charges find a conductive channel along the grain boundaries, causing discharges. These discharges are picked up by the pixel amplifiers in the FE-I4. A single discharge can trigger a group of up to  $\sim$ 500 pixels, resulting in a *blob* on the detector occupancy map. Sometimes the conductive channel stays in a conductive state, making one or more pixels always to fire. These pixels saturate the bandwidth of the readout channel, so they have to be masked out during measurements.

### 4.5.3 Test beam results

The first two assembled prototype DBM modules, MDBM-01 and MDBM-03, were tested at DESY, Hamburg, in a test beam facility. The aim of the measurements was to measure their efficiency, the spatial distribution of the efficiency and the effect of the beam on the disconnected regions. A silicon module MSBM-02 was measured to crosscheck the measurements. Since the silicon module is almost 100 % efficient, it was used as an “anchor” – the efficiency of the diamond module was measured relative to that of the silicon module. Two beam telescopes were used as reference systems: Kartel telescope [85] built by JSI institute from Ljubljana, and EUDET Aconite [86]. Both are instrumented with six Mimosa26 pixel planes and capable of tracking particles with a 2  $\mu$ m pointing resolution.

The test beam prototypes did not meet the acceptance criteria for production DBM modules in the following areas: first, the reported CCDs were slightly below 200  $\mu$ m, which would be the DBM minimum. Second, the applied bias voltages ranged from 1–2 V/ $\mu$ m, which is in some cases below the minimal required value. In addition, the threshold cut could only be set to 1'500 electrons, which is higher than the DBM minimum (1'000 e). Nonetheless, the resulting module efficiencies were still in the range between 70–85 %.

To analyse the test beam data, Judith software framework [85] was used. Judith is capable of synchronising data streams from several detector systems only connected via a trigger system, reconstructing tracks and calculating efficiency for the DUTs (devices under test). It was also used to reconstruct and analyse the acquired Kartel test beam data together with the silicon and diamond module as DUTs. A sample of the analysed data is shown in figures 4.12a and 4.12b. First figure shows the efficiencies for individual pixels of the MDBM-03 diamond module. Only the top half of the sensor is measured because the telescope trigger window is smaller than the sensor area. The map is non-uniform (granulated) due to grain boundaries of the pCVD material, which cause



(a) This figure shows an efficiency map of ad DBM diamond module. Each bin corresponds to a single pixel. The triggering scintillator of the Kartel telescope is smaller than the DUT. Hence, the recorded hits can only be seen in the top half of the sensor.

(b) A pixel efficiency distribution across the module. A large number of pixels is either fully efficient or is close to 100 % but the distribution is broad and reaches almost 0 % for a small number of pixels.

Figure 4.12: An efficiency study of a prototype DBM diamond module in a test beam [71, 85]. The statistics are low ( $\sim 10$  hits/pixel) as the data were collected during a short run.

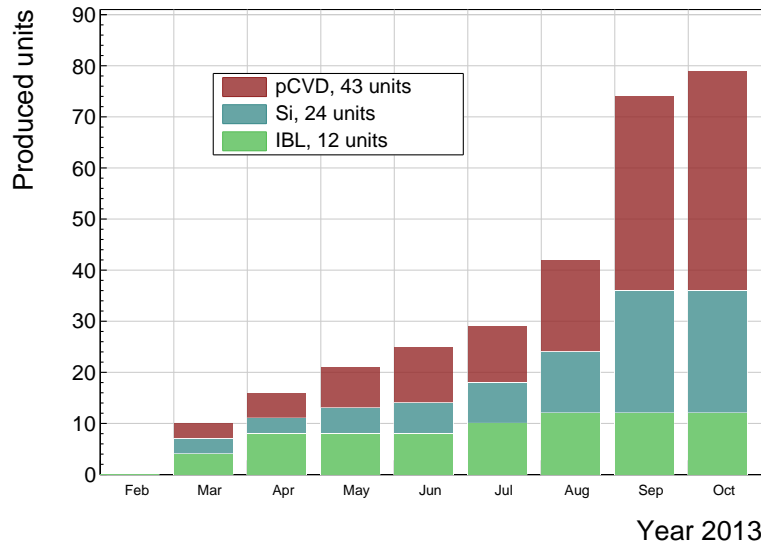


Figure 4.13: Module production with time.

high efficiency gradients at a  $\mu\text{m}$  scale. The second figure shows the efficiency distribution for the measured pixels.

#### 4.5.4 Summary of the QC

All in all, 79 modules went through the QC procedure – 43 diamond modules and 36 silicon modules, 12 of the latter only for testing purposes. Figure 4.13 shows their production with time. 18 diamond modules and 6 silicon modules were in the end chosen to be integrated into DBM telescopes and installed into ATLAS.



Figure 4.14: This photo highlights four telescopes installed onto the nSQPs and around the pipe.

## 4.6 Installation and commissioning

The DBM modules that passed the QC tests were assembled into telescopes – sets of three modules, one behind the other, with a spacing of 50 mm. All in all 6 diamond and 2 silicon telescopes were built out of 18 diamond and 6 silicon modules. A special care was taken when choosing the sets of three diamonds. The modules with a similar pseudo-efficiency, leakage current, maximum stable high voltage and shape of disconnected regions were grouped together. After assembly into telescopes, the modules were tested for their connectivity. Then the high voltage was applied and the leakage current was observed. This was an important point to check because all three modules shared the same high voltage channel. Any instabilities on one of the modules would cause problems on the other two. This would for instance happen if one of the modules had a much lower breakdown voltage.

The telescopes were installed onto the pixel detector structure that had been extracted from ATLAS due to pixel detector commissioning. After every installation, the telescopes were tested again. First, the low voltage connectivity was checked and a set of tests was run on the FE-I4 front-end chips. An eye diagram was made to estimate the quality of the signal transmission. Then a  $^{90}\text{Sr}$  source was used to perform a source test on three modules at the same time. Leakage current was observed during the source test. The final test included running four telescopes (all on one side) at a time. All tests were successful and the DBM was signed off.

### 4.6.1 Positioning in ATLAS

The installed DBM is shown in figure 4.14. The DBM is placed in the forward region of the ATLAS detector very close to the beam pipe, as shown in figure 4.2 in section 4.2. Eight DBM telescopes reside approximately 1 m away from the collision region, four on each side. They are tilted with respect to the beam pipe for 10°. This is due to a specific phenomenon connected to erratic currents in diamond. Studies have shown [84] that the erratic leakage currents that gradually develop in diamond can be suppressed under certain conditions. For instance, if a strong magnetic

field is applied perpendicular to the electric field lines in the diamond bulk, the leakage current stabilises. The DBM was designed to exploit this phenomenon. The magnetic field lines in the ATLAS experiment are parallel to the beam. Hence, an angular displacement of the sensor with respect to the beam allows for the leakage current suppression. However, the DBM telescopes still need to be directed towards the interaction region. Taking these considerations into account, a 10° angle with respect to the beam pipe was chosen. The influence of the magnetic field on particle tracks at this angle is very low as the field lines are almost parallel to the tracks. The tracks are therefore straight, which reduces the track reconstruction complexity.

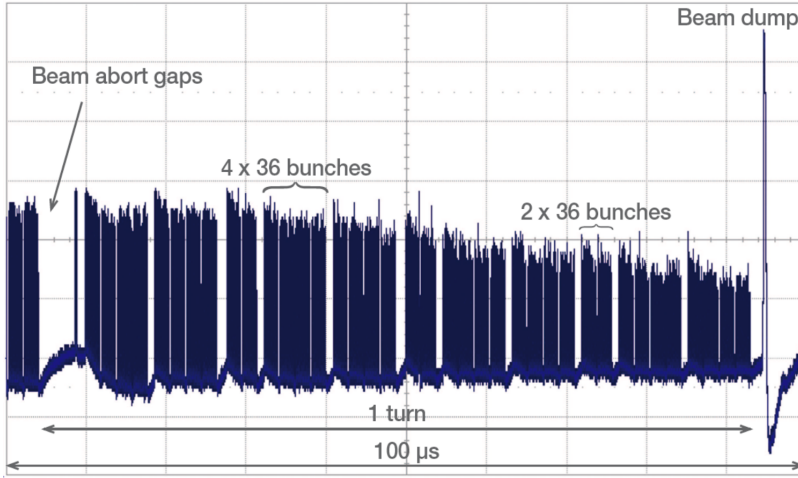


Figure 4.15: Time-resolved bunch structure at the LHC measured by diamond detectors [87]. The beam abort gap is clearly visible.

## 4.7 First collision data

The detector's capability of particle tracking has been tested during collisions. Only one telescope was used to take data.

### 4.7.1 LHC beam bunch structure

As described in chapter 1, the LHC accelerates two beams of protons in opposite directions, intersecting at four collision points. Collisions take place in a collision region around the nominal collision point, with a gaussian spread. The particles in the beam are grouped in bunches. Not all bunch buckets are filled. For example, a long *abort gap* between bunches shown in figure 4.15 allows for enough time for the steering magnets to dump the beam in an event of beam instabilities or at the end of fill. Therefore some bunches arriving at the collision point do not have their corresponding bunches traveling in the opposite direction. These are referred to as non-colliding or *unpaired bunches* while those with their respective bunches in the opposite direction are *paired*. The unpaired bunches should not create any collisions. Nevertheless, some collisions might still be detected, whether as a result of stray particles hitting the beam pipe or the surrounding detectors or if the purportedly empty buckets still contain a small number of particles that “spilt over” from the filled buckets.

### 4.7.2 Collision point reference system

If all three planes of the telescope are hit during a bunch crossing, a linear line is fitted to these hits and extrapolated towards the interaction region. This line represents the particle's trajectory. Two parameters are calculated: the radial distance  $D_0$  and the longitudinal distance  $Z_0$  between the line and the interaction point, as shown in figure 4.16.  $D_0$  and  $Z_0$  values are cylindrical coordinates of the distance of closest approach of the particle's trajectory to the nominal interaction point. Figure 4.17 shows the theoretical gaussian distribution of  $D_0$  and  $Z_0$  (black) as well as the expected distribution as measured by one DBM telescope (blue). The latter is biased due to the positioning and the aperture of the telescope. The red distribution shows the contribution of the particles colliding with the beam pipe and the surrounding electronics, such as the IBL [88].

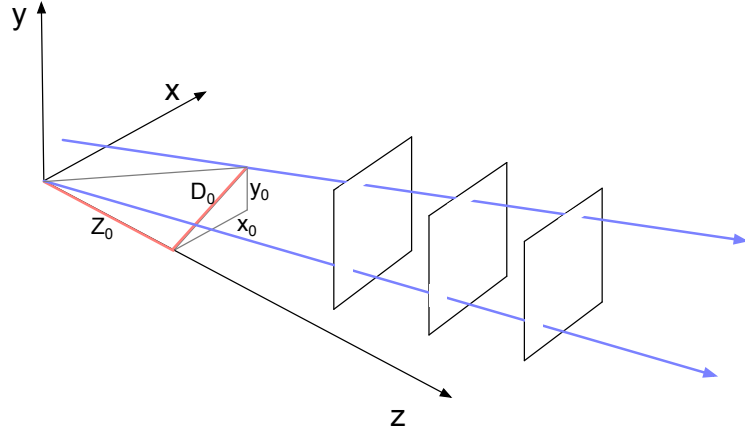


Figure 4.16: Two particle tracks. One originates in the centre of the collision region. The vertex of the other is at the radial distance  $D_0$  and longitudinal distance  $Z_0$  from the interaction point. Axis  $z$  is the beam direction. Three module planes intercept the particles and reconstruct their trajectory. The arrow on the top right shows the telescope used for data acquisition.

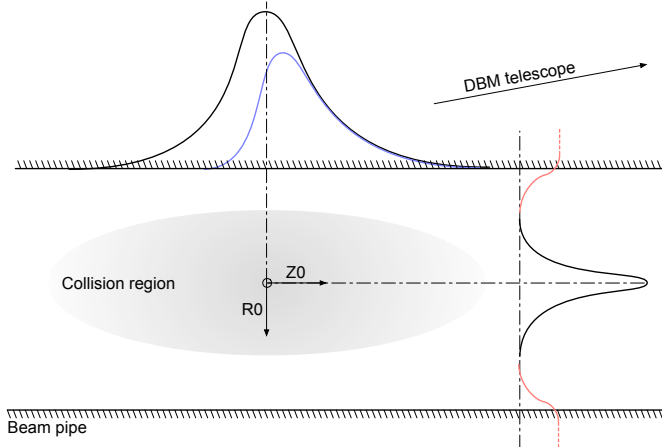


Figure 4.17: Expected distribution of collision points in the collision region (black). A single DBM telescope taking data records the collisions with a biased distribution marked blue. The red distributions stem from collisions of stray particles with the beam pipe or surrounding material.

### 4.7.3 Discussion

The data acquired with a single DBM telescope are shown in figures 4.18a and 4.18b. Histograms for collisions of paired and of unpaired bunches are plotted separately for each of the two cylindrical coordinates. For the colliding bunches, the majority of the reconstructed tracks has the origin close to the nominal interaction point, with a narrow spread in  $Z$  and  $R$ . A slight negative displacement in  $D_0$  and a positive displacement in  $Z_0$  are expected due to the positioning of the telescope.

For non-colliding bunches, the spread is wider. The  $D_0$  distribution has one peak in the middle, which means that the empty buckets still hold some particles that collide. The two peaks on the sides, however, show that a significant number of tracks has their origin at the radius of the beam pipe. Therefore these tracks are made by secondary particles created by stray protons that collided

## 4.8. CONCLUSION

---

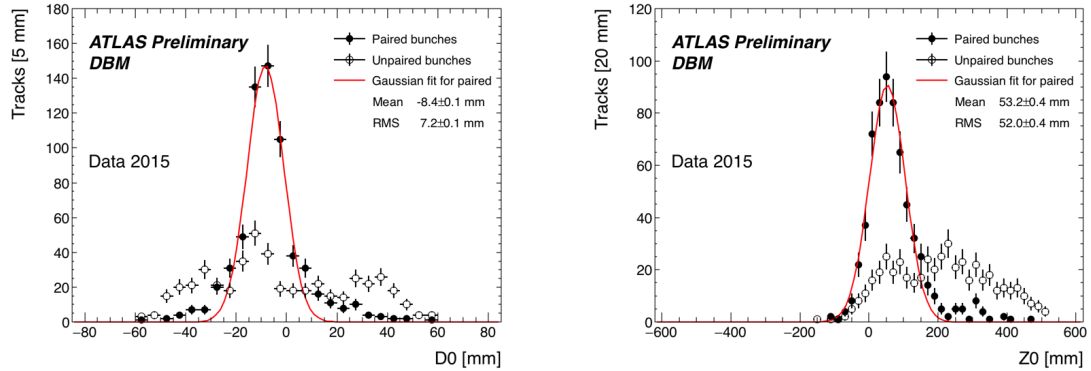


Figure 4.18: These two plots show two parameters of particle tracks recorded by one of the DBM telescopes: radial (left) and longitudinal (right) distance of the projected tracks from the interaction point. Note the different scale on the  $x$  axis. The red, blue, yellow and green lines mark the inner and outer radius of the beam pipe, the outer radius of the IBL and the outer radius of the IBL insertion tube [80, 88].

with the beam pipe and the surrounding material. These collisions are unwanted as they do not produce any meaningful physics while still damaging the ATLAS detector by means of the scattered radiation.

The  $Z_0$  distribution has a high spread in the positive direction. This bias is due to the positioning of the telescope and its angular acceptance. The peak that coincides with that of the paired bunches stems from collisions of stray particles. The second peak with a wide spread is due to collisions with the surrounding material.

## 4.8 Conclusion

The Diamond Beam Monitor has been designed as an upgrade to the existing luminosity detectors in the ATLAS experiment. It is the first diamond pixel tracking detector installed in a high-energy physics experiment. The pixelated front-end electronic chips ensure precise spatial detection of the charged high-energy particles. The projective geometry allows for particle tracking and background rejection. The detector is placed in a high-radiation forward region of the experiment. Therefore, radiation hardness of the chosen pCVD diamond sensors is an important requirement. The tests carried out in the test beam and in the laboratory confirmed that enough detector-grade DBM modules have been built to be installed in the experiment. The DBM is has been running in ATLAS since October 2013.

# Chapter 5

# Current monitoring

## *Real-time particle identification*

Diamond sensors have a very fast signal response due to their low capacitance. When the sensor is used together with a fast current amplifier with a high broadband limit ( $\sim 2$  GHz) and a readout device with a similar limit, the information about the drifting charges is retained. For instance, a proton creates the free e-h pairs along its trajectory. The electrons and holes start drifting immediately. Those closest to the electrodes recombine quickly whereas those at the opposite side contribute to the induced signal for longer. The resulting signal is therefore a triangular pulse with a steep rising edge and a gentle falling edge. It is possible to determine the drift velocity of the charge carriers by measuring the width of the pulse, as was done in chapter 3. Furthermore, it is possible to determine with a certain probability what is the type of incident radiation, judging by the shape of the induced pulse. This, however, only applies to sCVD diamond material. Its uniform carbon lattice allows the ionisation profiles to retain their shape, unlike in pCVD material, laden with grain boundaries, or in even in silicon where the shape is deformed due to p-n junction non-uniformities.

This chapter describes an application that performs particle identification by means of the pulse shape analysis. It was developed for measuring activity of neutron reactors. In this case the device has to be able to filter out the photon background with a rate several orders of magnitude higher than the neutron rate. Overall detected rate in a neutron reactor can easily exceed  $10^8$  particles  $\text{cm}^{-2}\text{s}^{-1}$ , depending on the distance of the detector from the reactor core. The device has to be able to cope with such high rates. It also needs to be dead time free or at least close to that, to minimise the counting error. At these rates, it still has to be able to identify the types of pulses. This type of online analysis cannot be done in software. It has to be implemented in an FPGA.

### 5.1 Motivation

Pulse shape analysis (PSA) is a common software tool for extracting information from electrical signals created by the sensors. It is usually done by means of software analysis run over large amounts of data acquired and saved to storage. This offline analysis can be repeated and improved. However, the saved data take up a lot of storage space. In addition, saving raw waveform data requires a system capable of a high data throughput and fast data storing. For instance, an oscilloscope can save up to 100 signal waveforms per second. This means that there is a high measurement dead time. To avoid high dead times, the software algorithms can be ported to the FPGA where they analyse the incoming signal in real time. The saved analysis results take far less space than full

## 5.2. REQUIREMENTS

---

waveforms, which decreases the storage space significantly.

The offline pulse shape analysis has already been used for particle identification with a diamond sensor [89, 90]. An effort has been made to implement an online and real time application for this analysis by porting the algorithms into an FPGA. This section first describes the device specifications. Then it describes in detail the PSA algorithms and the structure of the code. Afterwards it discusses the performance results, which showcase the limitations of the device. Finally it describes the data acquired with radioactive sources and in neutron reactors.

## 5.2 Requirements

Chapter 3 shows that the shape is heavily dependent on several factors, such as environmental temperature and received irradiation dose. Section 3.4 shows that at temperatures lower than 150 K the signal from an  $\alpha$  starts deteriorating due to recombination of charges in the charge cloud. Sensor irradiation, on the other hand, introduces charge traps, which change the signal pulse shapes, as shown in section 3.4.2. In addition, irradiated sensors have a reduced long-term stability during operation, as shown in section 3.3.2. These factors are a significant limitation for particle identification. Priming can improve the charge collection and longterm stability of the pulse shapes, as shown in section 3.3.2. To improve the measurement further, a high bias voltage has to be applied, increasing the measurement SNR.

Factor	Operating range
Sensor material	sCVD diamond
Sensor thickness	500 $\mu\text{m}$
Temperature	150 K – 400 K
Radiation dose	$< 1 \times 10^{13} \text{ neq cm}^{-2} \text{ s}^{-1}$
Bias voltage	$\sim 1 \text{ V } \mu\text{m}^{-1}$
Signal-to-noise	>5

Table 5.1: Limitations to particle identification.

## 5.3 Device specifications

The CIVIDEC ROSY readout system has been used for this task. It has a single BNC input with a  $50 \Omega$  or  $1 M\Omega$  termination and a DC or AC coupling. The analog chain has a 250 MHz bandwidth limit. The input range can be set from  $\pm 50 \text{ mV}$  up to  $\pm 5 \text{ V}$ . The signal offset can be set to any value within this range. The ADC samples the signal with an 8-bit precision at a rate of up to 5 GSPS. The PSA uses the highest sampling to achieve width measurement resolution of 0.2 ns. The amplitude resolution depends on the chosen input range, but at 256 ADC counts per sample, it can be as low as  $0.39 \text{ mV s}^{-1}$  at the range of  $\pm 50 \text{ mV}$  and as high as  $39 \text{ mV s}^{-1}$  at the range of  $\pm 5 \text{ V}$ .

The logic of the PSA is designed using VHDL and runs on a Xilinx Virtex 5 FPGA. The PSA is capable of a maximum counting rate of  $1.56 \times 10^8$  pulses per second, yielding a 6.4 ns double pulse resolution. The analysis is more time consuming; the maximum throughput rate of the pulse shape analysis is  $\sim 6 \times 10^6$  pulses per second. This means that after every pulse, the device has a dead time of approximately  $(200 \pm 15)$  ns, depending on the width of the pulse being analysed. Any pulse arriving during the analysis of the previous one is counted, but not analysed. Any two pulses with the distance between the rising edges lower than 6.4 ns are counted as a single pulse.

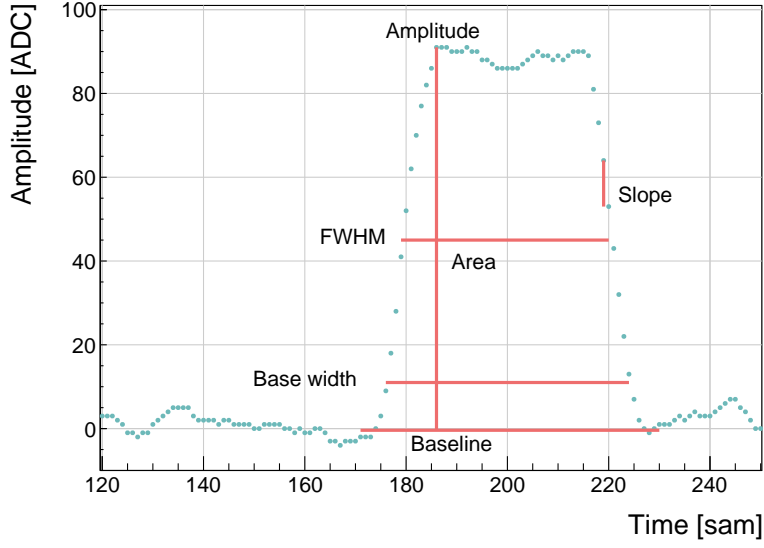


Figure 5.1: Pulse parametrisation: FWHM, area, amplitude, base width and falling slope.

The device is very sensitive to noise pick-up. Therefore the setup must be designed to minimise the pick-up by means of proper shielding, use of high-quality cables etc. The relatively low bandwidth limit filters out some high-frequency noise, but not the ringing or higher noise spikes. That is the task for the PSA.

## 5.4 Pulse parameters

A signal pulse on the input is parametrised during the analysis process. The PSA measures its amplitude, area, width at a defined pulse height, and the slope of its falling edge, as shown in figure 5.1. The amplitude is the difference between the baseline and the highest sample in the pulse and is given in ADC counts as an 8-bit value. The area is defined as the sum of amplitudes of all samples between two defined boundaries within the pulse. The width is defined as the number of samples with a value higher than a set amplitude threshold. If the threshold is at half the maximum amplitude, the resulting width is *full width at half maximum* (FWHM). The falling slope is the maximum negative difference between values of two samples and is given in ADC counts per sample.

The most important pulse parameter is the pulse area. It is directly proportional to the deposited charge of the particle and as such also proportional to the energy of the particle that is stopped in the sensor. The area distribution of a particle is therefore its energy spectrum. This is the target measurement for all radiation types. All subsequent parameters are shown as a function of the pulse area:

- FWHM [w, a]
- Base width [bw, a]
- Amplitude [A, a]
- Amplitude  $\times$  Base width [A  $\times$  bw, a]
- Base width-FWHM [bw-w, a]
- Falling slope [s, a]

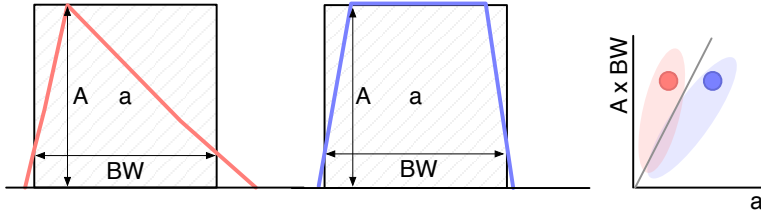


Figure 5.2: Form Factor. The black squares show the calculated area of the pulse. The calculated area is similar to the measured area for rectangular pulses, but not so much for triangular pulses. The red and blue dot in the right plot are the value entries of the two pulses shown. The red and blue oval shapes depict the regions for the values expected for triangular and rectangular pulses.

The Amplitude  $\times$  Base width qualifier is referred to as the *calculated area*. The ratio between the calculated area ( $a$ ) and the measured area ( $A \times BW$ ) is the *Form Factor* and is shown in figure 5.2. A Form Factor value of 1 means that the pulse shape is similar to a rectangle. A value of 2 means that the pulse has a triangular shape.

## 5.5 Description of the firmware

The application is built on top of the existing platform that handles the low-level connectivity with the hardware. It also provides the interface to the ADC data, the input/output registers and the USB data transfer. The PSA application has a set of modules that handle the data input and output and a module for signal analysis, as shown in figure 5.3. The data handling layer consists of the final state machine (FSM), the histogram builder, the raw signal handler, the USB FIFO buffer and the register array.

The firmware is written entirely in VHDL. The diagram in figure 5.3 shows the module architecture. The ADC provides the module with 32 digitised signal samples every clock cycle. The signal is routed directly to the pulse analyser and into the raw signal handler. The analyser outputs are connected to I/O registers and to histogram buffers. Both the histogram buffers and raw signal buffers are connected to the USB FIFO through a multiplexor. The firmware communication to the controller is done via input/output (I/O) registers (control and status registers, counters) and serially via USB (histogram data, waveforms).

### 5.5.1 Design constraints

**Speed** The ADC provides 32 8-bit samples on every 6.4 ns clock cycle. It is not possible to e.g. sum all 32 values in a single cycle, because the summation takes too long to complete. This is why the summation has to be pipelined and carried out in three cycles. This adds up to the analysis duration, which in turn decreases the maximum pulse rate.

**Firmware size** The PSA application makes use of a number of FIFO and RAM buffers to store the pulse waveforms and histograms. 48 32k block RAM modules have been used for the implementation, maxing out the available block RAM memory space on this FPGA. The analysis algorithm also takes up a significant portion of the FPGA fabric. Many of the operations are carried out on 256-bit long numbers received from the ADC, which quickly fills up the available logic. This is also why the place and route procedure takes a long time.

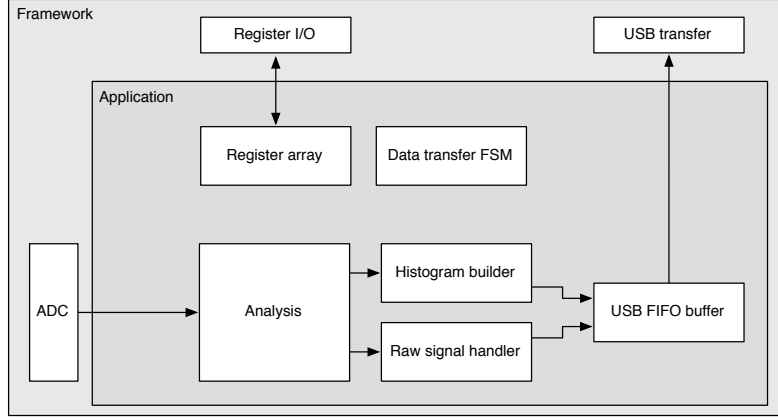


Figure 5.3: Firmware design structure.

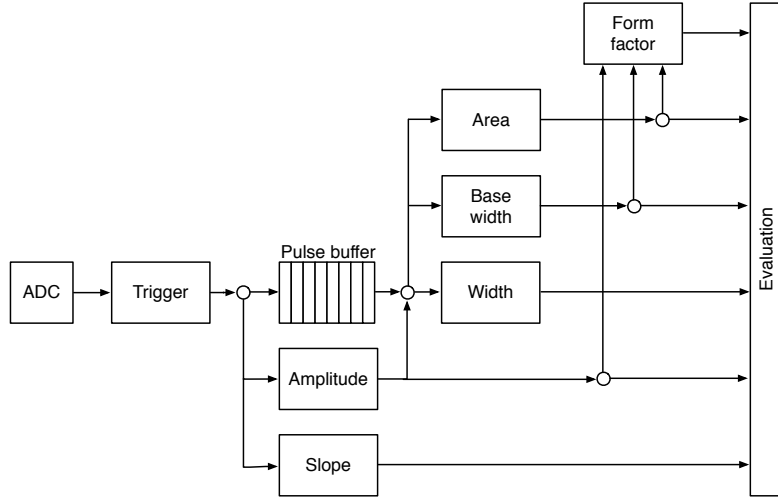


Figure 5.4: Code design plan.

**Power consumption** The reduction of the power consumption is not crucial for the intended applications.

### 5.5.2 Analysis module

This module is different for different applications. The Pulse Shape Analysis (PSA) application has the most complex module design. The spectroscopy application only uses a small part of that design and the Counter application an even smaller one.

The analysis (or parametrisation) is carried out in several steps, as shown in figure 5.4. The triggering block starts the readout upon signal threshold crossing. The maximum slope of the falling edge is observed. The Amplitude block calculates the pulse height and retains the maximum amplitude while pushing the signal into the pulse buffer. Then the entire pulse is clocked out of the buffer while its FWHM, baseline width and area are measured. Finally, the Form factor is calculated. At the end the Evaluation block takes in all the parametrised information and classifies the pulse according to user-defined cuts.

**Triggering** module handles signal polarity swapping, triggering on threshold and defining the trigger window. The real-time processing algorithm allows for a positive or an inverted input signal. However, the PSA only handles positive-polarity pulses. Therefore a negative signal is swapped in the *triggering* block. Signal analysis and readout are then triggered when the signal crosses a user-defined threshold. In addition, the signal has to be over the threshold for a defined number of samples. This is to avoid triggering on noise spikes. A double clock cycle delay is used on the signal to make sure that the recorded signal window includes the rising edge of the pulse as well as some baseline before it. A *trigger active* signal marks a window that contains the entire pulse including some baseline signal before and after it. The trigger can be vetoed by three signals: if the pulse analysis is still taking place, if the input signal exceeds the maximum voltage range or if the data transfer FSM is pausing the analysis due to data transfer to the controller.

**Amplitude** block calculates the pulse height as a difference between the pulse and the baseline. It also finds the position of the maximum amplitude within the clock cycle. It receives 32 8-bit samples from the triggering block every clock cycle. Time delays in the logic prevent it to find the maximum value of the 32 samples within one clock cycle. Therefore the decision logic has been pipelined in three stages, which means that the final maximum value is ready three clock cycles after the end of the pulse.

**Pulse buffer** is a FIFO buffer that stores the signal while its amplitude is being measured. At the end of the pulse the FIFO is read out so that the remaining measurements can take place.

**Width** block uses the maximum amplitude to determine the *half-maximum* and to measure the FWHM. To do so, it counts the samples that are above the half-maximum amplitude. However, this method might also count high enough noise spikes before or after the pulse. Hence an improved method, which “cleans” the measurement of unintentional additional noise, has been implemented. It is described in section 5.5.3.

**Baseline width** block is the same as the Width block, but it measures the width either at 50 %, 25 %, 12.5 % or 6.25 %, depending on the setting in the register. It also makes use of the special method described in 5.5.3 to avoid overestimations due to including noise in the measurement.

**Area** block measures the pulse area by summing up the amplitude values of the samples in the pulse. The boundaries of the summation are defined with the crossing of the amplitude above a certain threshold. Only the samples between those boundaries are summed up. The boundaries can be set at 50 %, 25 %, 12.5 % or 6.25 % of the maximum amplitude of the pulse. The area measurement makes use of the same routine as the FWHM and Baseline width block to remove the potential outlying samples.

**Falling slope** block measures the highest negative difference between amplitudes of two adjacent samples, thus getting the maximum negative slope of the pulse. It is an experimental routine, only used for academic purposes.

**Form factor** block is used as a special qualifier for particle identification. It compares the weighted measured area of the pulse with its weighted calculated “form”, which is defined as the multiplication of the measured amplitude and baseline width. The equation is as follows:

$$x \cdot a - y \cdot A \cdot BW \geq 0, \quad (5.1)$$

where  $a$  is the measured area,  $A$  is the amplitude,  $BW$  is the baseline width and  $x$  and  $y$  the user-defined weighting factors for the measured and calculated area. Typical values for these factors are 2 and 1, respectively. The output of the block is the boolean result of this equation.

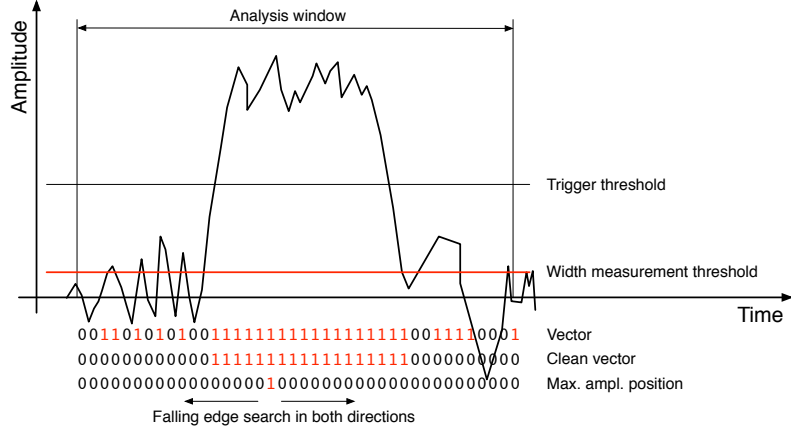


Figure 5.5: A sample pulse. The first vector shows which samples are above the width measurement threshold. The second vector is a clean vector. The third line shows the position of the maximum amplitude. The vector cleaning algorithm starts from the maximum amplitude and continues in both ways along the vector. From the first falling edge on it sets all bits to 0.

**Evaluation** block takes in all the parameters from the analysis blocks and compares them against the user-defined qualifiers. If the parameters are within the bounds, the pulse is accepted, otherwise it is rejected. The corresponding counters within the block are incremented.

### 5.5.3 Area and width measurement

The routine for measuring pulse area and width must have a specific algorithm implemented to carry out the measurements correctly. The core point is that the routine precisely defines the edges of a pulse. It does so by means of *vector cleaning*, presented in figure 5.5. An important input, beside the ADC data and the measurement threshold, is the position of the sample with the highest amplitude.

The signal arrives from the ADC as a set of 32 8-bit samples every every clock cycle with a period of 6.4 ns. All 32 samples are compared against the width measurement threshold. If a sample value is equal or higher than this threshold, a binary 1 is set in a 32-bit *vector* on the position corresponding to the position of the sample in the incoming ADC data set. The resulting vector might also include some noise at the edges of the pulse, depending on the height of the width measurement threshold. The old routine simply counts the binary ones in this vector to get the pulse width. This works well for measuring the FWHM because the threshold is high. However, for width measurements at 25 %, 12.5 % or 6.25 % of the pulse height this might already become a problem, because the noise might be counted in as well. This is why the new routine cleans the outliers in this vector before counting the remaining ones in the clean vector.

The routine starts from the position of the maximum height. It follows the vector in both ways and finds the first falling edge (0 at this position and 1 at the previous one). From there on it rewrites any binary 1 with a binary 0. The resulting clean vector only has one bunched set of binary ones which are summed, yielding a precise pulse width. The area measurement is similar - it only integrates over the samples marked in the clean vector. Both measurement routines, for area and for width, are implemented separately so that the area routine can have a different threshold set.

This section explains how the algorithm is designed. The idea for it was tested using Excel and was only afterwards ported to the VHDL. The underlying algorithm first cleans the vector. Then it passes the cleaned vector either to the width or area measurement, as shown in figures 5.6 and 5.7.

## 5.5. DESCRIPTION OF THE FIRMWARE

---

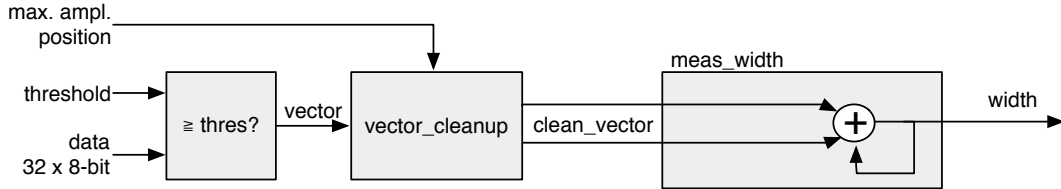


Figure 5.6: This block counts the remaining binary ones in the clean vectors and outputs this value as the pulse width.

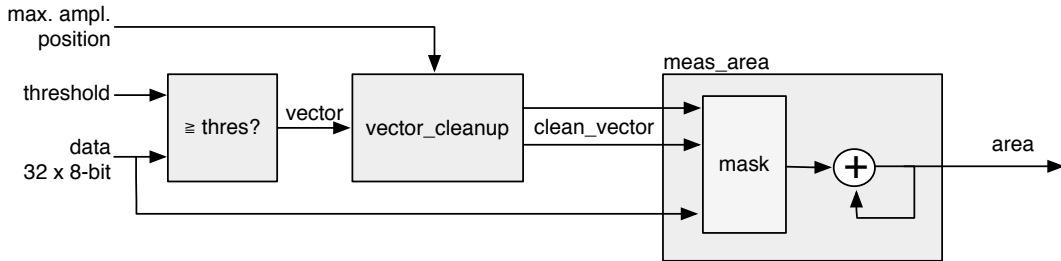


Figure 5.7: This block masks the input data with the clean vector and sums the remaining samples.

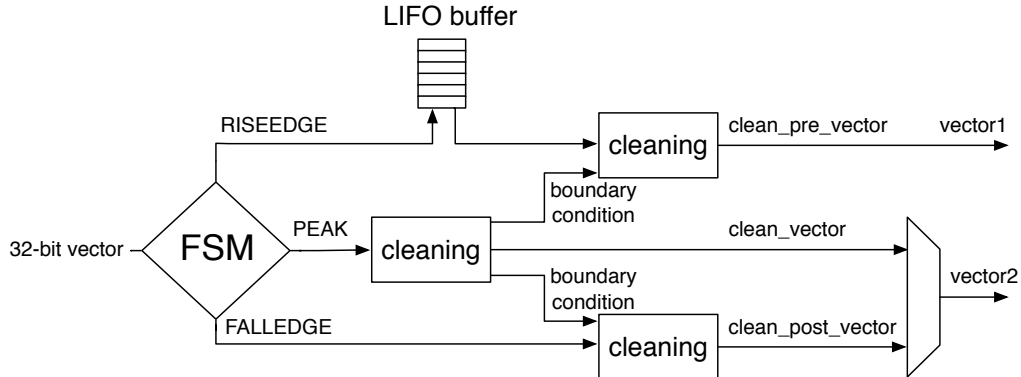


Figure 5.8: Vector cleaning routine outputs two vectors - one forward in time and one back in time starting from the peak of the pulse.

The width measurement module only sums the ones in the vector whereas the area measurement module sums the data samples marked by the cleaned vector. Both modules issue a *valid* signal when they finish the measurement.

### 5.5.3.1 Vector cleaning

This is the most important block. Its inputs are: *vector*, *parsing active*, *position of the max. amplitude (PA)* and *its delay (DA)*. PA is a 32-bit binary number that shows the position of the sample with the maximum amplitude within the data block (see figure 5.5) whereas the DA tells how many clock cycles after the start of the parsing this PA block is. The vector cleaning module is designed as a final state machine (FSM) with the states IDLE, RISEEDGE, PEAK, FALLEDGE and READY. The FSM is idle until it receives the *active* signal from the external module, marking

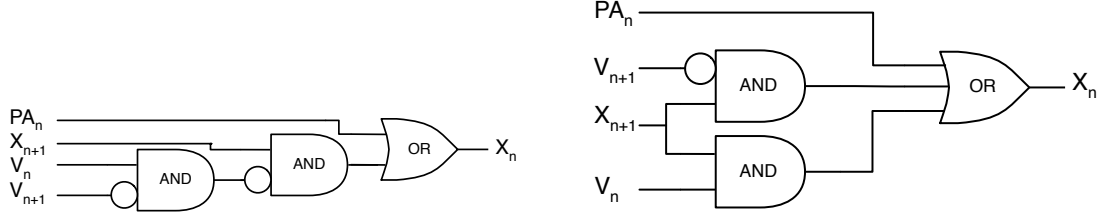


Figure 5.9: One logic step in the algorithm chain before and after Karnaugh minimisation.

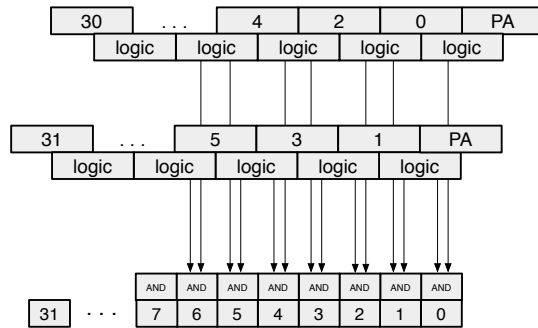


Figure 5.10: The vector is divided into two 16-bit logic chains. The algorithm logic is then run on the two chains separately. The results are then merged into one 32-bit clean vector by using a set of AND gates.

that the vector parsing has commenced. It switches to RISEEDGE, which starts two procedures: 1) it fills the vector of the pulse's rising edge into a last-in-first-out LIFO buffer (see figure 5.8) and 2) counts down from the DA value. When this counter reaches 0, the FSM changes its state to PEAK because the current vector on the input is the one containing the maximum amplitude. This data block is sent through the *peak algorithm*, which cleans the vector. The FSM switches to FALLEDGE state. Now both the previously buffered vector of the rising edge and current vector of the falling edge go through the *pre- and post- algorithm* where they are cleaned, but they get their boundary conditions from the *peak algorithm*. The output of this module is therefore two cleaned vectors in parallel – one forward in time and the other backwards.

### 5.5.3.2 Algorithm

The underlying algorithm is sequential - it carries out a logic operation shown in figure 5.9 on vector bit on position 0, uses the output of this operation for the operation on bit on position 1 and so on. This means that it has to carry out 32 logic operations per clock cycle. With each operation taking approximately 0.3 ns, the entire logic chain takes approximately 10 ns to complete. With only 6.4 ns per clock cycle, this means timing errors would occur. To fix the problem, a more complicated *decimated algorithm* has been designed. It consists of two parallel logic chains. Each of the two only takes every second bit into account (Chain one: 0, 2, 4 ..., 30. Chain two: 1, 3, 5 ..., 31). This makes the chains effectively 16 bits long. The algorithm is run on the two chains and the results are merged together at the end as shown in figure 5.10. This effectively reduces the number of sequential logic operations to 18, which is within the timing constraints.

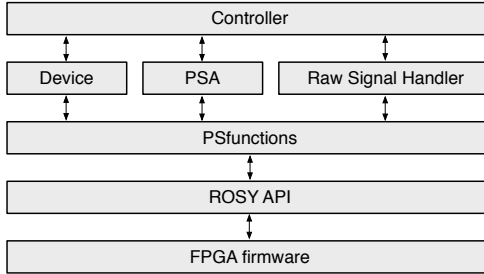


Figure 5.11: Abstraction levels of the controller software.

## 5.6 Control and data interface

Communication between the device and the controller PC is done via the API functions provided by the producer. In addition, the API used by CIVIDEC has access to several extra functions. These allow the user to download a customised bitfile to the FPGA, access the I/O registers and use the USB data transfer.

### 5.6.1 Software

The software has been designed in C++ in several levels of abstraction. Figure 5.11 shows the structure of the classes. The classes Device, PSA and RawSignalHandler are there to make it easier to read and understand the controller code. In principle the PSfunctions can also be accessed directly by the controller, but for this the instruction sequences must be well known and understood.

### 5.6.2 Data readout

The device records the data in two forms - as signal waveforms and as histograms of analysed pulse parameters. Both are available upon request from the controller. Only one of the two can be transferred via the USB line at a time.

The waveforms are saved into a FIFO buffer, which can hold up to 64 pulses of the length of  $\sim 500$  samples. The data format for each pulse is such that it starts with a header containing the pulse timestamp and the sequential number, continues with the data samples and ends with a header containing all the measured parameters (width, amplitude, area, falling slope and form factor). When the FIFO is full, it issues a flag, which tells the controller that the data buffer is ready for readout.

The histograms are implemented into the FPGA's Block RAM. Their sizes range from 256 to 4'096 bins (8-bit to 12-bit histograms, respectively), depending on the required histogram resolution. For instance, the width parameter is measured with a 0.2 ns resolution and the expected maximum pulse width is less than 20 ns. This yields the maximum range of 100 bins, making an 8-bit histogram sufficiently large. The amplitude histogram range is defined by the 8-bit resolution of the ADC. The area measurement, however, yields higher values and can therefore have a more refined 12-bit binning. Finally, a single 12-bit 2D histogram is included, with six bits for every axis. It is used as an online scatter plot for comparing two measured parameters. An example for it is a comparison of the width against the area, which can help the user determine the cuts that need to be applied to the measurement. All implemented 2-D plots are shown in section 5.8.

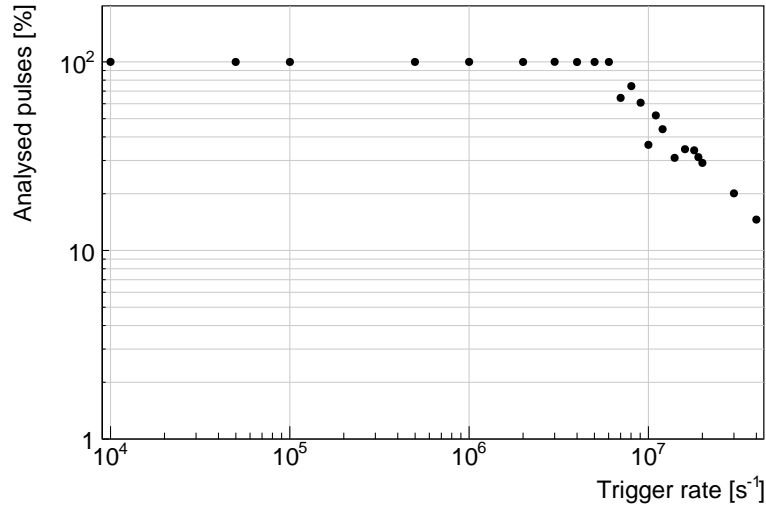


Figure 5.12: This figure shows the capability of the device to analyse all arriving pulses for a range of input frequencies. The highest achievable rate with zero lost pulses is  $6 \times 10^6 \text{ s}^{-1}$ .

## 5.7 Performance results

The PSA was tested in the laboratory first using a pulse generator and then with a radioactive sources. This section contains the results of the performance tests.

### 5.7.1 Tests with a pulse generator

#### 5.7.1.1 Trigger rate

A pulse generator was used to verify the highest achievable rate at which the PSA still analyses every incoming pulse. The final state machine implemented in the pulse analysis module prevents the triggering block from issuing a trigger due to an incoming pulse if the previous analysis is still ongoing. Given that all the pulses have the same length, the analysis duration must always be the same. When the time between the incoming pulses is shorter than the time of the analysis, the pulses are not analysed. Figure 5.12 shows the sharp decline in the percentage of the analysed pulses when reaching the rate of 6 MHz. Therefore the overall analysis duration for a 10 ns pulse is approximately 200 ns.

#### 5.7.1.2 Linearity

A pulse generator was used to verify the linearity of the measurements across all input ranges. The pulse width and the amplitude were varied and measured both with the oscilloscope and the PSA to estimate the systematic error of the PSA measurements with respect to those taken by the oscilloscope. The results are shown in figures 5.13a and 5.13b. The measured amplitude error  $e_{\text{ampl}}$  is within  $\pm 3\%$  of the real value throughout the amplitude range. The width error  $e_{\text{width}}$ , however, increases significantly in the lower width range. This stems from the low bandwidth limit of the PSA, which affects the pulse shape via a slow rising and falling time, effectively smearing the pulse along the time axis. Therefore the PSA cannot measure rectangular pulses shorter than 2 ns.

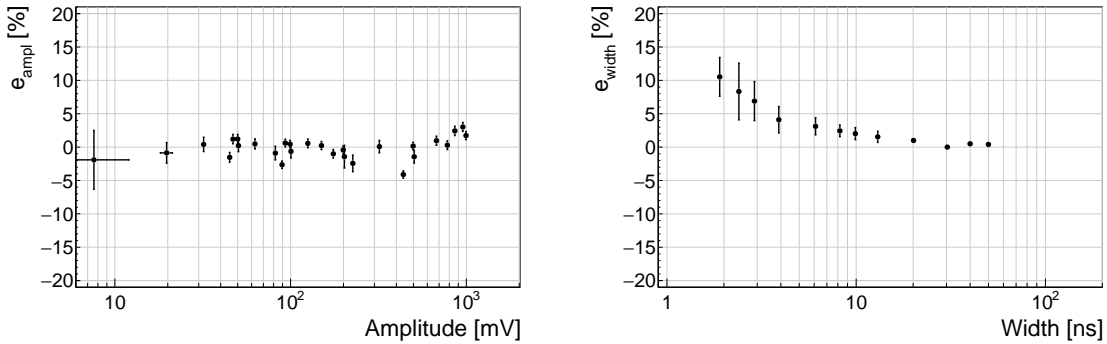


Figure 5.13: These figures show the measurement errors for amplitude (left) and width (right) across the measurement range.

#### 5.7.1.3 Stability

The input pulse signal was superimposed with the white noise generated by a CIVIDEC noise generator with a variable attenuation. The mixed signal yielded pulses with an SNR ranging from 5 (very noisy) to 100 (noise negligible). The PSA then performed the pulse parametrisation at different SNRs without changing the pulse shape. The results of the measurement errors for amplitude, width and area are shown in figures 5.14a, 5.14b and 5.14c. The amplitude is highly overestimated at a low SNR (high noise). This is because the algorithm takes the peak of the signal as the maximum amplitude and these peaks are higher with a higher noise. Therefore the  $e_{\text{ampl}}$  is always positive and increasing with increasing noise. The width measurement, on the other hand, is stable even for the low SNR. The  $e_{\text{width}}$  does not exceed  $\pm 5\%$ . Finally, the mean of the area measurement error  $e_{\text{area}}$  is always 0, but the spread of the error increases with noise. This means that the increased noise only affects the resolution of the measured area spectrum, not its position.

#### 5.7.1.4 Conclusion

The results show that: 1) the amplitude, area and width measurement are linear for pulses at least 2 ns wide, 2) the highest rate of the PSA algorithm is  $\sim 6 \times 10^6$  pulses per second and 3) the lowest SNR where the algorithm still functions is  $\sim 5$ , but the area measurement spread at that SNR is significant.

### 5.7.2 Comparison between the charge-sensitive and current spectroscopy

The calibration was done using a quadruple- $\alpha$  source containing  $^{148}\text{Gd}$ ,  $^{239}\text{Pu}$ ,  $^{241}\text{Am}$  and  $^{244}\text{Cm}$ . Each of the radioactive elements emits  $\alpha$  particles with a specific energy: 3.2 MeV, 5.2 MeV, 5.5 MeV and 5.8 MeV. The PSA in combination with the CIVIDEC C2 current amplifier was compared against an 8-bit spectroscopic application in combination with the CIVIDEC Cx spectroscopy amplifier.

Figure 5.15 shows the energy spectrum acquired by the two amplifiers. The  $^{241}\text{Am}$  peak measured by the CIVIDEC Cx amplifier has an RMS of 0.8 ADC, which corresponds to a 32 keV energy resolution. For comparison, the CIVIDEC C2 broadband current amplifier measures this peak with an RMS of 1.9 ADC, which corresponds to a 75 keV energy resolution. Therefore the energy spectrum measured by the current amplifier has a factor of 2.3 lower energy resolution.

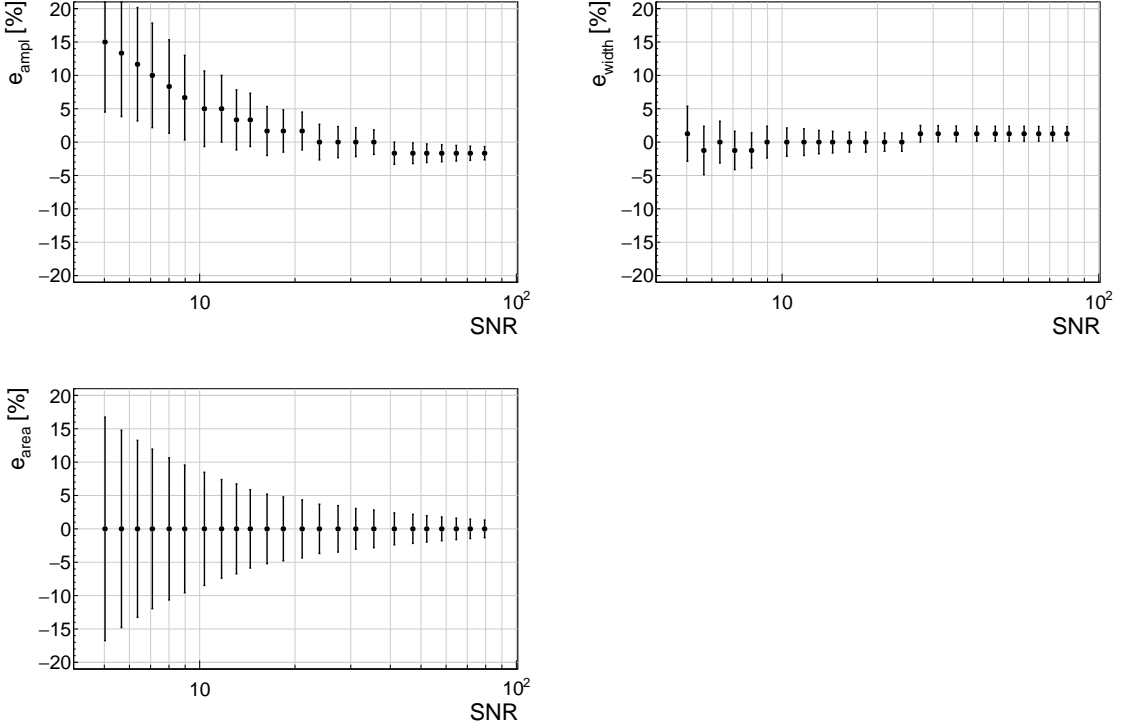


Figure 5.14: These figures show the measurements errors for amplitude (top left), width (top right) and area (bottom left) as a function of the signal-to-noise ratio.

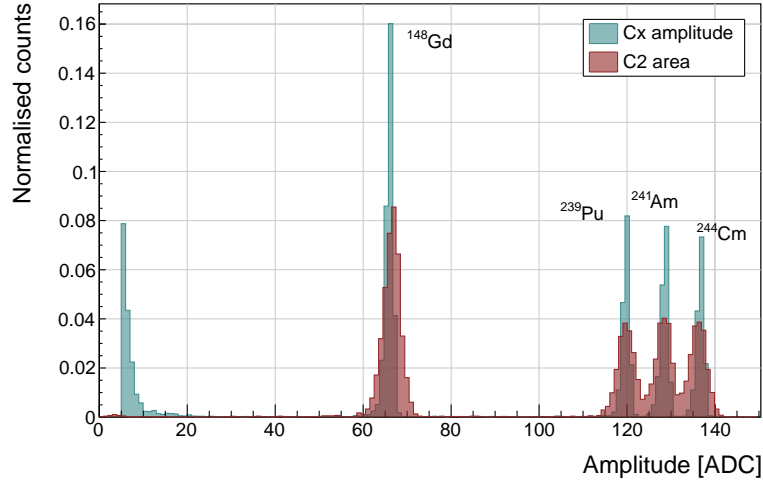


Figure 5.15: Energy spectrum of a quadruple- $\alpha$  source using a CIVIDEC Cx spectroscopic amplifier and a CIVIDEC C2 current amplifier. The peak on the left part of the Cx distribution is attributed to the  $\gamma$  background.

## 5.8 Source calibration

### 5.8.1 Pulse classification

Pulses induced by a specific radiation type have a specific pulse shape and therefore similar parameters. This section outlines the parameter space for several types of radiation. Table 5.2 lists the

## 5.8. SOURCE CALIBRATION

---

types of radiation and their respective pulse shapes. The types have been sorted into classes for easier discussion. The table includes the radioactive sources that emit these particles.

Class	Particle type	Current signal	Source
A	$\alpha$	Square pulse, h <sup>-</sup> drift	$^{241}\text{Am}$
B	$\alpha$	Square pulse, e <sup>-</sup> drift	$^{241}\text{Am}$
C	$\beta$	Triangular pulse	$^{90}\text{Sr}$
D	$\gamma$	Triangular pulse	$^{60}\text{Co}$
E	n	Mixed pulse shapes	$^{239}\text{Pu}$
F	p	Mixed pulse shapes	$^{239}\text{Pu}$

Table 5.2: Current pulse classification.

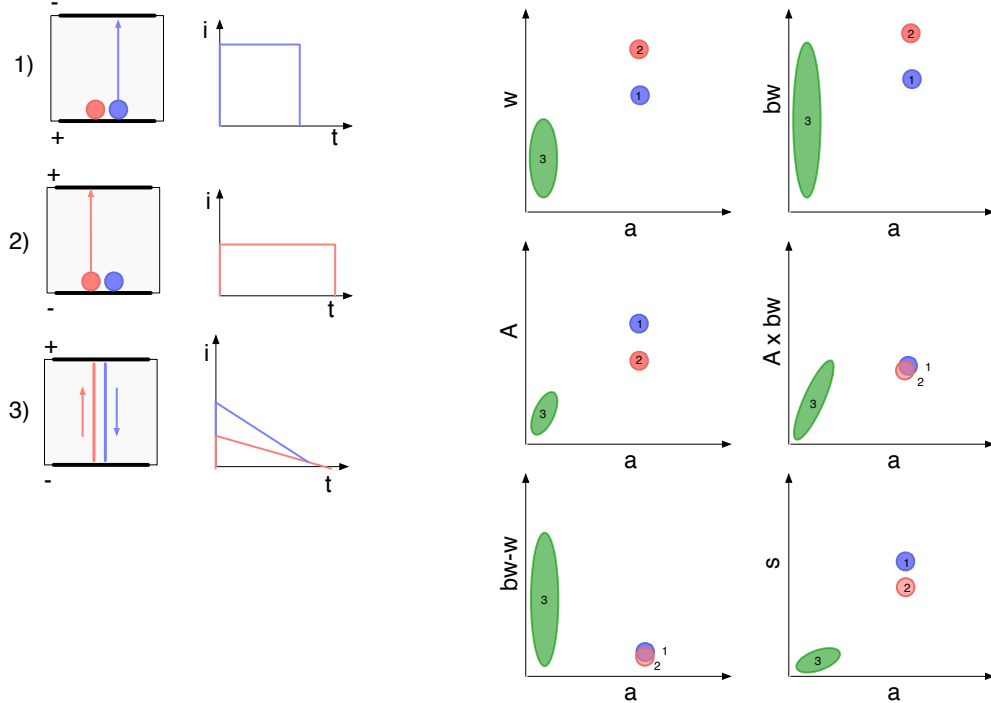


Figure 5.16: Class A, B, C, D.

### **5.8.1.1 Class A, B, C, D**

An  $\alpha$  particle deposits all its energy at the point of entry in the sensor. Depending on the polarity of the sensor bias voltage, either holes or electrons drift through the sensor, inducing a rectangular current pulse.

Schematic 1) in figure 5.16 shows the positive charge carriers drifting through the sensor and the current pulse they induce – Class A. Holes produce a short and high rectangular pulse. The parametric “fingerprint” of these current pulses is shown on the right side of figure 5.16, marked with number 1. All  $\alpha$  particles deposit the same amount of charge. The width and the base width are always the same as the drift velocity of the charge carriers does not change regardless of the number of carriers drifting. The base value is slightly higher due to the rise and fall time of the current signal. The amplitude is the same for all pulses. The same goes for the calculated area (a product of the amplitude and base value). For an ideal pulse, the coefficient between the measured area and the calculated area for a rectangular pulse is 1. The difference between the base width and the width is close to 0 and depends on the rise and fall time of the current signal defined by the electronics. The falling slope of the signal depends on the amplitude of the signal, therefore it is constant for a nominal pulse.

Schematic 2) in figure 5.16 shows the negative charge carriers drifting through the sensor and the current pulse they induce – Class B. Electrons produce a wide and low rectangular pulse. Parametrically Class B differs from Class A in the width, base width, amplitude and slope. The former two are higher due to a lower drift velocity of electrons. The amplitude is proportionally higher to preserve the constant pulse area due to a constant deposited charge.

Schematic 3) in figure 5.16 shows the configuration of the deposited charge created by an incident  $\beta$  particle – Class C. The positive and negative charge carriers induce a triangular pulse while drifting to their respective electrodes. The number of electrons and holes created differs from pulse to pulse, but follows a Landau distribution, as discussed in previous chapters. The amplitude of the pulse is linearly dependent on the initial number of created carriers, but has a higher coefficient than that of Class A or B. The same goes for the width and base width. The width of the pulses is lower than that of Class A and B. The base width, however, can already be close to Class A and B for the widest Class C pulses. The coefficient between the measured and calculated area is close to 2. The difference between the base width and width is a wide distribution. The falling slope is a low value for triangular pulses of all amplitudes.

$\gamma$  particles interact with the diamond mostly via the photoelectric effect and via Compton scattering, exciting an electron, which in turn ionises the sensor. Therefore the predicted pulse shape – Class D – will be similar to that of  $\beta$  particles – Class C.

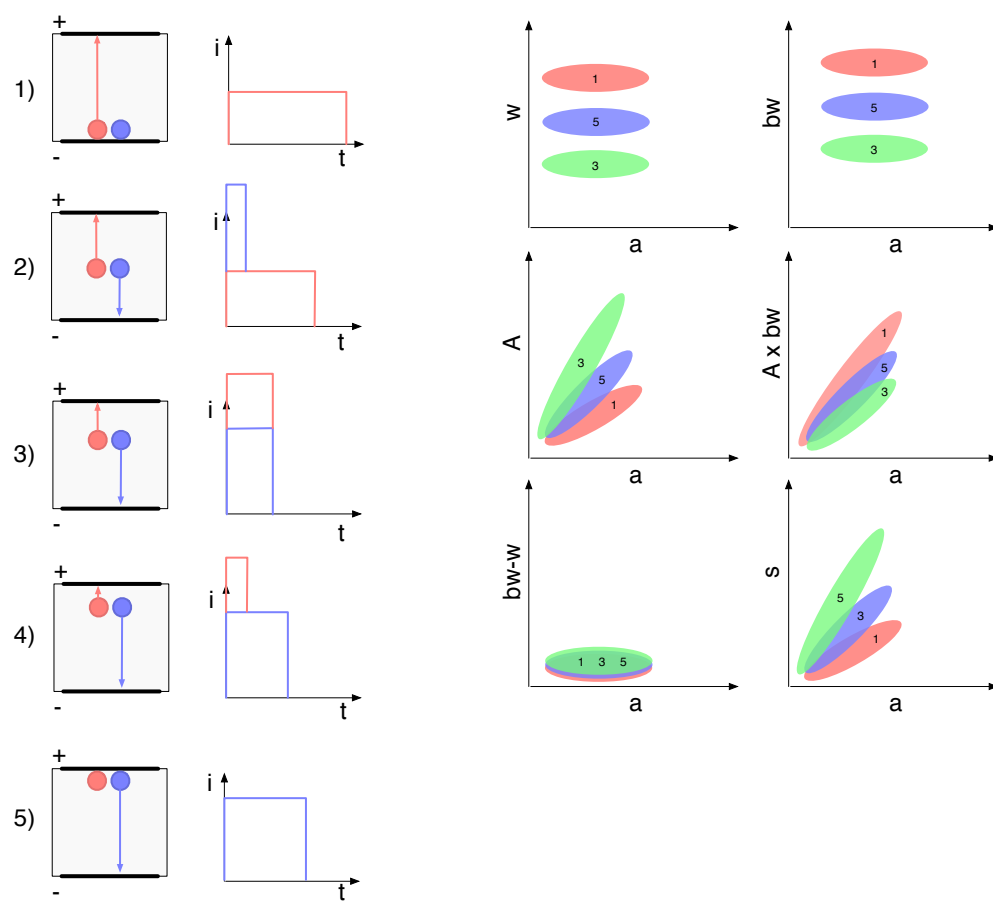


Figure 5.17: Class E.

### **5.8.1.2 Class E**

Neutrons interact with the core of the carbon atoms, producing a range of particles ranging from  $\gamma$ ,  $\beta$  and  $\alpha$  to protons. Neutrons are therefore a source of Class A, B, C, D, E and F pulses. Class E is a special case whereby  $\alpha$  particles are created at various points throughout the sensor. These particles immediately deposit all their energy and the created electrons and holes that drift to their respective electrodes induce a pulse with a specific shape. Schematics in figure 5.17 show examples of an  $\alpha$  creation in the sensor at five depths.

Schematics 1) and 5) are equal to Class B and A type. The difference here is that the created  $\alpha$  particles have a range of energies and therefore the deposited charge has a wide range. Their parametric fingerprint is similar to that of Class A and B, but is now spread over a wide range. The width and base width are equal across the measured range, the same holds for the difference between base width and width. The amplitude for both 1 and 5 increases linearly with the area.

Schematic 2) shows a carrier creation in the middle of the sensor and its respective current pulse. The holes drift faster and reach their respective electrode before the electrons reach the opposite side. The resulting pulse has a high peak at the start where both charges contribute to the signal and a long rectangular tail pertaining to the electron drift. Schematic 4) is similar to 2), with a difference that in this case the electrons contribute to the initial peak. These two cases are not shown in the parameter space.

Schematic 3) shows a special case in which the created electrons and holes reach their respective electrodes at the same time. This results in a short and high rectangular shaped current pulse. It is narrower than 1) and 5). Its amplitude increase as a function of the area is faster than for the other two. The same goes for the slope. Inversely, the calculated area increase as a function of the area is slower due to a narrower base width.

In summary, Class E pulses stem from neutron interactions at the electrodes or in the bulk, forming three distinct lines.

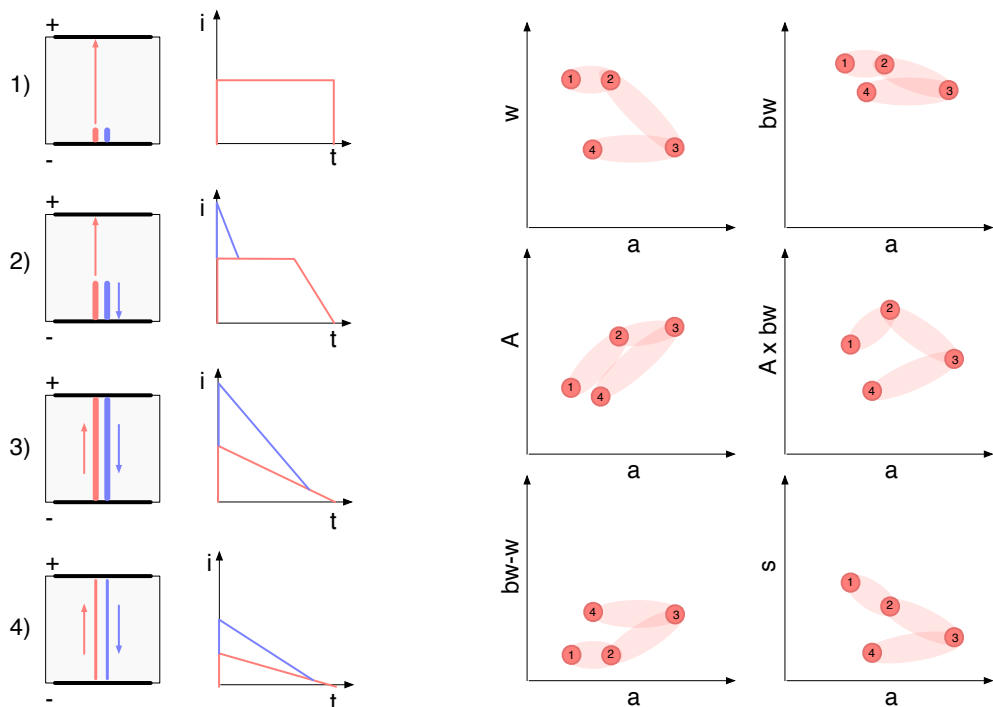


Figure 5.18: Class F. Red points in the graphs marked 1, 2, 3 and 4 correspond to example pulses on the left.

### 5.8.1.3 Class F

Protons can produce a range of pulse shapes, depending on their energy. High-energy MIPs fly through the sensor and produce a triangular pulse equal to that of  $\beta$ . Those with a low energy get stopped in the sensor, inducing a pulse with a complex shape. Class F comprises protons created by a neutron interaction with a carbon atom, referred to as recoil protons. For reasons of clarity the examples shown below stem from a neutron interaction at the negatively charged electrode. In addition, the direction of the recoil proton is always in the direction of the opposite electrode.

Schematic 1) shows a creation of a low-energy recoil proton. It deposits all its energy within a few  $\mu\text{m}$ , inducing a Class B rectangular pulse. It also resembles the Class B in the parameter space.

Schematic 2) shows a proton that travels for a third of the sensor width before being stopped. The trace it leaves induces a pulse with an initial peak due to the contribution of the drifting holes and a gentle falling edge at the end. Its width and base width are still close to the nominal value. The amplitude is significantly higher due to the initial peak. As a consequence, the calculated area is higher as well. The difference between the base width and width is still nominal. The slope value decreases due to a less pronounced falling edge of the pulse.

Schematic 3) shows a corner case whereby the recoil proton is stopped at the opposite electrode. It induces a high triangular pulse. Its width is significantly lower due to the high amplitude. The base width, however, remains almost the same. Therefore the difference between the base width and width increases. The slope continues decreasing.

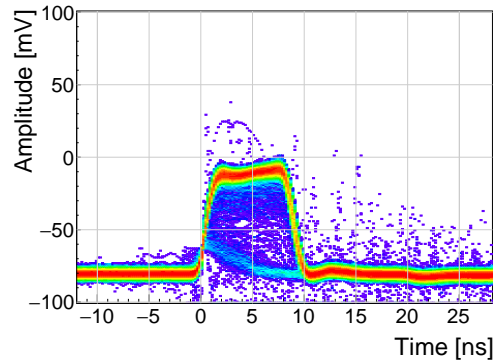
Schematic 4) shows a high-energy recoil proton that exits the sensor with a high velocity. According to the Bethe-Bloch such a highly energetic particle deposits less charge than that with a low energy. The resulting current pulse therefore has a lower amplitude while preserving the width. Its slope is also lower due to the lower amplitude.

### 5.8.2 Data acquisition

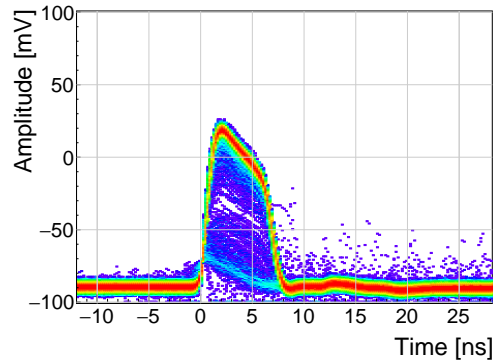
The operation of the pulse shape analysis has been tested using several radioactive sources. In particular, an  $\alpha$ , a  $\beta$  and a  $\gamma$  source have been used. Each source has been placed on top of the diamond detector and left for a predefined time depending on its activity. Table 2.1 shows the sources used, the time of exposure and their rate during data acquisition. The data for the  $\alpha$  source have been taken for both polarities.

Run	Source	Radiation	Energy [MeV]	Time [h]	Triggers	Rate [ $\text{s}^{-1}$ ]	Bias [V]
1	$^{241}\text{Am}$	$\alpha$	5.5	17	10558	0.17	500
2	$^{241}\text{Am}$	$\alpha$	5.5	18	11454	0.18	-500
3	$^{90}\text{Sr}$	$\beta$	2.3	0.42	1.07e6	1'000	500
4	$^{60}\text{Co}$	$\gamma$	1.3	0.28	1.34e6	3'300	500
5	$^{239}\text{Pu Be}$	$n$	1-10	2.5	1.5e6	230	500

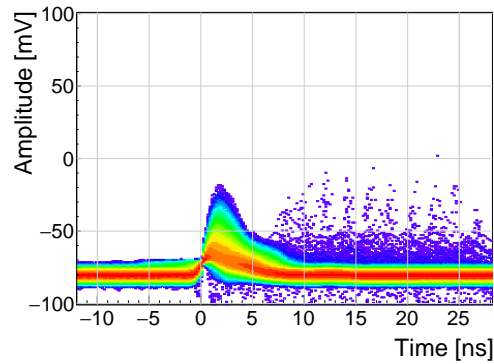
Table 5.3: Measurements carried out at Atominstutitut.



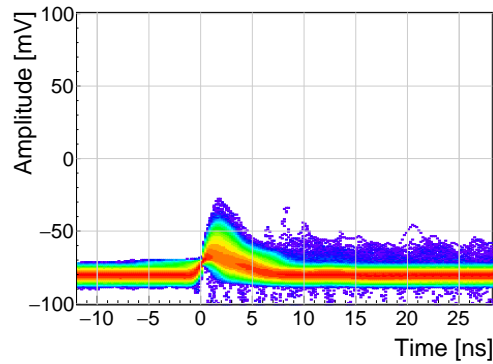
(a)  $^{241}\text{Am}$ ,  $e^-$  collection.



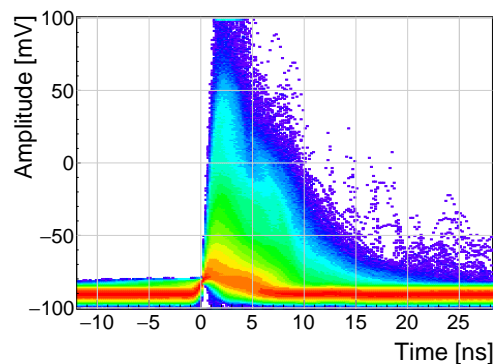
(b)  $^{241}\text{Am}$ ,  $h^+$  collection.



(c)  $^{90}\text{Sr}$ .



(d)  $^{60}\text{Co}$ .



(e)  $^{239}\text{Pu}$  Be.

Figure 5.19: Accumulated current pulses for all runs.

Figure 5.19 shows five sets of data acquired by a non-irradiated diamond sensor. The measurements were carried out in the following order: a), c), d), e), b).

Figure 5.19a shows a set of current pulses induced by the  $\alpha$  particles whereby only the electrons drift through the sensor. The great majority of particles creates a defined number of charge carriers. According to the FWHM of the pulse, the electrons drift for 9 ns before reaching the opposite electrode. The pulse amplitude is stable during the drift, with a gentle positive inclination. This hints on a weak negative space-charge built up across the sensor. Some pulses have a lower amplitude while retaining the width; the smaller pulse area means that there are fewer drifting charge carriers than a nominal value. This shows that some incident  $\alpha$  already lose a part of their energy while traveling through the air before hitting the sensor. Furthermore, there is a number of low-amplitude triangular pulses which are created by incident  $\gamma$  particles. Finally, the scarce entries above the baseline after the pulse stem from interference pulses.

Figure 5.19b also shows the  $\alpha$ -induced current signals, but for the hole collection. The number of holes created is equal to the number of created electrons, therefore the collected charge is the same for both. This means that the area of the current pulse is equal to that in figure 5.19a. The pulses are only 6 ns wide, which confirms that hole mobility in diamond is  $\sim 30\%$  higher than that of electrons at room temperature. Therefore the current pulse must be higher to preserve the area. The pulses have a steep negative droop. This is due to a strong negative space-charge built up during preceding measurements with a neutron source. Furthermore, some pulses induced by a lower energy  $\alpha$  have a lower amplitude and hence a lower pulse area. Finally, the  $\gamma$ -created triangular pulses are still present.

Figure 5.19c shows the triangular pulses created by the incident  $\beta$  particles. Most have a low amplitude that is close to the trigger threshold (red coloured line). Those below the threshold are not visible by the PSA. The entries behind the pulses are either interference pulses or  $\beta$  pulses following the first pulse.

Figure 5.19d shows the triangular pulses created by the incident  $\gamma$  particles. The distribution is very similar to that created by the incident electrons in figure 5.19c. This is expected –  $\gamma$  particles interact with the sensor via compton scattering, freeing an electron which in turn ionises the sensor. Therefore the resulting current pulses of an incident  $\gamma$  are similar to those of an incident  $\beta$ .

Figure 5.19e shows that the neutron source causes the widest variety of pulse shapes - triangular and rectangular as well as those in between. This stems from the various interactions of neutron with carbon atoms, whereby  $\alpha$ ,  $\beta$ ,  $\gamma$  or protons can be produced. The prevailing pulses are still those created by  $\gamma$ . Pulse shapes caused by neutrons are described in detail in [91, 92].

### 5.8.3 Scatter plots

The parameters of the pulses are plotted in 2D histograms - in form of scatter plots. The energy spectrum is directly proportional to the measured area of the current pulses, therefore all the parameters are plotted as a function of the pulse area. Every individual parameter can be attributed a set of qualifiers with which a certain part of the distribution can be rejected. There are two ways to apply the qualifiers. One is to set the minimum and maximum value for a specific parameter. The accepted pulses are those in between these two values. The minimum and the maximum qualifier are marked with a blue and a red line in the scatter plots. The second way is to apply a linear cut to the distribution in the scatter plot. The user can choose the slope of the line and to accept either the pulses above or below the line. The line is blue if the part above the line is accepted and red if opposite. Currently two scatter plots have this option implemented: area vs amplitude and area vs amplitude  $\times$  base width. The latter represents the Form Factor, which is discussed in section 5.5.2.

## 5.8. SOURCE CALIBRATION

---

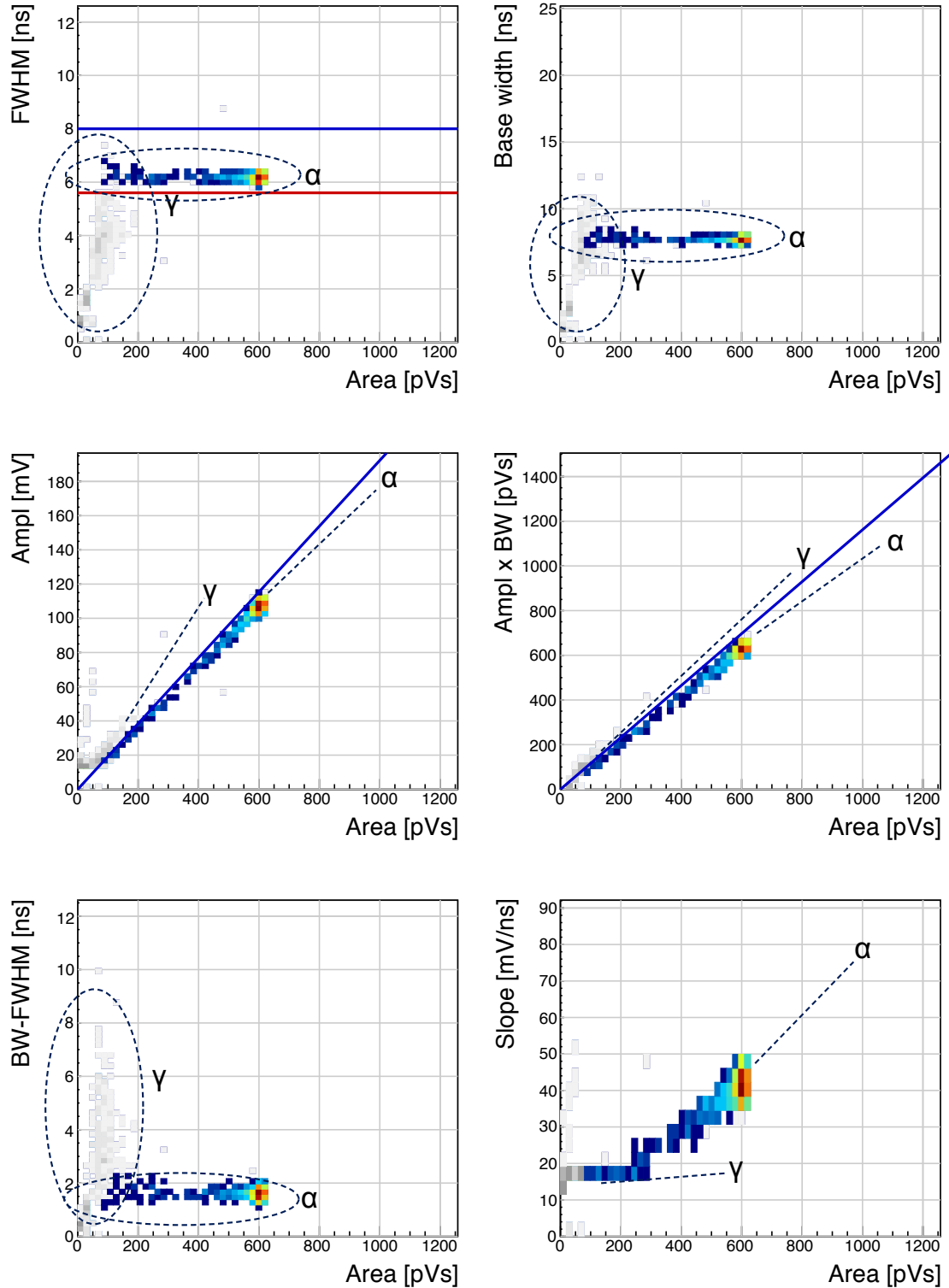


Figure 5.20:  $^{241}\text{Am}$ ,  $\text{h}^+$  collection. Qualifiers: FWHM, amplitude, calculated area.

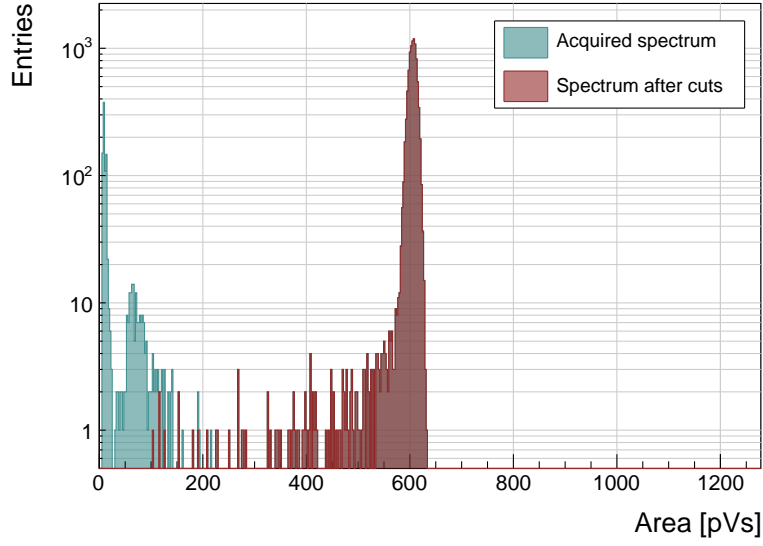


Figure 5.21:  $^{241}\text{Am}$  area histograms for hole collection. The green histogram represents all collected data whereas the red one marks the data whereby the pulse parameters are within the qualifiers. The  $\alpha$  peak at 600 pVs is clearly visible, followed by a  $\gamma$  quasi-Landau distribution with an MPV of  $\sim 70$  pVs and a noise peak at the very left of the area distribution.

#### 5.8.3.1 $^{241}\text{Am}$ source, $\text{h}^+$ collection

The source emits  $\alpha$  particles at  $\sim 5.5$  MeV and 60 keV  $\gamma$  photons. Due to the losses in the air and in the electrode the measured  $\alpha$  energy varies – between  $\sim 5$  MeV down to 1 MeV. Figure 5.20 shows the parameter space of the acquired data for hole collection - Class A . Width, amplitude and calculated area qualifiers have been used to identify the  $\alpha$  pulses and reject the  $\gamma$ . Figure 5.21 shows a one-dimensional area distribution of the acquired data. The MPV of the  $\gamma$  distribution is not at the expected position (30 pVs, which is approximately a factor of 20 lower than the  $\alpha$  peak). This is due to two factors: increased non-linearity in area measurement at the lower range as shown in figure 5.13 and the fact that the threshold for self-triggering cuts the majority of the Landau distribution due to the low amplitude of the pulses. The effect is also observed in  $\gamma$  source measurements in section 5.8.3.4.

**Width:** A distinct horizontal line at 6.5 ns starting from 100 and peaking at 600 pVs shows the aforementioned spread of  $\alpha$  energies. The width of the pulse remains constant.  $\gamma$  cluster overlaps with the  $\alpha$  cluster at low energies. Width qualifier is used.

**Base width:** Wider than the FWHM, yet still constant over the range. High overlap with  $\gamma$ .

**Amplitude:** Linear increase with area. The coefficient for  $\alpha$  pulses is lower than that for  $\gamma$ . Amplitude qualifier is used.

**Calculated area:** Barely distinguishable difference in slope coefficients for  $\alpha$  and  $\gamma$ . Calculated area qualifier is used.

**Base width – width:** Minimal difference for  $\alpha$ , high spread for  $\gamma$  as expected. At low  $\gamma$  area the overlap is high, so the qualifier cannot be used.

**Slope:** Linear increase with the area. Significant overlap in the low area range. A line of entries with a high slope at low area pertains to short noise pulses with a high spike.

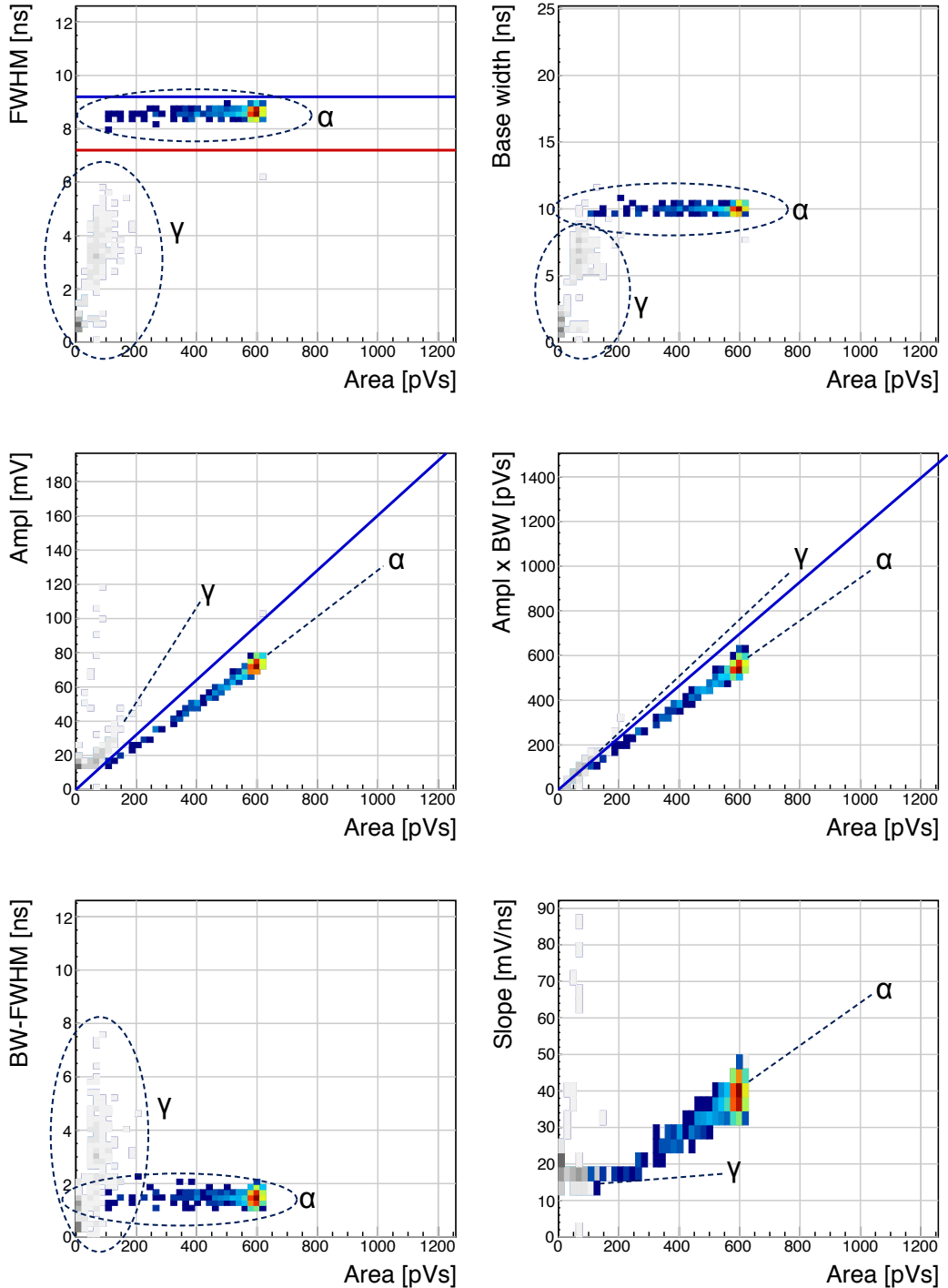


Figure 5.22:  $^{241}\text{Am}$ ,  $e^-$  collection. Qualifiers: FWHM, amplitude, calculated area.

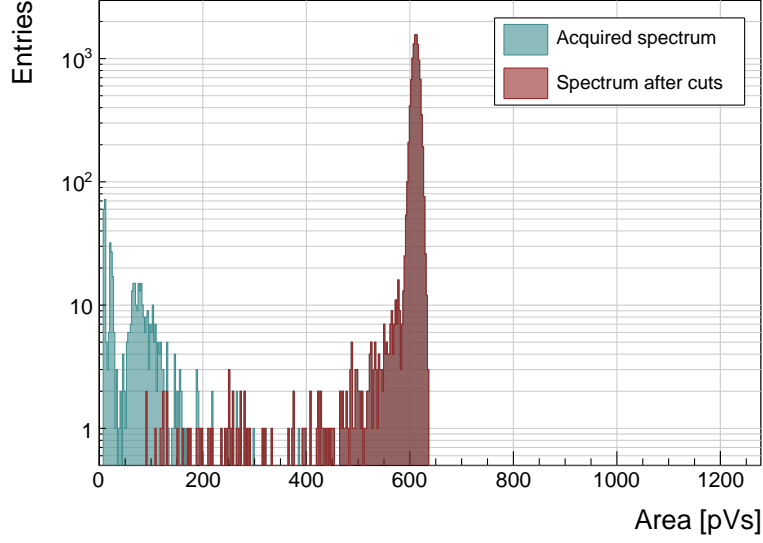


Figure 5.23:  $^{241}\text{Am}$  area histograms for electron collection. The green histogram represents all collected data whereas the red one marks the data whereby the pulse parameters are within the qualifiers. The  $\alpha$  peak at 600 pVs is clearly visible, followed by a  $\gamma$  quasi-Landau distribution with an MPV of  $\sim 70$  pVs and a noise peak at the very left of the area distribution. These two contributions have been rejected by the qualifiers.

#### 5.8.3.2 $^{241}\text{Am}$ source, $e^-$ collection

Figure 5.22 shows the parameter space of the acquired data for electron collection - Class B. Width, amplitude and calculated area qualifiers have been used to identify the  $\alpha$  pulses and reject the  $\gamma$ . Figure 5.23 shows a one-dimensional area distribution of the acquired data. The  $\gamma$  MPV of 70 pVs is not as expected (30 pVs); the reason for the shift is discussed in section 5.8.3.1.

**Width:** A distinct horizontal line at 8.5 ns starting from 100 and peaking at 600 pVs shows the spread of  $\alpha$  energies. The width of the pulse remains constant.  $\gamma$  cluster does not overlap with the  $\alpha$  cluster at low energies as none of the  $\gamma$  pulses are as wide as the  $\alpha$ . Width qualifier is used.

**Base width:** Wider than the FWHM, yet still constant over the entire range. Small overlap with  $\gamma$ .

**Amplitude:** Linear increase with area. The coefficient for  $\alpha$  pulses is significantly lower than that for  $\gamma$ , also lower than that for hole collection. Amplitude qualifier is used.

**Calculated area:** Distinguishable difference in slope coefficients for  $\alpha$  and  $\gamma$ . Calculated area qualifier is used.

**Base width – width:** Minimal difference for  $\alpha$ , high spread for  $\gamma$  as expected. At low  $\gamma$  area the overlap is low, but due to low statistics.

**Slope:** Linear increase with the area. Overlap in the low area range. A line of entries with a high slope at low area pertains to short noise pulses with a high spike.

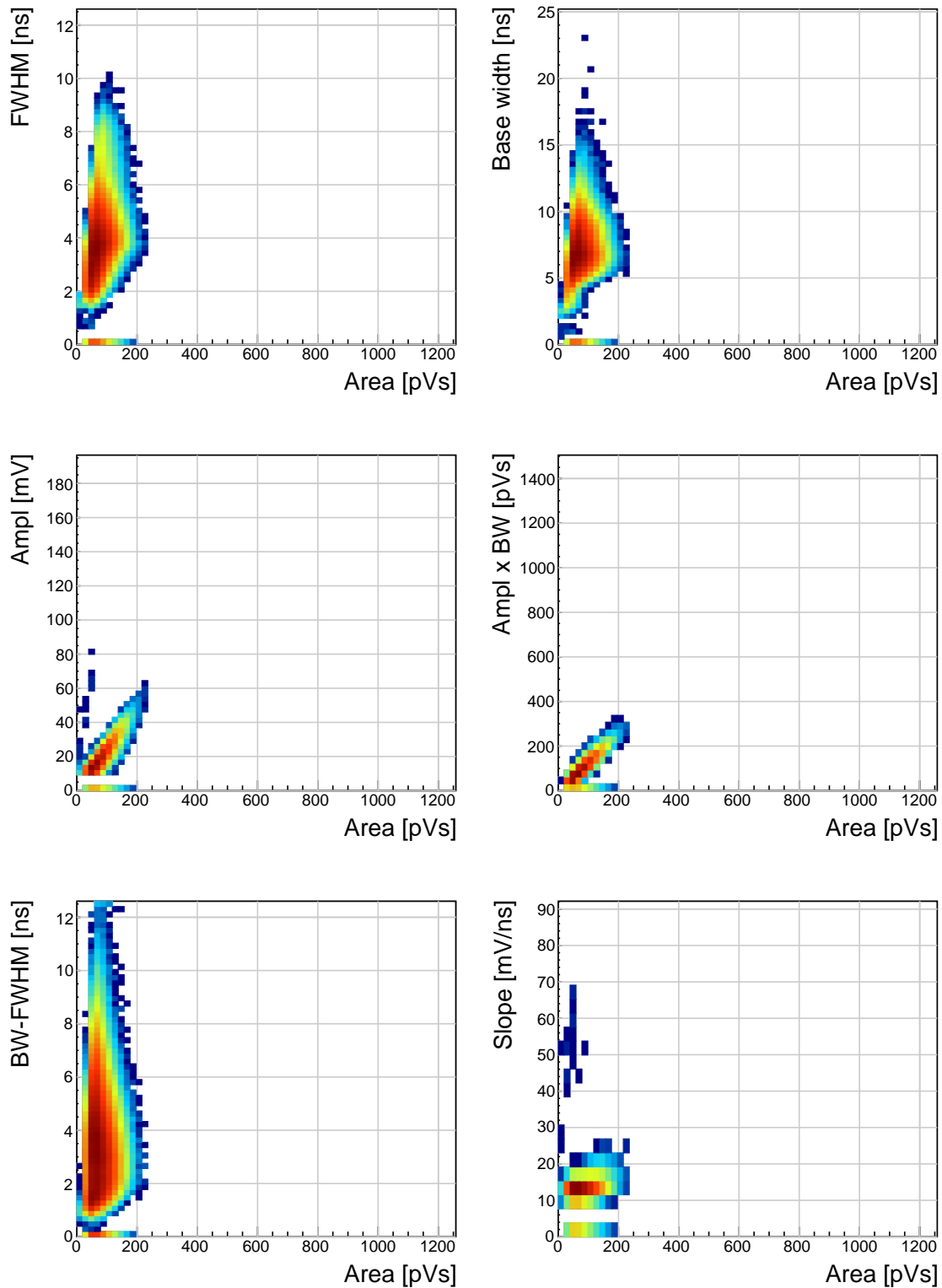


Figure 5.24:  $^{90}\text{Sr}$  scatter plots.

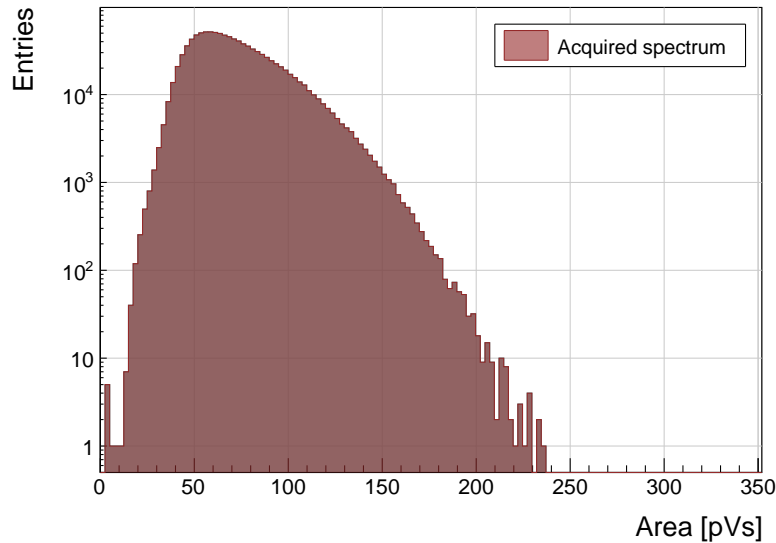


Figure 5.25: Area histogram for  $\beta$  particles. Relative to the 600 pVs  $\alpha$  peak, the expected MPV of a  $\beta$  MIP is  $\sim 30$  pVs, which is not the case in these distributions (peaking at 60 pVs). This is because the PSA device is a self-triggering system, which cuts the lower energetic particles with the trigger threshold. The resulting distribution is therefore only the top part of the real Landau distribution. This is a limitation of the device, governed by the analog noise of the current pre-amplifier.

#### 5.8.3.3 $^{90}\text{Sr}$ source

Figure 5.24 shows the parameter space of the acquired data for  $\beta$  particles - Class 3. Figure 5.25 shows a one-dimensional area distribution of the acquired data.

**Width:** The width of the  $\beta$  cluster is spread over a wide range and is not linearly dependent on the area. This implies that the pulse shapes are not necessarily triangular but have varying shapes.

**Base width:** Wider than the FWHM with a similar distribution.

**Amplitude:** Linear increase with the area. A line of entries with a high slope at low area pertains to short noise pulses with a high spike.

**Calculated area:** Linear increase with area.

**Base width – width:** A wide spread of entries.

**Slope:** A gentle linear increase with the area. A line of entries with a high slope at low area pertains to short noise pulses with a high spike.

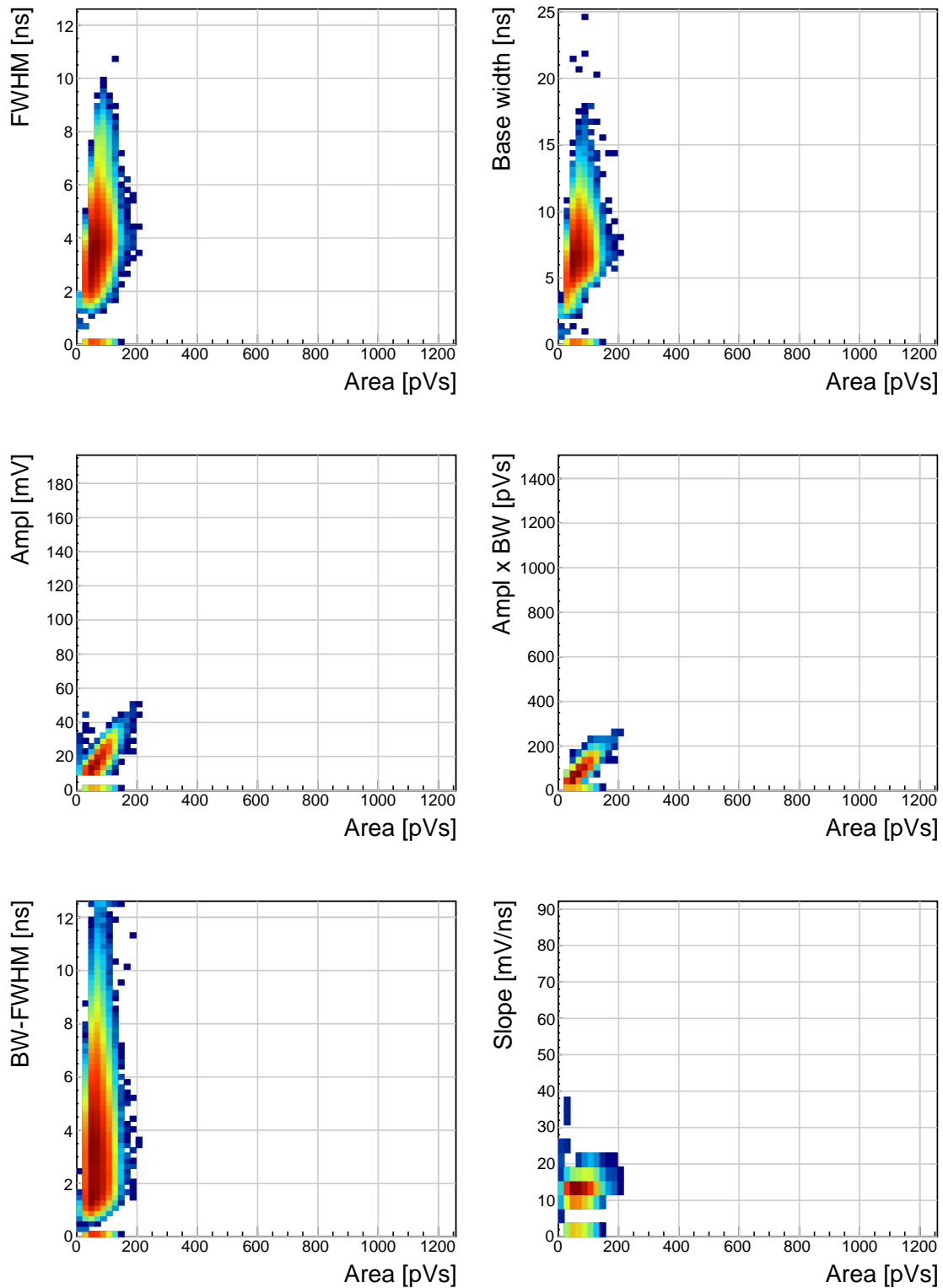


Figure 5.26:  $^{60}\text{Co}$  scatter plots.

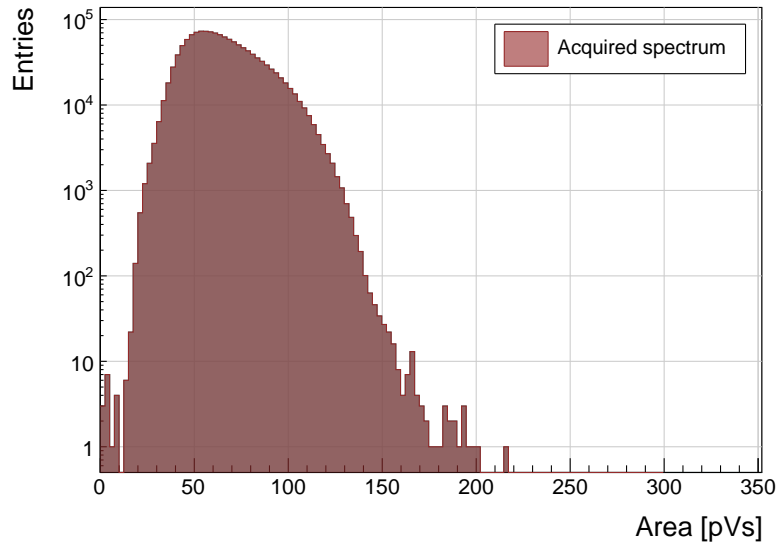


Figure 5.27: Area distribution of  $\gamma$  particles. Relative to the 600 pVs  $\alpha$  peak, the expected MPV of a  $\beta$  MIP is  $\sim 30$  pVs, which is not the case in these distributions (peaking at 60 pVs).

#### 5.8.3.4 $^{60}\text{Co}$ source

The parameter space of the  $^{60}\text{Co}$  source overlaps entirely with that of the  $^{90}\text{Sr}$  source. This renders it virtually impossible to distinguish between  $\gamma$  and  $\beta$  particles. Comparing the width of the  $\gamma$  and  $\beta$  and the high reach of the former, the electron collection of the alphas would need to be used to effectively discriminate between the two types of particles.

The one-dimensional histogram in figure 5.27 shows a quasi-Landau distribution with the MPV at  $\sim 60$  pVs, which is in agreement with the background  $\gamma$  radiation emitted by the  $^{241}\text{Am}$  source, as shown in figure 5.23 in the previous subsection. This is again not a pure Landau distribution – the real MPV should be peaking at 30 pVs, with a minimum expected area of 20 pVs at 2/3 of the MPV. This is not possible to measure due to the high electronics noise of the amplifier and consequently a high trigger threshold to avoid noise triggers.

## 5.9 Applications in neutron instrumentation

The real-time pulse shape analysis procedure can be applied to more complex systems. This section includes three applications where the PSA has been applied.

Semiconductor-based neutron detectors provide a compact technology for neutron detection. However, the cross section of a neutron with diamond is very low, since it only interacts with the core of the atoms. Diamond is mainly used to detect charged particles.

Research neutron reactors radiate a mix of particles, apart from neutrons also  $\gamma$ , considered a background radiation, which conceals the neutron spectrum. When measured with diamond, the signal from neutrons is difficult to distinguish from the photon spectrum. In addition, low energy neutrons do not cause nuclear reactions in the bulk. All in all, the neutron measurements in a reactor using a diamond sensor present a challenge. However, by means of the PSA, the neutron signal can be discriminated from the photon background to some extent. The following examples show how measurements of fast ( $n^+$ ) and thermal ( $n^-$ ) neutrons have been carried out by means of the PSA.

Note the changing scale on the  $x$  axis in the figures.

### 5.9.1 Thermal neutron flux monitoring

Research neutron reactors like TRIGA MARK II [9] at Atominstitut [7] in Vienna are capable of emitting neutrons at a wide range of energies. The neutron flux is proportional to the current power of the reactor. It is therefore instrumental to monitor the neutron flux to make sure that the reactor operation is within the specified limits. However, the byproduct of the radioactive decays in the core is  $\gamma$  radiation, which has an energy range that overlaps with that of neutrons, making it difficult to measure the neutron flux. This is where PSA and diamond detectors come into play. This section describes the application of thermal neutron flux monitoring by means of the PSA.

Thermal neutrons do not interact with the diamond bulk due to their low kinetic energy (of the order of 0.012 eV). Hence a converter foil has to be added to produce second order effects. Incoming neutrons interact with the foil, producing a set of secondary particles. These can then be detected upon hitting the detector bulk. Common neutron interactions that are used in thermal neutron detection are  $^{10}\text{B}(n,\alpha)^7\text{Li}$  reaction and  $^6\text{Li}(n,\alpha)^3\text{H}$  reaction ( $\alpha$  stands for  $^4_2\text{He}$ , see equation 5.2). The focus in this section is on the latter. With a foil installed, there are several possibilities for neutrons to interact with the detector system. Each of these interactions ionises the diamond bulk in its own way, resulting in a specific shape of the current pulse. A neutron can: 1) interact with the foil, producing an  $\alpha$  and a  $^3\text{H}$ , 2) interact with a carbon atom in the lattice, producing an  $\alpha$  and a  $\gamma$  or even three  $\alpha$ . The thermal neutrons do not have enough kinetic energy to interact with the lattice, therefore the focus is on case (1). The equation for this reaction is the following:



The particles in the first case are produced outside the diamond and get stopped immediately upon hitting the sensor. The resulting pulses for both particles have a rectangular shape of the same width, because the carriers drift with the same velocity in both cases. The difference is in the number of free carriers produced - the tritium creates more (proportional to the deposited energy), which in turn induces a higher pulse. The tritium and  $\alpha$  particle produced travel at 180 ° from each other. Therefore a sensor placed after the converter foil can detect at most one of the two.

TRIGA MARK II neutron reactor emits large amounts of  $\gamma$  radiation in the energy range up to 3 MeV. This already affects the measurements of  $\alpha$  particles, the energy of which peaks at 2.05

MeV in the case of  ${}^6\text{Li}$  converter foil. However,  $\gamma$  background radiation can be suppressed by discriminating current pulses of  $\gamma$  from those induced by  $\alpha$  particles.

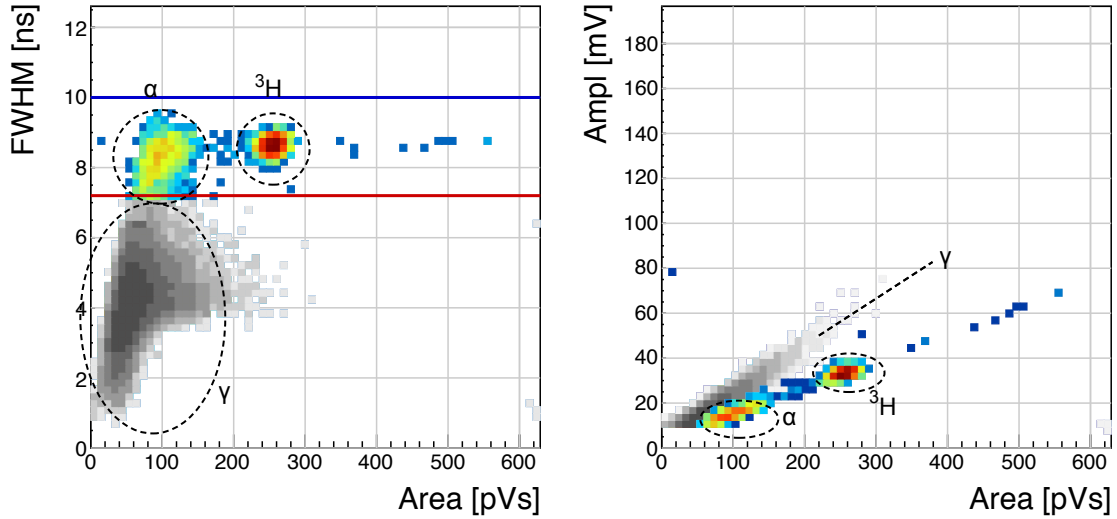
#### **5.9.1.1 Measurements**

ROSY readout device with the implemented Pulse Shape Analysis was put to a test at Atominstitut in Vienna. Their TRIGA neutron reactor is capable of delivering thermal neutrons with the energy 0.012 eV at a rate of  $10^3 \text{ n cm}^{-2} \text{ s}^{-1}$ , with a considerable  $\gamma$  background.

First, the device was calibrated using an unsealed monochromatic  ${}^{241}\text{Am}$  source with the emitted particle energy  $E_\alpha = 5.1 \text{ MeV}$  (taking into account the losses in the air). Then the diamond detector was exposed to the beam. Secondary reaction products ( $\alpha$  and  ${}^3\text{H}$  particles) created by neutrons hitting the converter foil were detected by the diamond sensor, together with a significant photon background. Then the pulse identification algorithm was applied to discriminate between the reaction products and the  $\gamma$ .

The main parts of the detector are an sCVD diamond sensor sized  $4.7 \text{ cm} \times 4.7 \text{ cm}$  and a  $1.8 \mu\text{m}$  thick  ${}^6\text{LiF}$  converter foil, both embedded in an RF-tight PCB. The diamond sensor is biased with a bias voltage of  $1 \text{ V}/\mu\text{m}$  and capacitively coupled to CIVIDEC's C2 40 dB wide bandwidth current preamplifier. A 5 m long BNC cable connects the preamplifier to CIVIDEC ROSY box.

Note: this data set has been taken with an older version of the firmware, which only measured a limited number of pulse parameters.


 Figure 5.28: Thermal neutrons,  $\gamma$ . Qualifier: FWHM.

### 5.9.1.2 Results and discussion

The data shown in figure 5.28 show a high flux of  $\gamma$ , which covers a wide area range.

**Width** The  ${}^3\text{He}$  peak is clearly visible in the top left plot and has almost no overlap with the  $\gamma$  cluster. The  $\alpha$  cluster has a much lower energy and is in the same energy range as the  $\gamma$ . However, its width is higher and makes a separation between the  $\gamma$  and the  $\alpha$ . By setting a qualifier to the right value, the photon background is cut away, leaving only the thermal neutron decay products in the data set.

**Amplitude** A clear difference between the linear coefficients is seen. However, at low area values the  $\alpha$  peak is already hidden by the  $\gamma$ , which makes the amplitude qualifier insufficient.

The resulting one-dimensional area histogram before and after applied cuts is shown in figure 5.29. The blue distribution is the mixed field of background  $\gamma$ , tritium and  $\alpha$  particles. The latter are completely hidden in the  $\gamma$  energy distribution. After applied qualifiers the  $\alpha$  peak appears. There are 2'422 and 1'174 entries in the respective peaks, pointing to a  $\sim 50\%$  detection efficiency of  $\alpha$  particles. This is due to the limitations of the measurement system, which can not detect low-energy  $\alpha$  pulses. These have a low energy due to losses in the air, yielding rectangular pulses with amplitudes below the trigger level. The mean values of the distributions for tritium and  $\alpha$  are at 260 pVs and 100 pVs, which correspond to 2.1 MeV and 0.8 MeV.  $\alpha$  therefore on average lose 60 % of their energy whereas tritium particles only lose 22 %.

Given that the sensor can only detect one of the two particles per neutron interaction due to the geometry of the decay trajectories and assuming that the sensor geometry allows for detection of 100 % of the converted neutrons, the converted thermal neutron detection efficiency of the system is 75 %.

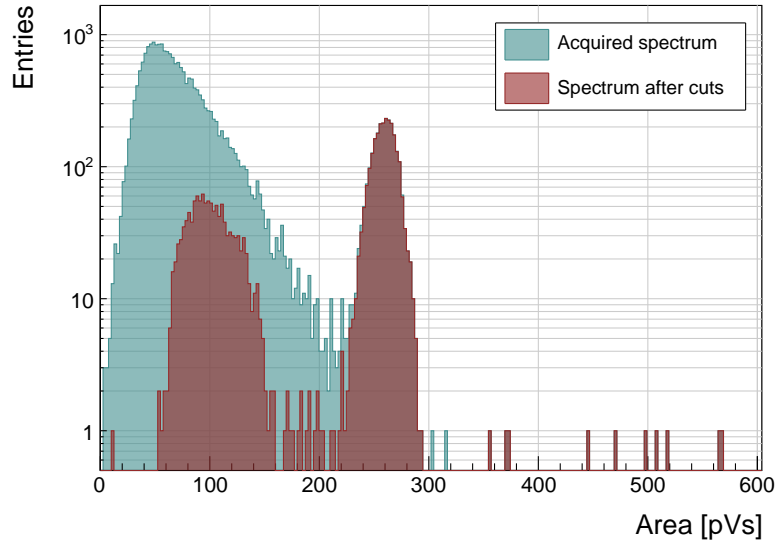


Figure 5.29: Energy spectrum after applied qualifiers reveals the tritium and the  $\alpha$  peak.

To sum up, by applying the FWHM qualifier to the acquired data from the TRIGA neutron reactor, the  $\alpha$  and tritium particles can be identified and separated from the  $\gamma$  background. The resulting cleaned data can be used to correctly count the thermal neutrons detected by the diamond sensor. The 50 % detection efficiency of  $\alpha$  particles can be improved by minimising the distance between the  ${}^6\text{LiF}$  foil and sensor, thus minimising the energy loss in the air.



### 5.9.2 Fusion power monitoring

Many research collaborations around the world are trying to develop a functional fusion reactor, which could provide a cleaner energy source. One of them is ITER [93], a research fusion reactor being built in France. The idea behind it is to harvest energy from the fusion of light atoms into a heavier one. For ITER the fuel chosen is a mixture of deuterium and tritium, which fuse into a helium atom at extremely high temperatures (plasma), emitting a highly energetic neutron as a byproduct. The equation is the following:



The  $\alpha$  particle immediately deposits its energy within the plasma. The neutron, due to its neutral charge, continues its way out of the system where it is stopped. The stopping power is converted into energy, which heats the water into steam, which in turn spins the turbines, generating electricity.

It is possible to monitor the activity of the reactor by measuring the flux of neutrons emitted. Neutron diagnostics such as neutron cameras, neutron spectrometers and neutron flux monitors therefore provide robust measurements of fusion power. A high  $\gamma$  background makes it difficult to accurately measure the neutron flux. This is a motivation to use a diamond based detector with a real-time PSA algorithm.

The neutrons emitted are 14 MeV mono-energetic fast neutrons. The most accurate and efficient way to detect them with a diamond detector is by means of a  $C_{12}(n,\alpha)$  reaction with a carbon atom in the ballistic centre [94]. In this region the positive and negative charge carriers created by  $\alpha$  that start drifting in the opposite directions need the same time to reach the opposite electrodes.

#### 5.9.2.1 Measurements

The  ${}^{239}\text{Pu Be}$  neutron source has been used to simulate the fusion reactor. It emits a mixed field of neutrons and  $\gamma$  with a wide range of energies. The neutrons are rarely detected with diamond – the interactions happen mostly in the electrodes on either side of the detector. The  $\alpha$  particles created by the interactions are detected by the diamond. Depending on the side of the interaction, the created pulse is either due to hole or electron collection. These two interactions make the two distinct lines in the *width* plot at 9 ns and 6 ns, as shown in figure 5.32, top left plot.

A very interesting interaction point is the ballistic centre [94, 92] of the diamond. A ballistic centre is the position from which it takes the holes and the electrons the same amount of time to drift to the respective electrodes. In this case the shortest possible pulse is created. Conversely, to conserve the collected charge and thus the pulse area, the pulse amplitude must be the highest at the ballistic centre. The entries in between are created by neutron interactions at random positions in the diamond, which produce pulses of various shapes.

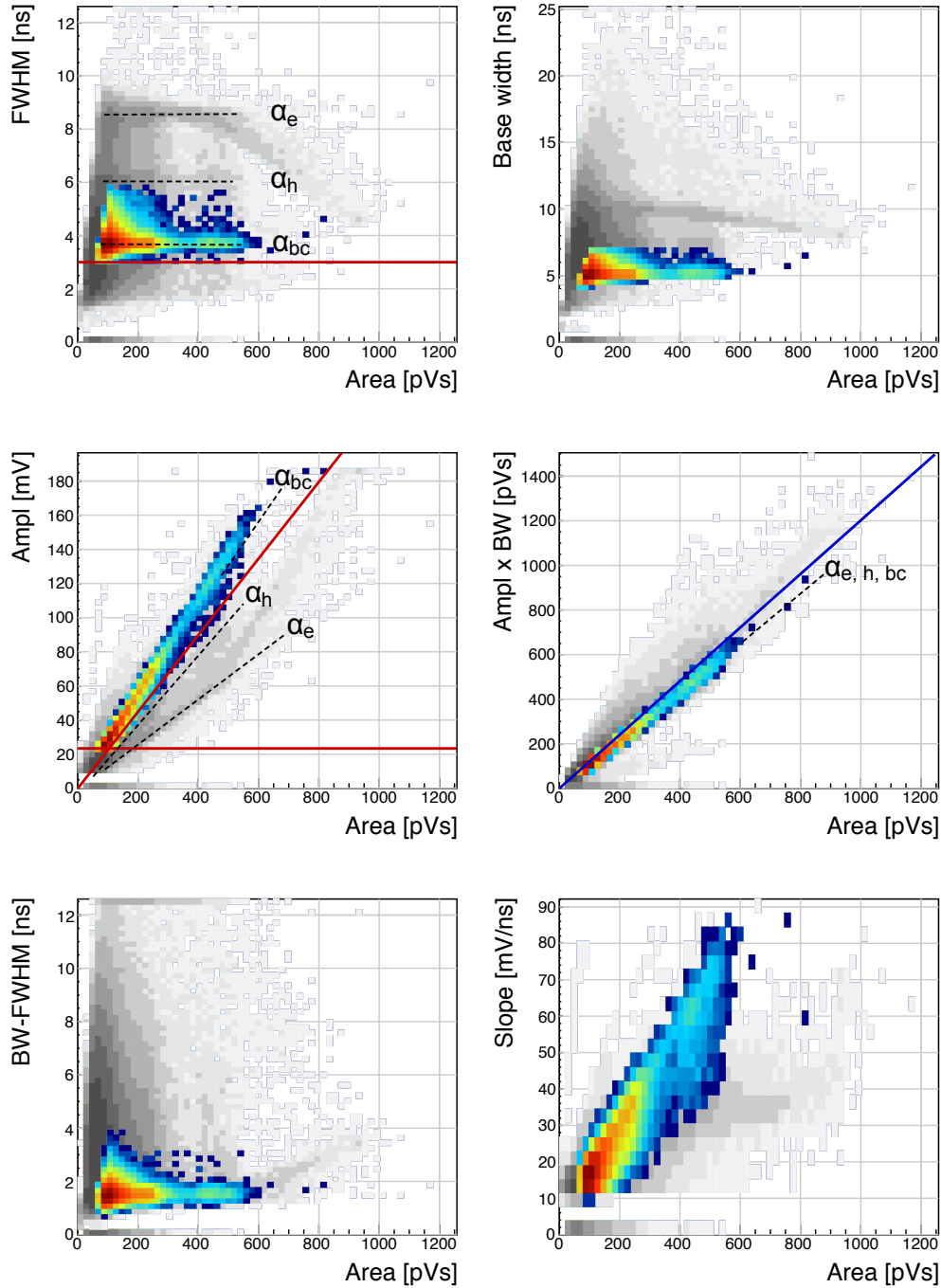


Figure 5.30:  $^{239}\text{Pu}$  Be. Qualifiers: BW-FWHM, FWHM, amplitude, calculated area.

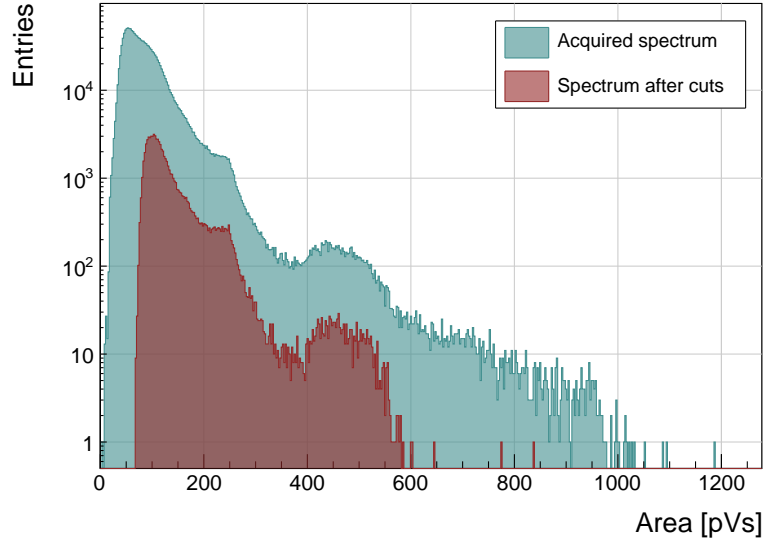


Figure 5.31:  $^{239}\text{Pu Be}$ , energy distribution of the neutrons interacting in the ballistic centre.

### 5.9.2.2 Results and discussion

Coming back to the motivation, the most efficient way of counting the 14 MeV neutrons is through the measurement of the neutrons interacting in the ballistic centre [94, 92]. To extract this type of interaction several qualifiers must be used. The first possibility is the FWHM set to 3–5 ns. However, this time the cuts on the *width* and the *calculated area* are preferred. First, a minimum constant amplitude qualifier is set to 22 mV, as shown in figure 5.32, middle left plot. Then a linear amplitude qualifier is set such that only the pulses with the highest amplitude for every area value are taken. This ensures that the high pulses from the ballistic centre are chosen. Second, a maximum linear calculated area qualifier is set such that only the pulses bearing the closest resemblance to a rectangle are chosen, as shown in figure 5.32, middle right plot. In this space the entries at the bottom of the distribution are bearing more resemblance to a rectangle whereas those at the top are more akin to triangles.

The resulting *width* plot after applied qualifiers highlights the entries with a FWHM of 4 ns, which is the width of the pulses induced by neutrons interacting in the ballistic centre. This proves that these combined qualifiers indeed pinpoint these neutron interactions. The final one-dimensional area/energy distribution of the neutrons interacting in the ballistic centre is shown in figure 5.33.

The result could be further improved by further constraining the identification, e.g. to define the minimum FWHM constant qualifier and the minimum slope constant qualifier. To sum up, by applying the appropriate qualifiers to the data, the neutron interactions in the ballistic centre can be identified.

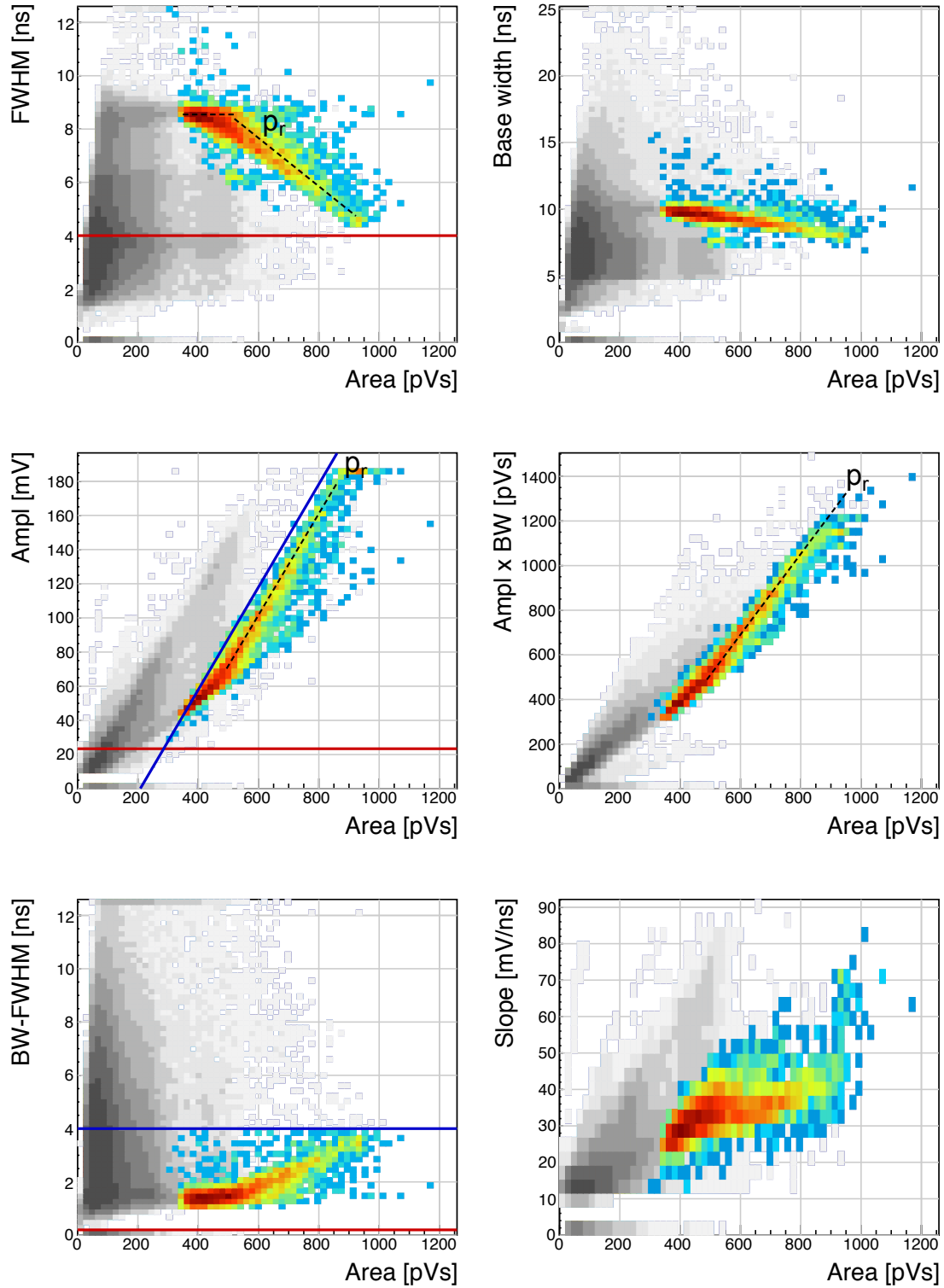


Figure 5.32:  $^{239}\text{Pu}$  Be. Qualifiers: BW-FWHM, FWHM, amplitude, linear amplitude.

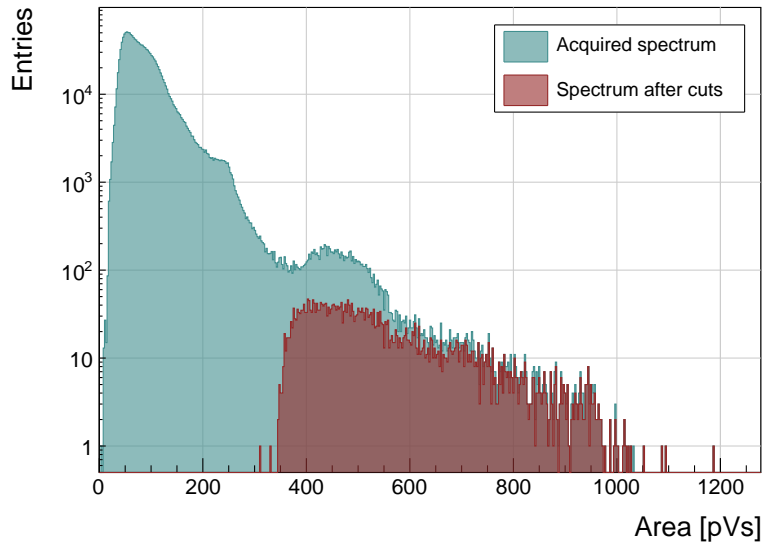


Figure 5.33:  $^{239}\text{Pu Be}$ , energy distribution of the neutrons creating a recoil proton.

### 5.9.3 Recoil proton monitoring

High energy neutrons are typically detected indirectly through elastic scattering reactions. They collide with the nucleus of atoms in the detector, transferring energy to that nucleus and creating an ion, which is detected. If the hydrogen ion – a proton – is created, it travels through the sensor while ionising it and, depending on its initial energy, stops in the sensor or exits it with some residual energy. Its specific parametric signature is discussed in section 5.8.1.3.

#### 5.9.3.1 Measurements

As in section 5.9.2, a  $^{239}\text{Pu Be}$  has been used as a source of high energy neutrons.

#### 5.9.3.2 Results and discussion

The most important qualifier for extracting the recoil protons is the amplitude. However, in this case the constant qualifiers do not help, nor does the linear qualifier starting at 0. To cut the recoil proton strand the starting point of the linear amplitude qualifier line has to start at a higher area value, 200 pVs in this case (shown in the *amplitude* plot in figure 5.32). Other qualifiers are set only to clean the outliers.

The measured parametric signature is not fully in agreement with that in figure 5.18. However, the steady fall in the *width* plot is clearly seen. The resulting one-dimensional plot after applied qualifiers is shown in figure 5.33.

To sum up, recoil protons can be extracted from a mix of created particles after neutron interactions with the diamond sensor.



### **5.9.4 Fast and thermal neutron monitoring**

The CROCUS reactor at EPFL [95] is a research neutron reactor. The research group working on the reactor is interested in measuring neutrons with energies between 1–2 MeV, which is overlapping with the  $\gamma$  background energy range.

The highest output power of the CROCUS reactor is 100 W. Currently there are fission chambers that carry out the neutron counting, which is a measure of the activity of the reactor. The new goal is to measure both neutrons and  $\gamma$ , but separately. The pulse shape analysis is a good solution for this task. For this, a 400  $\mu\text{m}$  thick diamond detector with a specially designed casing was installed to measure the activity. The  ${}^6\text{LiF}$  foil was added for conversion of thermal neutrons. The ROSY box with the integrated PSA routine was used for signal analysis.

#### **5.9.4.1 Measurements**

At the highest reactor activity the real-time system counts and analyses particles at a rate of  $\sim 1.5 \times 10^5 \text{ s}^{-1}$ . The results from a test run at 10 W output power are shown in figure 5.34. The data include a mixed field consisting of fast neutrons,  $\gamma$  and of  $\alpha$  and  ${}^3\text{H}$  particles as products of thermal neutron decay in the  ${}^6\text{LiF}$  foil in front of the detector. The energy deposited in the diamond is not as high as that from the  ${}^{239}\text{Pu}$  Be source. In addition, the analog noise during this measurement is higher than in the previous application. These conditions combined make particle identification at CROCUS a challenging task.

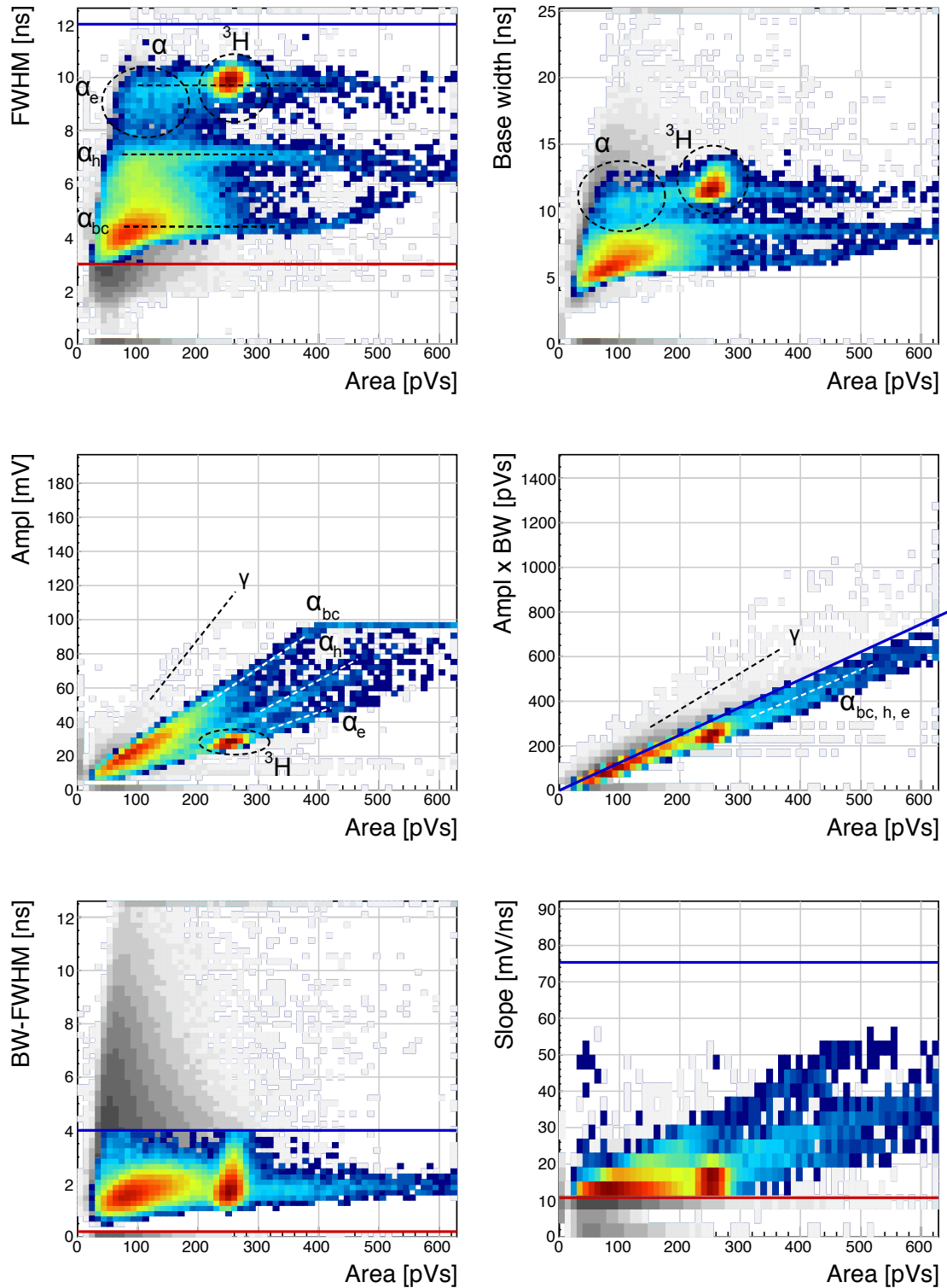


Figure 5.34: Fast neutrons, thermal neutrons,  $\gamma$ . Qualifiers: BW-FWHM, FWHM, calculated area, slope.

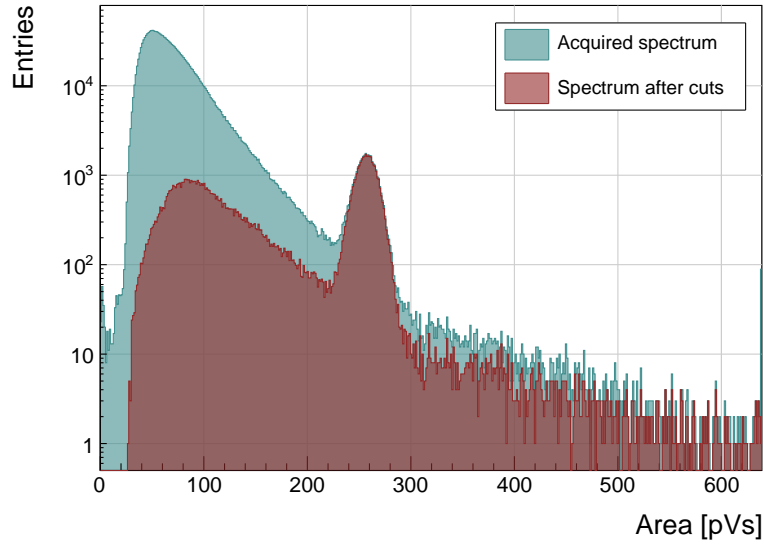


Figure 5.35: Energy spectrum in CROCUS before and after applied qualifiers.

#### 5.9.4.2 Results and discussion

The aim of this exercise is to identify both thermal and fast neutrons. For this the main qualifier used is the Form Factor - the linear line in the *calculated area*. Additional FWHM, FWHM-BW and slope constant qualifiers are used to clean the outlying entries. The resulting accepted entries in figure 5.34 have the distinctive three-line fast neutron signature in the *width* plot with two superimposed islands by the  $\alpha$  and  ${}^3\text{H}$  cluster produced by thermal neutrons in the  ${}^6\text{LiF}$  foil. The  $\gamma$  background is sufficiently suppressed. The resulting one-dimensional histogram of the area/energy distribution is shown in figure 5.35.

To sum up, by applying the Form Factor qualifier both fast and thermal neutrons can be identified, suppressing the  $\gamma$  background.

## 5.10 Conclusion

This chapter describes a system that can identify the type of radiation in real time. The system is implemented on an FPGA in a CIVIDEC ROSY box and is used with diamond detectors. The signal from the diamond sensor is read in and analysed in the firmware. First the shape of the pulse is parametrised. Then the logic determines the type of particle according to the user defined cuts. Finally the parameters are written into a histogram, which is read out by the user. The firmware is designed to carry out the pulse shape analysis of a single pulse in  $\sim 200$  ns, yielding a maximum pulse rate of  $6 \times 10^6$  particles per second. The rate as well as the linearity the measurement stability with respect to noise have been verified using a pulse generator. Then several radioactive sources were used to calibrate the device. Finally the system has been set up in two neutron reactors to test the operation in a mixed field containing thermal neutrons, fast neutrons and  $\gamma$ . The identification can be optimised using a combination of qualifiers to achieve the desired effect.

# Bibliography

- [1] S. F. Novaes. *Standard model: An Introduction*. In *Particles and fields. Proceedings, 10th Jorge Andre Swieca Summer School, Sao Paulo, Brazil, February 6-12, 1999*, 1999.
- [2] Daniel Dominguez. *Standard Model. Le modele standard*. General Photo, Mar 2015.
- [3] E Rossi. *Measurements of the properties of the Higgs-like boson in the four leptons decay channel with the ATLAS detector using  $25\text{fb}^{-1}$  of proton-proton collision data*. *Nuovo Cimento C*, 037(01):217–221. 5 p, 2014.
- [4] European Centre for Nuclear Research, CERN. <http://home.cern>.
- [5] E Regenstreif. *The CERN proton synchrotron, 1. Ned. T. Natuurk.*, 25:117–132, 1959.
- [6] W P C Mills. *The present performance of the SPS*. *IEEE Trans. Nucl. Sci.*, 26(CERN-SPS-AOP-79-9):3176–3178. 3 p, Mar 1979.
- [7] Atominstitut, Technical University of Vienna, Austria. <http://ati.tuwien.ac.at/startpage/EN/>.
- [8] General Atomics. *View of the TRIGA reactor*. 2015.
- [9] *TRIGA MARK II neutron reactor*. <http://ati.tuwien.ac.at/reactor/EN/>.
- [10] *Neutron Time-of-flight experiment*. <https://ntof-exp.web.cern.ch/ntof-exp/>.
- [11] Maximilien Brice. *View of the nTOF detector*. Oct 2010.
- [12] Lyndon Evans. *The Large Hadron Collider*. *Annu. Rev. Nucl. Part. Sci.*, 61:435–466. 32 p, 2011.
- [13] Maximilien Brice. *LHC tunnel*. Jan 2011.
- [14] Arnaud Devred. *Practical Low-Temperature Superconductors for Electromagnets*. CERN, Geneva, 2004.
- [15] W Herr, B J Holzer, and B Muratori. *Design and Principles of Synchrotrons and Circular Colliders: Concept of Luminosity*. *Landolt-Bornstein*, 21C:6.4–1 – 6.4–7, 2013.
- [16] I Bejar Alonso and L Rossi. *HiLumi LHC Technical Design Report: Deliverable: D1.10*. Technical Report CERN-ACC-2015-0140, CERN, Geneva, Nov 2015.
- [17] Peter Jenni. *The experiments: ATLAS*. page 16 p, 2009.
- [18] Joao Pequenao. *Computer generated image of the whole ATLAS detector*. Mar 2008.

## BIBLIOGRAPHY

---

- [19] H Danielsson. Design considerations for a transition radiation tracker in ATLAS. *Frascati Phys. Ser.*, 25:115–120, 2002.
- [20] E. A. Ekimov, V. A. Sidorov, E. D. Bauer, N. N. Mel’nik, N. J. Curro, J. D. Thompson, and S. M. Stishov. *Superconductivity in diamond*. *Nature*, 428(6982):542–545, 04 2004.
- [21] 1951 Park, Jong-Hee, 1955 Sudarshan, T. S., and Inc ebrary. Chemical vapor deposition. Materials Park, Ohio : ASM International, 2001. Includes bibliographical references.
- [22] Satoshi Koizumi, Christoph Nebel, and Milos Nesladek. *Physics and applications of CVD diamond*. Wiley, Hoboken, NJ, 2008.
- [23] CIVIDEC Instrumentation GmbH. *sCVD diamond sensor*. <http://www.cividec.at>, 2015.
- [24] S. Sze and K. N. Kwok. *Physics of Semiconductor Devices*, 3rd ed. Wiley, Hoboken, NJ, 2007.
- [25] Heinz Pernegger. *The Pixel Detector of the ATLAS Experiment for LHC Run-2*. Technical Report ATL-INDET-PROC-2015-001, CERN, Geneva, Feb 2015.
- [26] Claudia Marcelloni De Oliveira. *IBL installation into the inner detector of the ATLAS Experiment side C*. General Photo, May 2014.
- [27] *Bremsstrahlung*. 2016.
- [28] Yoshihiko Hatano, Yosuke Katsumura, and A. Mozumder. *Charged Particle and Photon Interactions with Matter: Recent Advances, Applications, and Interfaces*. CRC Press, 2010.
- [29] W. Blum, W. Riegler, and L. Rolandi. *Particle Detection with Drift Chambers*, volume 2 of 2. Springer-Verlag, Berlin Heidelberg, 2008.
- [30] Helmuth Spieler. *Semiconductor detector systems*. Semiconductor Science and Technology. Oxford Univ. Press, Oxford, 2005.
- [31] W. Shockley. *Currents to Conductors Induced by a Moving Point Charge*. *Journal of applied Physics*, 9:635, 1938.
- [32] S. Ramo. *Currents Induced by Electron Motion*. *Proceedings of the IRE*, 27:584–585, 1939.
- [33] Hendrik Jansen, Norbert Wermes, and Heinz Pernegger. Chemical Vapour Deposition Diamond - Charge Carrier Movement at Low Temperatures and Use in Time-Critical Applications. PhD thesis, Bonn U., Sep 2013. Presented 10 Dec 2013.
- [34] Hendrik Jansen, Daniel Dobos, Thomas Eisel, Heinz Pernegger, Vladimir Eremin, and Norbert Wermes. *Temperature dependence of charge carrier mobility in single-crystal chemical vapour deposition diamond*. *Journal of Applied Physics*, 113(17), 2013.
- [35] Z. Li and H. Kraner. *Modeling and simulation of charge collection properties for neutron irradiated silicon detectors*. *Nuclear Physics B - Proceedings Supplements* 32, (32):398–409, 1993.
- [36] H. Pernegger, S. Roe, P. Weilhammer, V. Eremin, H. Frais-Kolbl, E. Griesmayer, H. Kagan, S. Schnetzer, R. Stone, W. Trischuk, D. Twitchen, and A. Whitehead. *Charge-carrier properties in synthetic single-crystal diamond measured with the transient-current technique*. *Journal of Applied Physics*, 97(7), 2005.

## BIBLIOGRAPHY

---

- [37] Peter Sigmund. Particle Penetration and Radiation Effects Volume 2 - General Aspects and Stopping of Swift Point Charges, volume 151 of *Springer Series in Solid-State Sciences*. Springer-Verlag Berlin Heidelberg, 2006.
- [38] R Kotte, H J Keller, H G Ortlepp, and F Stary. Bragg-peak spectroscopy of low-energy heavy ions. Technical Report ZFK-591, Rossendorf Fachinformations-Zentrum. Zentral-Inst., Dresden, 1986.
- [39] U. Fano. *Ionization Yield of Radiations. II. The Fluctuations of the Number of Ions. Physical Review*, 72:26–29, July 1947.
- [40] R. C. Alig, S. Bloom, and C. W. Struck. *Scattering by ionization and phonon emission in semiconductors*. 22:5565–5582, December 1980.
- [41] Claude A. Klein. *Radiation-Induced Energy Levels in Silicon*. *Journal of Applied Physics*, 30(8):1222–1231, 1959.
- [42] Moritz Guthoff and Willem De Boer. *Radiation Damage to the diamond-based Beam Condition Monitor of the CMS Detector at the LHC*. PhD thesis, CERN, 2014.
- [43] Marco Marinelli, E. Milani, M. E. Morgada, G. Pucella, G. Rodriguez, A. Tucciarone, G. Verona-Rinati, M. Angelone, and M. Pillon. *Thermal detrapping analysis of pumping-related defects in diamond*. *Applied Physics Letters*, 83(18):3707–3709, 2003.
- [44] M. Huhtinen. *Simulation of non-ionising energy loss and defect formation in silicon*. *Nuclear Instruments and Methods in Physics Research A*, 491:194–215, September 2002.
- [45] Moritz Guthoff, Wim de Boer, and Steffen Mller. *Simulation of beam induced lattice defects of diamond detectors using {FLUKA}* . *Nuclear Instruments and Methods in Physics Research Section A: Accelerators, Spectrometers, Detectors and Associated Equipment*, 735:223 – 228, 2014.
- [46] Determination of operational dose equivalent quantities for neutrons. ICRU, Washington, DC, 2001.
- [47] RD42 collaboration. <http://rd42.web.cern.ch/rd42/>.
- [48] M. Mikuž. *Diamond sensors for high energy radiation and particle detection*. TIPP, 2011.
- [49] J. L. Yarnell, J. L. Warren, and R. G. Wenzel. *Lattice Vibrations in Diamond*. *Phys. Rev. Lett.*, 13:13–15, Jul 1964.
- [50] W. Y. Liang. *Excitons*. *Physics Education*, 5:226–228, July 1970.
- [51] H. Frais-Kolbl, E. Griesmayer, H. Kagan, and H. Pernegger. A fast low-noise charged-particle cvd diamond detector. *IEEE Transactions on Nuclear Science*, 51(6):3833–3837, Dec 2004.
- [52] M. Červ, P. Sarin, H. Pernegger, P. Vageeswaran, and E. Griesmayer. *Diamond detector for beam profile monitoring in COMET experiment at J-PARC*. *Journal of Instrumentation*, 10(06):C06016, 2015.
- [53] J. B. Johnson. *Thermal Agitation of Electricity in Conductors*. *Phys. Rev.*, 32:97–109, Jul 1928.

## BIBLIOGRAPHY

---

- [54] H. Nyquist. *Thermal Agitation of Electric Charge in Conductors*. *Phys. Rev.*, 32:110–113, Jul 1928.
- [55] *Xilinx Virtex 5 FPGA*. <http://www.hdl.co.jp/XCM-109/top.560.jpg>.
- [56] M. Garcia-Sciveres. *ATLAS Experiment Pixel Detector Upgrades*. 2011.
- [57] *Element Six*. <http://www.e6.com>.
- [58] *I2a Technologies Pte. Ltd.* <https://www.2atechnologies.com>.
- [59] *DRS4*. <https://www.psi.ch/drs/evaluation-board>.
- [60] The ATLAS IBL collaboration. Prototype atlas ibl modules using the fe-i4a front-end readout chip. *Journal of Instrumentation*, 7(11):P11010, 2012.
- [61] *Paul Scherrer Institute*. <https://www.psi.ch/>.
- [62] Giorgio Brianti. SPS North Experimental Area. Technical Report CERN-SPSC-T-73-8. LabII-EA-Note-73-4, CERN, Geneva, 1973.
- [63] Michal Pomorski. Electronic properties of single crystal cvd diamond and its suitability for particle detection in hadron physics experiments. *Wolfgang von Goethe University, Frankfurt am Main, Germany*, 2008.
- [64] V. Sarin. Comprehensive Hard Materials. Elsevier Science, 2014. p. 411.
- [65] E. Griesmayer and B. Dehning. *Diamonds for Beam Instrumentation*. *Physics Procedia*, 37:1997 – 2004, 2012. Proceedings of the 2nd International Conference on Technology and Instrumentation in Particle Physics (TIPP 2011).
- [66] V Eremin, E Verbitskaya, and Z Li. Effect of radiation induced deep level traps on si detector performance. *Nuclear Instruments and Methods in Physics Research Section A: Accelerators, Spectrometers, Detectors and Associated Equipment*, 476(3):537 – 549, 2002. Proc. of the 3rd Int. Conf. on Radiation Effects on Semiconductor Materials, Detectors and Devices.
- [67] S. F. Kozlov, R. Stuck, M. Hage-Ali, and P. Siffert. Preparation and characteristics of natural diamond nuclear radiation detectors. *IEEE Transactions on Nuclear Science*, 22(1):160–170, Feb 1975.
- [68] Eugenijus Gaubas, Tomas Ceponis, Dovile Meskauskaitė, and Nikolai Kazuchits. Profiling of current transients in capacitor type diamond sensors. *Sensors*, 15(6):13424, 2015.
- [69] Gregor Kramberger, V. Cindro, A. Gorisek, I. Mandic, M. Mikuz, and M. Zavrtanik. *Effects of bias voltage during priming on operation of diamond detectors*. *PoS*, Vertex2012:013, 2013.
- [70] Alison G. Bates and Michael Moll. A comparison between irradiated magnetic czochralski and float zone silicon detectors using the transient current technique. *Nuclear Instruments and Methods in Physics Research Section A: Accelerators, Spectrometers, Detectors and Associated Equipment*, 555(12):113 – 124, 2005.
- [71] Matevž Červ. *The ATLAS Diamond Beam Monitor*. Technical Report ATL-INDET-PROC-2013-021, CERN, Geneva, Nov 2013.

## BIBLIOGRAPHY

---

- [72] A Gorišek, V Cindro, I Dolenc, H Frais-Klbl, E Griesmayer, H Kagan, S Korpar, G Kramberger, I Mandic, M Meyer, M Mikuz, H Pernegger, S Smith, W Trischuk, P Weilhammer, and M Zavrtanik. *ATLAS diamond Beam Condition Monitor*. *Nucl. Instrum. Methods Phys. Res., A*, 572(1):67–69, 2007.
- [73] *Measurement of the Rate of Collisions from Satellite Bunches for the April-May 2010 LHC Luminosity Calibration*. Technical Report ATLAS-CONF-2010-102, CERN, Geneva, Dec 2010.
- [74] Lauren Tompkins. Measurement of the Inelastic Cross-Section and Prospects for Elastic Measurements with ATLAS. Technical Report arXiv:1110.1642, Oct 2011. Comments: From the proceedings of the XIX Workshop on Deep Inelastic Scattering.
- [75] Ken Oyama and the ALICE Collaboration. Cross-section normalization in proton-proton collisions at  $\sqrt{s} = 2.76$  and 7 tev, with alice at the lhc. *Journal of Physics G: Nuclear and Particle Physics*, 38(12):124131, 2011.
- [76] *Proton-proton interaction cross-section*. <http://lhc-machine-outreach.web.cern.ch/lhc-machine-outreach/collisions.htm>.
- [77] H. Kagan and W. Trischuk. Radiation Sensors for High Energy Physics Experiments. John Wiley and Sons, Ltd, 2009.
- [78] *II-IV Incorporated*. <http://www.ii-vi.com/>.
- [79] *CiS Forschungsinstitut fuer Mikrosensorik GmbH*. <http://www.cismst.org/>.
- [80] J Dopke. Overview of the ATLAS Insertable B-Layer (IBL) Project. Jul 2013.
- [81] J et al. Albert. *Prototype ATLAS IBL Modules using the FE-I4A Front-End Readout Chip*. *J. Instrum.*, 7(arXiv:1209.1906):P11010. 45 p, Sep 2012. Comments: 45 pages, 30 figures, submitted to JINST.
- [82] Fabian Huegging. *The ATLAS Pixel Insertable B-Layer (IBL)*. *Nucl. Instrum. Methods Phys. Res., A*, 650(arXiv:1012.2742):45–49. 7 p, Dec 2010. Comments: 7 pages, 5 figures, 4 tables, accepted by Nuclear Instruments and Methods A for publication.
- [83] Richard Claus. *A New ATLAS Muon CSC Readout System with System on Chip Technology on ATCA Platform*. Jun 2015.
- [84] S Mueller, W deBoer, M Schneider, A Sabellek, M Schmanau, C Ruehle, T Schneider, and R Hall-Wilton. *Study of leakage currents in pCVD diamonds as function of the magnetic field*. *Phys. Status Solidi, A*, 206(arXiv:0905.0403):2091–2097. 6 p, May 2009. Comments: 6 pages, 16 figures, poster at Hasselt Diamond Workshop, Mar 2009.
- [85] Garrin McGoldrick, Matevž Červ, and Andrej Gorišek. *Synchronized analysis of testbeam data with the Judith software*. *Nucl. Instrum. Methods Phys. Res., A*, 765:140–145, 2014.
- [86] *EUDET ACONITE telescope*. <https://telescopes.desy.de>.
- [87] E. Griesmayer et al. *Diamond detectors for LHC*. *Proceedings for IBIC2012*. Tsukuba, Japan, 2012.

## BIBLIOGRAPHY

---

- [88] M Capeans, G Darbo, K Einsweiller, M Elsing, T Flick, M Garcia-Sciveres, C Gemme, H Pernegger, O Rohne, and R Vuillermet. ATLAS Insertable B-Layer Technical Design Report. Technical Report CERN-LHCC-2010-013. ATLAS-TDR-19, CERN, Geneva, Sep 2010.
- [89] P. Kavrigin, P. Finocchiaro, E. Griesmayer, E. Jericha, A. Pappalardo, and C. Weiss. *Pulse-shape analysis for gamma background rejection in thermal neutron radiation using CVD diamond detectors*. Nuclear Instruments and Methods in Physics Research A, (795), 2015.
- [90] E. Griesmayer, R. Bergmann, H. Böck, M. Cagnazzo, P. Kavrigin, B. Morgenbesser, and M. Villa. *A Novel Neutron Flux Monitor Based On Diamond Detectors at the Vienna TRIGA Mark II Reactor*. submitted to the proceedings of ICRR 2015, 2015.
- [91] C. Weiss, H. Frais-Kölbl, E. Griesmayer, and P. Kavrigin. *Ionization signals of diamond detectors in fast neutron fields*. 2016.
- [92] C. Weiss. A CVD diamond detector for  $(n,\alpha)$  cross-section measurements. PhD thesis, TU Wien, Vienna, 2014.
- [93] *ITER fusion reactor*. <https://www.iter.org/>.
- [94] P. Kavrigin, E. Griesmayer, F. Belloni, A.J.M. Plompen, P. Schillebeeckx, and C. Weiss.  $^{13}C(n,\alpha_0)^{10}Be$  cross section measurement with sCVD diamond detector. EPJA, 2016.
- [95] *CROCUS neutron reactor*. <http://lrs.epfl.ch/page-55655-en.html>.